

ENHANCING THE STRENGTH AND FORMABILITY OF MAGNESIUM ALLOYS
FOR LIGHTWEIGHT STRUCTURAL APPLICATIONS

A Thesis

by

MATTHEW WEBSTER VAUGHAN

Submitted to the Office of Graduate and Professional Studies of
Texas A&M University
in partial fulfillment of the requirements for the degree of

MASTER OF SCIENCE

Chair of Committee,	Ibrahim Karaman
Committee Co-Chair,	Miladin Radovic
Committee Member,	Ahmed Amine Benzerga
Head of Department,	Ibrahim Karaman

August 2017

Major Subject: Materials Science and Engineering

Copyright 2017 Matthew Webster Vaughan

ABSTRACT

Given their low density and high specific strength, magnesium alloys show excellent potential for use in lightweight structural applications. Current challenges facing these materials are poor strength levels and limited low temperature formability in comparison to the conventionally used steel and aluminum alloys. As such, the focus of this thesis is twofold. First, the effects of different deformation mechanisms on the ductility of a magnesium alloy are systematically investigated, in order to ultimately shed light on potential strategies for enhancing low temperature formability. Second, the need for higher strength magnesium alloys is addressed.

With this in mind, this thesis first investigates deformation and failure mechanisms at low and elevated temperatures, from 25°C to 200°C, under different favored deformation modes (basal slip, prismatic slip, and tension twinning) on the most commonly wrought magnesium alloy, Mg-AZ31. Here, a main finding was that ductility and strength levels can be simultaneously optimized when prismatic slip is the most active deformation mechanism. In addition, dynamic recrystallization (DRX) was found to be most active under basal and prismatic slip at elevated temperatures and positively enhanced ductility. In contrast, tension twinning suppressed DRX and was correlated with comparatively poor ductility.

In the second part of this thesis, a precipitation hardenable alloy, Mg-ZKQX6000, was processed via Equal Channel Angular Processing (ECAP) in the attempt to obtain ultra-high strength levels via grain refinement. Here, ECAP produced ultra-fine grain sizes

with ultra-high strength levels approaching ~400 MPa along several orientations. The roles of precipitation, grain size, and texture were investigated, where it was determined that ductility for ECAP processed samples was limited due to a high volume fraction of precipitates after ECAP. In addition, prismatic slip could be correlated with optimal strength and ductility, confirming findings from the first part of this thesis.

DEDICATION

I would like to dedicate this work to my mother and father, for their unconditional love and support, and also for the many sacrifices they made raising my siblings and me. I will be forever thankful to them as well as my grandparents for always being there for me. I would also like to thank many of my closest friends – including Garrett Jackson, Dangang Ma, Jeremy Tzou, Erick Chow, and Herman Vizcarrondo, among many others – for their constant inspiration and encouragement. In addition, I am thankful to all my awesome siblings and lab mates for their support, and I highly appreciate Dr. Ebubekir Dogan for his friendship and mentorship while I was just an undergraduate student. Of course, I would also like to express my gratitude to Dr. Karaman for his friendship, mentoring me throughout this entire process, and providing me with the many incredible opportunities throughout my undergraduate and graduate studies. Lastly, and most importantly, I am thankful to my Lord and Savior Jesus Christ, who is the source of all the blessings, goodness, and purpose in my life. May He be blessed forever.

ACKNOWLEDGEMENTS

I appreciate Texas A&M University for sponsoring my first year of graduate school with the Masters Merit Fellowship. I would also like to thank my adviser and committee chair Dr. Ibrahim Karaman and my committee members, Dr. Miladin Radovic and Dr. Amine Benzerga, for their guidance and support throughout the course of this research. Furthermore, I would like to thank Robert Barber for assistance with ECAP, and Dr. Jan-Marten Seitz, Rainer Eifler, Dr. Christian Klose, and Professor Hans Maier for their friendship and also for preparing the Mg-ZKQX6000 alloy. A special thanks also to Ceylan Hayrettin for assistance in tension testing and SEM, and to Professor Gwenaelle Proust from the University of Sydney for her invaluable EBSD images. Also, I am highly appreciative to Dr. Ebubekir Dogan, who contributed significantly to this body of work. A heartfelt “thank you” also goes out to the many others who walked with me along this journey of graduate school and offered their time, advice, friendship, and encouragement.

CONTRIBUTORS AND FUNDING SOURCES

Contributors

This work was supervised by a thesis committee consisting of Professor Ibrahim Karaman and Professor Miladin Radovic of the Department of Materials Science and Engineering, and Professor Amine Benzerga of the Department of Aerospace Engineering. The raw EBSD data analyzed in Chapter II was provided by Professor Gwenaelle Proust of the University of Sydney. Select microstructural analyses and tensile tests depicted in Chapter II were conducted by Ceylan Hayrettin and Dr. Ebubekir Dogan from the Department of Materials Science and Engineering and the Department of Mechanical Engineering, respectively. WDS analyses in Chapter III were conducted by Dr. Renald (Ray) Guillemette of the Department of Geology and Geophysics. All other work conducted for the thesis was completed by the student independently.

Funding Sources

Graduate study was supported by a Masters Fellowship from Texas A&M University's Office of Graduate and Professional Studies (OGAPS), by the Air Force Research Laboratory at Eglin Air Force Base, and by the Qatar National Research Fund under National Priorities Research Program award #NPRP-8-856-2-364.

NOMENCLATURE

AS-REC	As-Received
AZ31	Mg-3Al-1Zn-0.2Mn alloy (wt.%)
BSE	Back Scattered Electron
CRSS	Critical Resolved Shear Stress
DRX	Dynamic Recrystallization
EBSD	Electron Back-Scattered Diffraction
ECAP	Equal Channel Angular Processing (also known as Equal Channel Angular Extrusion or ECAE)
ED	Extrusion Direction
ED ₀	Extruded Direction
EDS	Energy Dispersive X-Ray Spectroscopy
EDM	Electrical Discharge Machining
FD	Flow Direction
HCP	Hexagonal Closed Packed
IPF	Inverse Pole Figure
LD	Longitudinal Direction
ND	Normal Direction
N-PLANE	Normal Plane
OM	Optical Microscope
RD	Rolling Direction
RD ₀	Radial Direction

RE	Rare Earth
R-PLANE	Rolling Plane
SE	Scanning Electron
SEM	Scanning Electron Microscope
TD	Transverse Direction
TEM	Transmission Electron Microscope
T-PLANE	Transverse Plane
WDS	Wavelength Dispersive X-Ray Spectrometers
XRD	X-Ray Diffraction
ZKQX6000	Mg-6Zn-0.6Zr-0.4Ag-0.2Ca alloy (wt.%)

TABLE OF CONTENTS

	Page
ABSTRACT	ii
DEDICATION	iv
ACKNOWLEDGEMENTS	v
CONTRIBUTORS AND FUNDING SOURCES.....	vi
NOMENCLATURE.....	vii
TABLE OF CONTENTS	ix
LIST OF FIGURES.....	xi
LIST OF TABLES	xvi
CHAPTER I INTRODUCTION AND LITERATURE REVIEW	1
1.1 Fundamentals of Magnesium Formability	3
1.2 Strategies for Enhancing Strength in Magnesium Alloys	15
1.3 Motivation and Thesis Objectives.....	22
CHAPTER II THE ROLE OF DEFORMATION MECHANISMS AND DYNAMIC RECRYSTALLIZATION ON THE FAILURE OF MG-3AL-1ZN UNDER TENSION AT LOW TEMPERATURES	24
2.1 Materials and Experimental Methods.....	25
2.2 Tensile Flow Responses and Microstructures at Failure.....	28
2.3 Summarizing Deformation Phenomena for Mg at Low Temperatures.....	66
2.4 Conclusions	74
CHAPTER III EFFECTS OF GRAIN SIZE REFINEMENT ON MECHANICAL PROPERTIES OF A PRECIPITATION HARDENABLE MAGNESIUM ALLOY	76
3.1 Materials and Experimental Methods.....	76
3.2 Experimental Results.....	80
3.3 Discussion of Results	85
3.4 Conclusions	93

CHAPTER IV CONCLUSIONS	94
REFERENCES	96

LIST OF FIGURES

	Page
Figure 1. Comparison of magnesium alloys' (a) specific strength and (b) tensile strength and elongation levels with conventionally utilized aluminum and steel alloy systems. Figure adapted from Ref. [13].	2
Figure 2. Several examples of strong textures produced for wrought magnesium alloys. (a) Hot-rolled magnesium plates and sheets exhibit crystal c-axes mostly aligned parallel to the ND. By convention, ND: Normal Direction, RD: Rolling Direction, TD: Transverse Direction. (b) In contrast, for hot-extruded magnesium alloys, the c-axes align mostly along the radial directions, normal to the extrusion direction (ED).	4
Figure 3. Primary slip and twinning systems as the deformation mechanisms in magnesium. Figure adapted from Ref. [23].	5
Figure 4. CRSS of various slip and twinning systems as a function of temperature in a magnesium single crystal. Figure adapted from Ref. [26], which analyzed previous studies for the CRSS values.	6
Figure 5. Twins (dotted box) result in rotation of the matrix (solid box) around the $\langle 1210 \rangle$ axis (normal to the page) by set angles, which are measured between the twin and the matrix c-axes. (a) and (b) correspond to tension and compression twinning, respectively; (c-e) shows double twinning. TEM diffraction patterns for twins when viewed from the $\langle 1210 \rangle$ axis are shown for each twin mode. Figure adapted from Ref. [38].	10
Figure 6. Identification of various twin types via EBSD. Red refers to tensile twins, green to compression twins, and blue to double twins. Figure adapted from Ref. [19].	10
Figure 7. (a) Necklace DRX grains likely form via CDRX. Figure adapted from Ref. [19]. (b) DRX grains at serrated grain boundaries formed via DDRX. Figure adapted from Ref. [39]. (c) DRX lamella nucleate within twins via TDRX. Figure adapted from Ref. [19].	12
Figure 8. Schematic diagram illustrating the formation of a shear zone from the bands of recrystallized grains. Figure adapted from Ref. [41], where the mechanism is explained in depth.	14
Figure 9. A schematic of a working ECAP die. Here, metal is severe plastically deformed by pressing it through a 90° corner, which imposes a shear region of 45° on the processed material. Back pressure can be used to prevent	

shear localization and failure during the processing. By convention, directions for specimens post-ECAP are the following: LD: Longitudinal Direction, ED: Extrusion Direction, FD: Flow Direction.....20

- Figure 10. (a) Schematic of the starting material, a hot-rolled Mg-AZ31 plate. N-Plane: Normal Plane, T-Plane: Transverse Plane, R-Plane: Rolling Plane. TD: Transverse Direction, ND: Normal Direction, RD: Rolling Direction. (b) Metallography of the T-Plane. Dashed ovals capture secondary $\sim\text{Al}_8\text{Mn}_5$ particles. The corresponding pole figure demonstrates that the c-axes generally align along the ND, representing a typical plate basal texture.25
- Figure 11. Engineering stress vs. engineering strain responses of Mg-AZ31 tension specimens tested along three different plate orientations: ND in red (tensile twinning), TD in blue (prismatic slip), and 45toND in black (basal slip). (a) 25°C, (b) 100°C, (c) 150°C, and (d) 200°C.....29
- Figure 12. Metallography near fracture edges of samples tested at 25°C with macro-images of tested samples. (a) and (b) correspond to TD. In (b), voids are evident along twins; $\sim\text{Al}_8\text{Mn}_5$ particles encircled in black. (c) corresponds to 45toND and (d) corresponds to ND. FS: Fracture Surface.....30
- Figure 13. Metallography near fracture edge of ND at 100°C, with a macro-image of the tested specimen. In (a) shear bands are seen to form (annotated in black). In (b), a zoomed in image of (a) according to the red square, twinning activity is obvious. (c) shows no obvious DRX regions; Al_8Mn_5 particles are encircled in white. FS: Fracture Surface.37
- Figure 14. Metallography near the fracture edge of TD at 100°C, with a macro-image of the tested sample. (a-b) show twins localized near the fracture edge. (c) shows DRX grains evident within twins. FS: Fracture Surface.39
- Figure 15. Metallography near the fracture edge of 45toND at 100°C, with a macro-image of the tested sample. (a) shows elongated grains with significant twinning activity near the fracture edge. (b) shows DRX within the twin boundary, where cracks have grown along twins. FS: Fracture Surface.42
- Figure 16. EBSD of 45toND at 100°C. (a) IPF with corresponding texture contour plot. (b) Map of indexed twin types: red = tension twin, green = compression twin, blue = double twin. (c-d) are Schmid factor maps for prismatic slip and basal slip, respectively.....43
- Figure 17. Metallography of TD at 150°C, with a macro-image of the tested sample. (a, c) show voids formed along necklace DRX regions at the fracture surface. (b) shows voids along $\sim\text{Al}_8\text{Mn}_5$ precipitates. DRX are also visible away from the fracture surface (d). FS: Fracture Surface.46

Figure 18. EBSD of TD at 150°C. (a) IPF map with corresponding basal plane textures, (b) indexed twins, (c) Schmid factor map for prismatic slip (for entire image) and basal slip (for dashed inset area near void), with corresponding basal plane texture for the latter.....	48
Figure 19. Metallography of ND at 150°C, with a macro-image of the tested specimen. (a-b) show prominent twinning activity, (b) also shows DRX grains near the fracture edge (red arrows). No cracks were obvious along the ~Al ₈ Mn ₅ secondary particles (encircled in white). FS: Fracture Surface...51	51
Figure 20. Large area EBSD map of ND at 150°C. (a) IPF map, (b) indexed twin boundaries and pole figure corresponding to (a), (c) Large grains and corresponding texture, (d) Refined grains between 0.4-5 μm and corresponding texture. (e-f) show Schmid factor maps and values for basal and prismatic slip, respectively. All pole figures capture the basal plane.52	52
Figure 21. Small area EBSD map of ND at 150°C. (a) IPF map with corresponding texture, (b) Indexed twins, (c) IPF and texture of refined (0.4-5 μm) grains, (d-e) Schmid factor map and values for prismatic and basal slip, respectively.54	54
Figure 22. Metallography of 45toND at 150°C, with a macro-image of the tested sample. (a) shows a crack evident along DRX region, (b) shows a crack present near an ~Al ₈ Mn ₅ precipitate. (c) DRX grains appear to coalesce into shear bands. FS: Fracture Surface.57	57
Figure 23. EBSD of 45toND at 150°C. The IPF map and corresponding basal plane contour texture plots are provided. Notice that the map was constructed near a crack (white arrow). See text for further details.58	58
Figure 24. Comparison between textures of (a) large (>5 μm) and (b) small (<5 μm) grains. Twin boundaries are also visible in (b). EBSD maps corresponds to the same area as in Figure 23.....59	59
Figure 25. Schmid factor maps for (a) prismatic slip and (b) basal slip for 45toND at 150°C. EBSD map corresponds to the same area as in Figure 23.60	60
Figure 26. Metallography of TD at 200°C. (a) and (b) show void and crack initiation, respectively, along DRX regions. White dynamic precipitates are visible in (b) along DRX regions. FS: Fracture Surface.62	62
Figure 27. Metallography of ND at 200°C, with a macro-image of the tested specimen. (a, c) show failure along DRX regions concentrated near the fracture surface. (b) shows DRX are less prominent away from the fracture	

surface. (c) also shows an $\sim\text{Al}_8\text{Mn}_5$ particle (red arrow) near the fracture surface. FS: Fracture Surface.	64
Figure 28. Metallography of 45toND at 200°C, with a macro-image of the tested specimen. (a) shows cracks initiate along the DRX regions, and also near an $\sim\text{Al}_8\text{Mn}_5$ secondary particle (red arrow). (b) shows DRX regions near the fracture surface. FS: Fracture Surface.	65
Figure 29. Engineering stress vs engineering strain tension responses of Mg-AZ31 tested at a temperature range of 25°C to 200°C. (a) ND (tensile twinning), (b) TD (prismatic slip), and (c) 45toND (basal slip). (d) Corresponding evolution of 0.2% yield stress with temperature.	67
Figure 30. Fracture surfaces for all samples tested to failure at 100°C (top) and 200°C (bottom).	71
Figure 31. A comparison of macroscopic images for samples tested to failure for all conditions.	72
Figure 32. Observed failure phenomena summarized for all conditions. Please follow the legend to clarify the schematics. GBs: grain boundaries, TBs: twin boundaries.	73
Figure 33. Schematic of the ZKQX6000 billets with respect to the ECAP press utilized in this study. Prior ECAP, pole figures show the (0002) basal planes are parallel to the Extruded Direction (ED_0). Post ECAP orientations - FD: Flow Direction, ED: Extrusion Direction, LD: Longitudinal Direction.	78
Figure 34. (a) Extruded and (b) pre-ECAP As-Rec microstructures for ZKQX6000. Corresponding prismatic (1010) and basal (0002) pole figures are shown as well. For the As-Rec condition, (c) shows WDS elemental maps for precipitates and the matrix, where precipitates were found to be Zn and Ca rich, with trace amounts of Zr and Ag.	81
Figure 35. Engineering stress vs. strain test curves for ZKQX6000. (a) pre-ECAP condition, called As-Rec. ECAP conditions: (b) A3-1, (c) A3-3, and (d) A3-4. Please refer to Table 2 for ECAP routes for each billet.	82
Figure 36. Metallography via SE for the following ECAP ZKQX6000 conditions: (a) A3-1, (b) A3-3, (c) A3-4. Precipitates cover fine grain regions. Pole figures are also included for (a-c), capturing the orientations of the prismatic (1010) and basal (0002) planes.	83
Figure 37. Precipitate morphologies captured via BSE for a larger area (top images) and a smaller area (bottom images). (a) As-Rec (b) A3-1 (c) A3-3 (d) A3-4.	84

Figure 38. A simplified summary of probable active deformation mechanisms via Schmid factors considerations for all tension and compression tests for As-Rec and ECAP conditions. T-Twin: Tension Twin, C-Twin: Compression Twin.....88

Figure 39. Microstructures at failure for As-Rec under tension along (a) RD₀ and (b) ED₀. Particles indicated by red arrows in (a); crack seen via white ellipse in (b). FS: Fracture Surface.....90

Figure 40. Evidence for dynamic precipitation after ECAP. (a) SE and (b) BSE of A3-3 from the same area; (c) SE and (d) BSE of A3-4 from the same area.....91

LIST OF TABLES

	Page
Table 1. A list of conventional ECAP routes, including the volume percent of fully worked material for billet with a square cross-section and an aspect ratio of 6, subjected to 1-8 passes. Rotations are done about the longitudinal axis. N: number of passes. Table adapted from Ref. [59].....	21
Table 2. ECAP processing details and resultant grain sizes for the ZKQX billets discussed in this study. Rotations were done about ED ₀	79

CHAPTER I

INTRODUCTION AND LITERATURE REVIEW

In recent years, efforts to reduce greenhouse gas emissions and promote energy conservation highlighted the need for lighter structural materials in the automobile industry. Enter magnesium, which is abundantly available, exhibits a low density of 1.74 g/cm^3 (2/3 the density of Al and 1/4 the density of steel), and demonstrates an excellent strength to weight ratio [1-4]. With these properties, magnesium and its alloys are a legitimate material candidate for lightweighting, and, as a result, extensive research has been conducted on these materials over the past three decades with this objective in mind. Today, magnesium components are now successfully being utilized in the automobile, aerospace, and electronics industries as a means for weight reduction. Additionally, magnesium alloys have been implemented in other arenas. As an example, in the medical field, biodegradable implants, including cardiovascular stents, sutures, and screws, are made from magnesium [5]. Another example is found in the defense industry, where magnesium has been researched for novel lightweight military applications [6].

While research efforts have focused on a broad variety of topics regarding magnesium, several overriding themes, or objectives, often motivate these studies. For wrought magnesium alloys, one major objective is to improve their *low temperature formability* – in other words, to create an isotropic ductility behavior for magnesium alloys at ambient temperatures [3, 7-9]. A second aim is to enhance other key mechanical properties, in particular corrosion resistance [5, 10] and strength [11, 12]. Such

improvements in magnesium alloys are necessary in order to make these materials more competitive with the conventional steel and aluminum alloys. Figure 1 captures graphically how magnesium's strength and ductility levels currently (as of 2016) compare with various aluminum and steel alloy systems [13]. With this in mind, the focus of this thesis is to expand the current understanding of magnesium formability and strengthening potential, as elaborated on in Sections 1.1 and 1.2. While a fascinating topic, enhancing the corrosion resistance of magnesium will not be investigated further here.

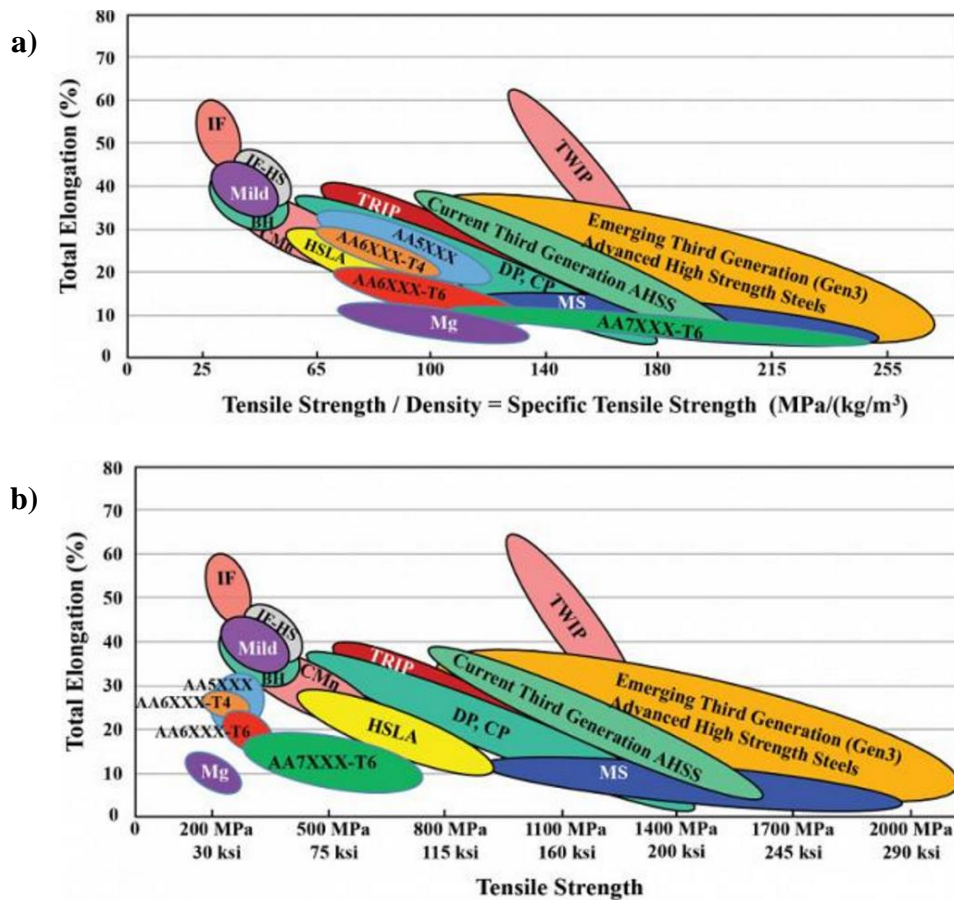


Figure 1. Comparison of magnesium alloys' (a) specific strength and (b) tensile strength and elongation levels with conventionally utilized aluminum and steel alloy systems. Figure adapted from Ref. [13].

1.1 Fundamentals of Magnesium Formability

Two decades ago, industry primarily utilized die-cast magnesium alloy products [3, 14, 15]. However, in more recent years, wrought magnesium products – such as extruded billets or hot-rolled sheets and plates – have grown increasingly popular [15]. The reason for this is wrought processing, a plastic deformation technique, refines grains while removing mechanically detrimental porosity and inhomogeneities from the cast condition. As a result, wrought magnesium alloys exhibit superior mechanical properties in comparison to their cast conditions [15-17]. However, for magnesium, wrought processing creates a strongly textured bulk material, making them highly anisotropic [1, 18]. Several common wrought textures are illustrated in Figure 2 for rolled and extruded magnesium alloys, which consequently exhibit poor low temperature formability [7, 19]. Looking towards the future, development of either novel wrought processing techniques or new magnesium alloys (e.g. novel Mg-Rare-Earth alloys [9, 20]) which favor more random texture development is needed to improve low temperature formability for this light metal.

Wrought magnesium alloys exhibit especially poor formability at temperatures below $\sim 180^{\circ}\text{C}$ [1, 8]. Therefore, forming operations, such as stamping or deep-drawing from hot rolled magnesium sheets, must be conducted at higher temperatures, resulting in increased production costs [14, 16]. Thus, improved low temperature formability is desired by industry to lower costs of production [14]. Furthermore, successful processing at lower forming temperatures would also allow for enhanced mechanical properties for magnesium alloys since refined grain sizes can be maintained at lower temperatures,

whereas grain growth occurs more readily at higher forming temperatures [21]. In short, successful low temperature formability could be used both to enhance magnesium's mechanical properties (via further grain refinement) while simultaneously reducing production costs.

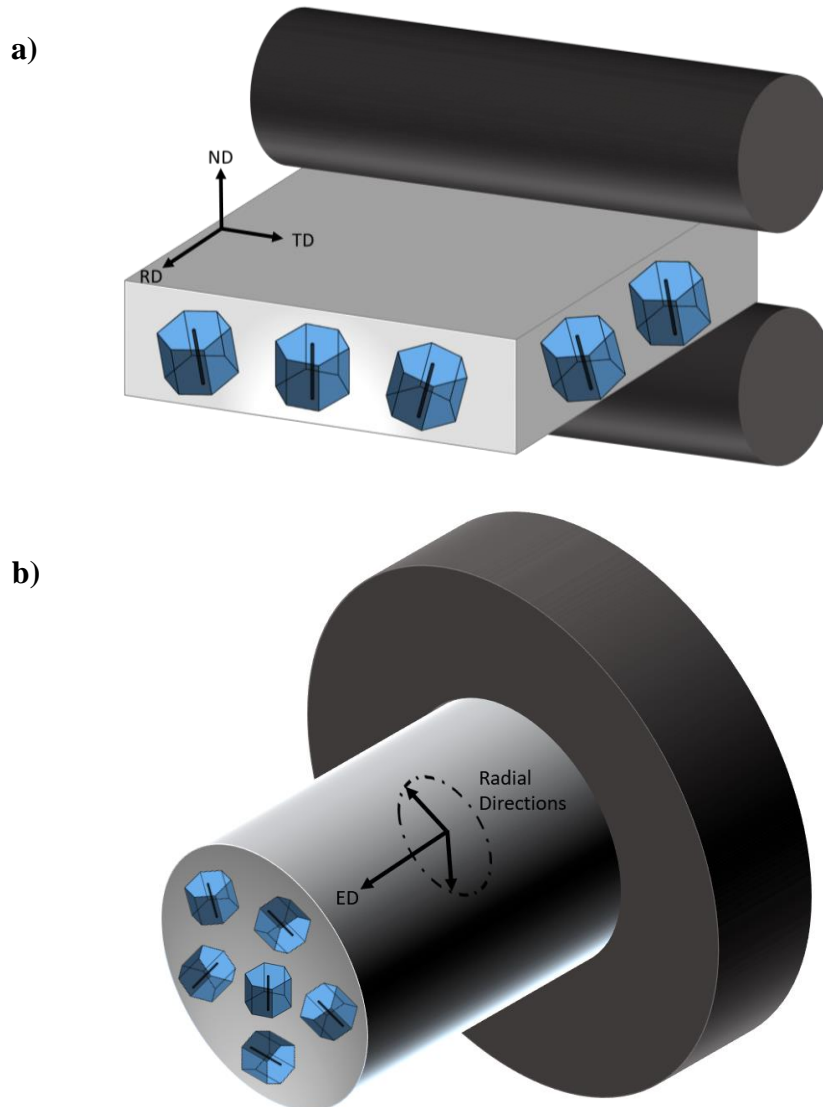


Figure 2. Several examples of strong textures produced for wrought magnesium alloys. (a) Hot-rolled magnesium plates and sheets exhibit crystal c-axes mostly aligned parallel to the ND. By convention, ND: Normal Direction, RD: Rolling Direction, TD: Transverse Direction. (b) In contrast, for hot-extruded magnesium alloys, the c-axes align mostly along the radial directions, normal to the extrusion direction (ED).

To understand the origins of poor low temperature formability in wrought magnesium alloys, it is helpful to start with the fact that magnesium is a hexagonal closed packed (HCP) metal with a nearly ideal c/a axis ratio of 1.624 [1, 7]. Note that for HCP metals, plastic deformation occurs via a variety of slip and twinning systems, which are illustrated for magnesium in Figure 3. Generally, HCP crystals are inherently brittle materials since they possess only one close-packed plane, the basal (0001) plane [22]. Consequently, basal $\langle a \rangle$ slip is the most easily activated slip mode for magnesium, exhibiting the lowest critical resolved shear stress (CRSS) in single crystal studies [16].

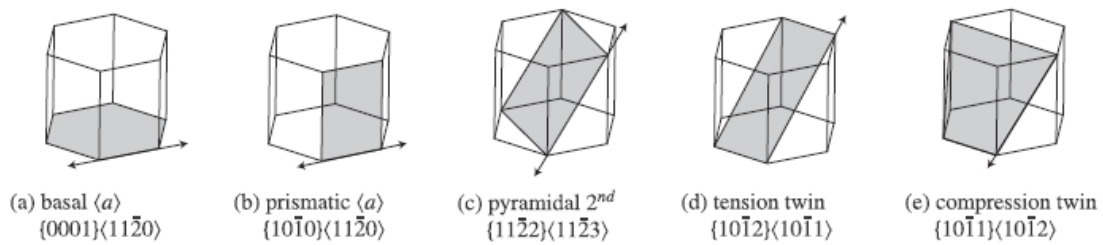


Figure 3. Primary slip and twinning systems as the deformation mechanisms in magnesium. Figure adapted from Ref. [23].

In magnesium, basal slip, which is limited to movements along the $\langle a \rangle$ planar directions, constitutes three total slip systems (there are three $\langle 11\bar{2}0 \rangle$ directions) but just two independent slip systems [8, 16], neither of which can accommodate c -axis deformation. According to Von Mises and Taylor criteria, five independent slip systems are required for homogeneous deformation, and hence good formability [7, 8, 24]. For magnesium, the other slip systems are the prismatic $\langle a \rangle$, pyramidal I $\langle a \rangle$ (not shown in Figure 3), and pyramidal II $\langle c + a \rangle$. As prismatic slip is also limited to movements along the $\langle a \rangle$ directions, it provides for just two independent slip systems. Thus, even

if prismatic slip and basal slip systems are both activated, the von Mises criterion will remain unsatisfied since only four independent slip systems are in operation [8]. Therefore, pyramidal $\langle c + a \rangle$ slip must be active in order to satisfy the Von Mises criterion and, simultaneously, allow for homogenous deformation and good formability via strain along the c-axis [24].

At temperatures above 180°C, magnesium is much more formable due to the activation of basal, prismatic, and pyramidal $\langle c + a \rangle$ slip systems, with the von Mises criterion being sufficiently met [8]. However, while basal slip is athermal with a very low CRSS, the CRSS values for prismatic and pyramidal $\langle c + a \rangle$ slip are highly temperature dependent [25]. The relationship between temperature and CRSS of different deformation mechanisms is illustrated in Figure 4 for the magnesium single crystals, and similar trends follow for wrought magnesium alloys [26]. Notice here that at low temperatures, pyramidal II $\langle c + a \rangle$ slip has a CRSS much higher than basal and prismatic slip and is the most difficult mode to activate.

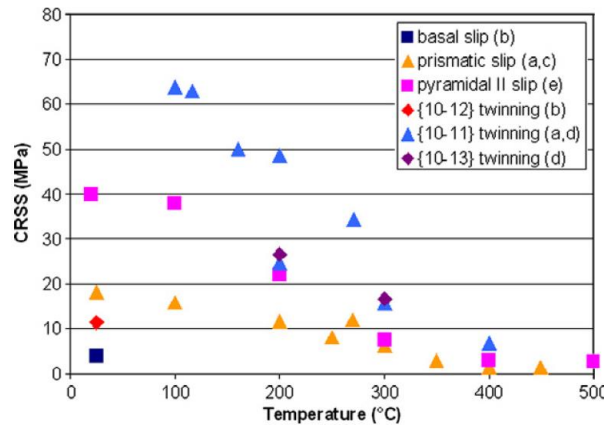


Figure 4. CRSS of various slip and twinning systems as a function of temperature in a magnesium single crystal. Figure adapted from Ref. [26], which analyzed previous studies for the CRSS values.

At room temperature, both prismatic and pyramidal slip are much harder to activate than basal slip [16, 18]. Nevertheless, it is worth mentioning that both non-basal slip systems have been observed for magnesium – even at room temperature [7, 14, 16, 27]. In one study, Koike *et al.* [16] observed cross slip from basal to non-basal slip systems via slip trace analysis, i.e. where dislocations along certain planes of slip are observed directly via the transmission electron microscope (TEM). Therefore, it is possible to activate prismatic and pyramidal slip systems at low temperatures, although it is very difficult to achieve them homogeneously throughout the material. Instead, these slip systems are more active near regions of stress concentrations, which exhibit higher stress levels closer to the CRSS levels required for non-basal slip [28].

Given the lack of readily active slip systems for homogenous deformation at low temperatures, $(10\bar{1}2)$ tensile twinning, which has an athermal [18], low CRSS [28] in comparison to non-basal slip, is typically observed during deformation at low temperatures [24, 29]. Here, tensile twinning, unlike basal and prismatic slip, can accommodate c-axis strain and is easily active as magnesium's c/a ratio is below $\sqrt{3}$ [30]. However, unlike the slip systems in magnesium, tensile twinning is a polar (unidirectional) deformation mechanism that can accommodate only up to 6.5% strain [8], and it is characterized by rapid texture change, stress concentrations at the twin interface, crack formation, and finally macroscopic failure [24, 25, 29]. As such, for improved formability suppression of twinning activity is preferred [19, 31]. Interestingly, twinning is a reversible process, as unloading can result in untwining, which is also known as detwinning [17, 32].

It is also relevant to mention that twinning may seem strain rate sensitive, as less twinning has been observed at slower strain rates [25]. However, there is some dispute about this, as others have argued that twinning is both athermal and strain rate insensitive [25]. The true effect may be derived from the thermal and strain rate sensitivity of non-basal slip mechanisms (i.e. pyramidal $\langle c + a \rangle$ slip), which in-turn affect how active the twinning mechanisms can be. Indeed, twinning occurs more easily at lower temperatures or higher strain rates, while the opposite is true for pyramidal $\langle c + a \rangle$ slip [25, 33]. Furthermore, basal slip and twinning modes have been characterized as non-strain rate sensitive, while the non-basal slip systems have been deemed strain rate sensitive [34]. Therefore, it can be deduced that the strain-rate and temperature sensitivity of non-basal slip mechanisms, in particular pyramidal $\langle c + a \rangle$ slip which can accommodate c-axis strain, influences the relative activity of twinning modes during deformation of magnesium and its alloys.

While tensile twinning is the primary twin mode in magnesium, compression twinning is another active deformation mechanism, although it is more difficult to activate at room temperature than tension twinning due to a much higher CRSS [28]. Characterized by c-axis contraction, compression twinning is generally more rarely observed than tensile twinning [30] and is also associated with void formation and failure [28, 35]. Here, double twinning, where tension twins form inside compression twin boundaries, occurs in

magnesium alloys [24, 35-37]. As the interiors of double twins favor basal slip, this leads to shear localization, void formation, and eventually material failure [35].

As illustrated in Figure 5, twinning rapidly rotates the twinning plane around the $\langle 1\bar{2}10 \rangle$ axis about a set reorientation angle [38]. According to Figure 5, twin reorientation angles can be measured between the twin c-axis and the matrix c-axis from the perspective of the $\langle 1\bar{2}10 \rangle$ axis [38]. Different reorientation angles serve to classify distinct twin types as follows: 86.3° for tensile twinning, 56° for compression twinning, and 38° for double twinning [22, 27, 35, 38, 39]. These different twin types can be identified accurately via TEM by the diffraction patterns shown in Figure 5 [38]; alternatively, they can also be identified via Electron Back Scattered Diffraction (EBSD) as shown in Figure 6 [19]. Rotations can also be roughly seen in pole figures from analyzing the basal pole orientations before and after twinning [8].

Tensile twinning, of course, results in c-axis extension, while both compression and double twinning result in c-axis compression. Under compression, which is characteristic of many wrought processes, twinning reorients the c-axes towards the compressive axis, a mechanism responsible for strong basal textures in wrought magnesium [7, 30]. It is worth mentioning that other HCP metals with excellent ductility, such as Re, Zr, and Ti, have an abundance of active tensile and compression twinning modes [24]. However, since tension twinning is the only readily active twinning mode for magnesium, twinning has an adverse effect on low temperature formability for magnesium alloys and must therefore be suppressed.

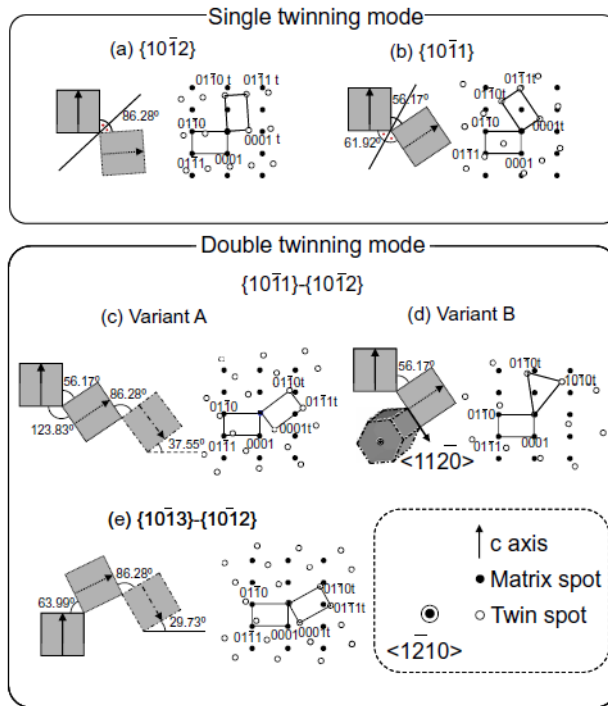


Figure 5. Twins (dotted box) result in rotation of the matrix (solid box) around the $\langle 1\bar{2}10 \rangle$ axis (normal to the page) by set angles, which are measured between the twin and the matrix c-axes. (a) and (b) correspond to tension and compression twinning, respectively; (c-e) shows double twinning. TEM diffraction patterns for twins when viewed from the $\langle 1\bar{2}10 \rangle$ axis are shown for each twin mode. Figure adapted from Ref. [38].

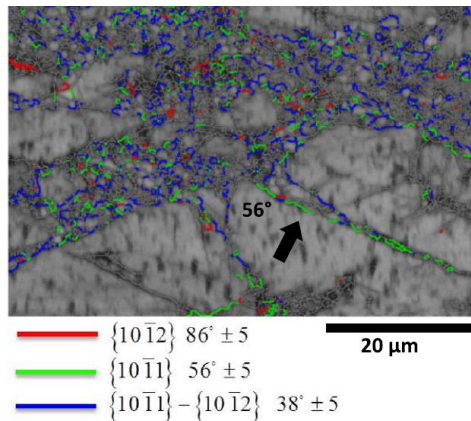


Figure 6. Identification of various twin types via EBSD. Red refers to tensile twins, green to compression twins, and blue to double twins. Figure adapted from Ref. [19].

For magnesium alloys, one successful technique for twinning suppression is grain refinement [36, 40], where a critical grain size can exist below which slip replaces twinning as the dominant deformation mechanism [18]. The reason behind this is twin formation requires the creation of an interface, necessitating energy input, and as the grain size is reduced, a higher number of interfaces must be created for twinning to initiate and grow across each grain [16]. In addition, propagation of twin boundaries across grain boundaries becomes more difficult in fine grained materials due to the larger grain boundary area.

Grain refinement not only allows for twinning suppression, but also promotes ready activation of prismatic and pyramidal slip with limited twinning at low temperatures for better low temperature ductility for magnesium [12, 16]. In general, grain boundaries serve to lower the magnitude of difference in CRSS values between basal and non-basal slip systems, which was observed when CRSS values for magnesium alloys were compared with single crystals [25]. Hence, higher grain boundary area via grain refinement promotes activation of additional slip mechanisms by further narrowing this gap in CRSS values between basal and non-basal slip systems [16]. Therefore, one viable strategy for enhanced formability at lower temperatures is via grain refinement, which by suppressing twinning enhances isotropy in mechanical properties, in turn minimizing anisotropy in strength and ductility [12, 16, 28].

With higher temperatures, dynamic recrystallization (DRX) becomes an increasingly important mechanism affecting grain size [41] and, to a lesser extent, texture evolution [9, 11]. Generally, DRX grains are known to nucleate via either subgrain

rotations, grain boundary bulging, or twins, depending on the deformation temperatures and active deformation mechanisms [3, 42]. These mechanisms have been classified specifically as continuous DRX (CDRX), discontinuous DRX (DDRX), and twin DRX (TDRX), respectively, and were reviewed in detail by Kaibyshev *et al.* [43]. Examples of each DRX mechanism are shown in Figure 7.

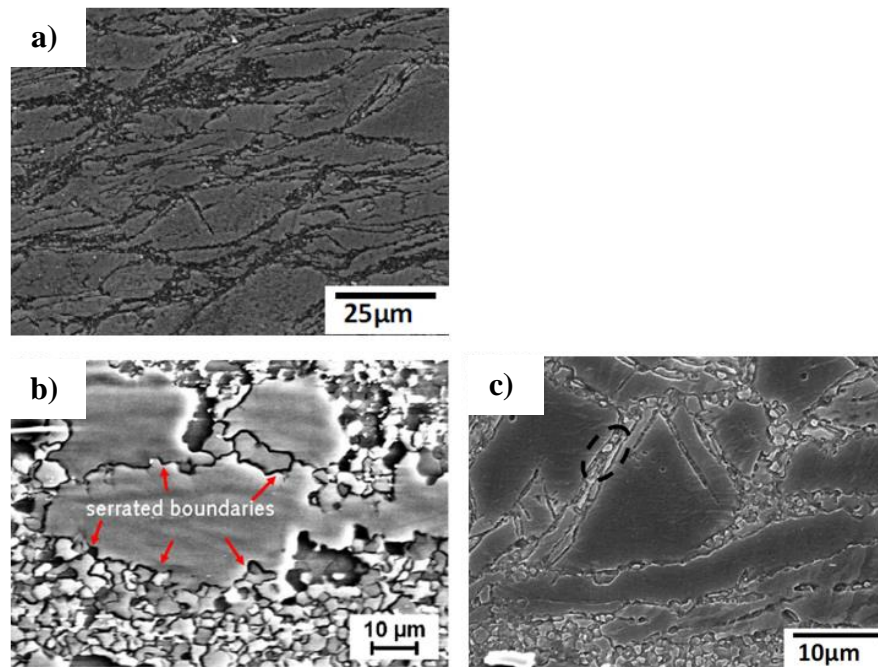


Figure 7. (a) Necklace DRX grains likely form via CDRX. Figure adapted from Ref. [19]. (b) DRX grains at serrated grain boundaries formed via DDRX. Figure adapted from Ref. [39]. (c) DRX lamella nucleate within twins via TDRX. Figure adapted from Ref. [19].

CDRX is thought of generally as a more gradual process (hence the name), where low angle boundaries (LABs) accumulate via strain, eventually transforming to high angle boundaries (HABs) which precede the formation of recrystallized grains [15, 39, 43]. Therefore, evidence for CDRX in the microstructure can be seen in parent grains if subgrain boundary angles increase in magnitude when moving from the parent grain's

core (i.e. center) towards its mantle (i.e. perimeter). In this case, necklace DRX lamella may be observed bordering the parent grain's mantle region. CDRX is strongly correlated with non-basal slip (as in Figure 7a) and has been observed at lower temperatures near grain boundaries, where stress concentrations allow for more easy activation of non-basal slip mechanisms [42]. In contrast, DDRX is marked as a nucleation process via a grain boundary migration mechanism, where dislocations are removed via the formation or propagation of HABs [3, 43]. Nucleation of a new grain usually happens at the grain boundaries [15]. Unlike CDRX, DDRX is not dependent on the accumulation of low angle grain boundaries but can occur directly (i.e. discontinuously) [43]. In this regard, evidence of DDRX can be seen as serrated or bulging parent grain boundaries at the site of a new DRX grain (see Figure 7b) [2, 43, 44].

Finally, TDRX (Figure 7c) has been observed within primary tensile twins and primary compression twins [43]. TDRX within tensile primary twins nucleate via a mechanism similar to CDRX, where formation of LABs within the twin interiors gradually leads to HABs with increased strain, creating a nucleus bounded by LABs and twins [39]. Subsequently, these nuclei transform into recrystallized grains. DRX grains have also been observed within double twin boundaries [19, 41]. Given that twinning is more prevalent at lower temperatures, TDRX is more expected at lower deformation temperatures or higher strain rates.

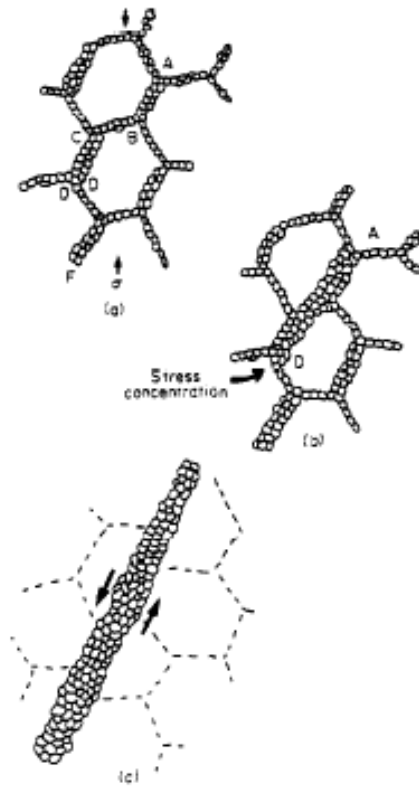


Figure 8. Schematic diagram illustrating the formation of a shear zone from the bands of recrystallized grains. Figure adapted from Ref. [41], where the mechanism is explained in depth.

At low temperatures, DRX regions have been identified as potential failure regions. As shown in Figure 8, shear zones consisting of fine, DRX grains are “softer” regions where cracks can originate more readily [21, 41]. Dogan *et al.* [19] also observed that fracture at 150°C at very high strains (>100%) was associated with DRX in double twin regions, where DRX grains formed and, subsequently, accumulated into shear zones. These shear zones were soft regions where the strain was localized and eventually microcracks nucleated, leading to failure [19].

A discussion of low temperature formability would not be complete without mentioning the different microstructural morphologies related to brittle and ductile fracture. In this regard, several distinct types of fracture surfaces are observed at low temperatures in magnesium alloys indicating either brittle or ductile fracture. Generally speaking, brittle failure in metals is associated with intergranular and cleavage fracture along densely packed atomic planes, while ductile failure is associated with small dimples, cavitation, and plastic instability [45, 46]. When deforming magnesium at room temperature, brittle fracture occurs via intergranular and transgranular separation, which is associated with shear zone formation, grain pullouts, and also failure along twin regions [47]. In magnesium alloys, ductile fracture is characterized by strain localization, followed by microvoid formation, growth, and coalescence [35, 47, 48]. Microvoids are associated with secondary particles and double twinning, which both promote strain incompatibility [31, 35, 49].

1.2 Strategies for Enhancing Strength in Magnesium Alloys

One strategy for enhancing both formability and strength for magnesium is alloy design – a fascinating topic, as selection of different alloying element combinations can have dramatic effects on microstructure and mechanical properties. In addition, many alloy systems have yet to be discovered. One path for improving magnesium's mechanical strength is via novel alloy design [4], which can take advantage of two related techniques for enhanced strength – solid solution strengthening and precipitation hardening. As touched upon in the Section 1.1, another avenue for improving the mechanical strength of

Mg, reducing anisotropy, and enhancing formability is via grain size refinement [12, 50, 51]. As such, these three strategies for strengthening will be discussed in detail in the current section.

Several common examples of solid solution strengthened alloys include the Al and Zn based alloys, such as AZ31, AZ91, and ZK60. As seen on phase diagrams for binary magnesium alloys (not shown here), each element shows unique solubility levels in magnesium which typically increase with temperature. For solid solution strengthening, elements are mixed with the molten magnesium at elevated temperatures, which is followed by air cooling. As solubility is higher at higher temperatures, the alloy can exhibit a super saturated solution once it has cooled to room temperature. Generally, the super saturated alloy can exhibit enhanced strength and ductility in comparison to pure magnesium, provided the alloying levels utilized are appropriate – accumulation and embrittlement along grain boundaries may occur above certain thresholds. Therefore, an optimal level of each alloying element is necessary to design for the best material properties, and this process requires an extensive survey of the existing literature and sometimes a fair amount of trial and error.

Solid solution strengthening allows for moderate strength enhancement, which can be further improved upon via precipitation hardening and grain refinement. Here, a supersaturated alloy is wrought processed after casting for grain refinement, removal of porosities, and microstructural homogenization. Afterwards, the alloy is aged for further strengthening, where different alloys exhibit unique age hardening responses. At aging temperatures – which are lower than the wrought processing temperatures – the solubility

of alloying elements is comparatively lower. Therefore, aging heat treatments allow for further strengthening via the nucleation of secondary particles from the matrix, which is thermodynamically favored due to their lower solid solubility. Essentially, the slightly elevated aging temperature serves to increase the kinetics of particle nucleation. It is also worth mentioning that aging does occur spontaneously at room temperature for a super-saturated material, yet the rate of particle nucleation is exceedingly slow in comparison to the elevated aging temperatures. Interestingly, aging was coined for this reason, as the microstructure and mechanical properties can evolve (i.e. age) over time.

Essentially, solid solution hardening followed by aging heat treatment can effectively enhance the strength of magnesium alloys. As aging heat treatments promote the nucleation of secondary precipitates which can enhance the strength levels, this method of strengthening is called precipitation hardening. Precipitation hardening has been shown to effectively enhance strength and reduce anisotropy in Mg alloys [52, 53]. Different magnesium alloy systems exhibit different precipitation hardening characteristics. In particular, precipitation hardening has been shown effective for Mg-Rare Earth (RE) alloy systems, which have shown ultra-high strength levels over 400 MPa [4, 54]. Here, a primary mechanism for ultra-high strength is via prismatic plates (i.e. major precipitate planes located on the prismatic planes), which form via aging and serve to narrow the gap in the CRSS between basal slip and prismatic and pyramidal slips [4, 54].

As RE elements are expensive and not readily available, design for RE-free, precipitation hardenable magnesium alloys is warranted. In this regard, recently Mendis

et al. demonstrated that precipitation hardening can be achieved in the Mg-ZK60 alloy by alloying with trace additions of Ag and Ca; these particles serve as precipitate nucleation sites and thus allow for a higher number density of MgZn₂ precipitates to form during the aging process [52, 53]. Here, a peak aged condition with a bimodal grain size averaging ~8.5 μm, with UTS nearing 350 MPa and an elongation approaching 15%, was produced [52]. Generally speaking, during precipitation hardening material strength increases with increasing precipitate number density (and consequently simultaneous refinement) [52, 55]. As an alloy must be super saturated to be precipitation hardenable, the two strengthening schemes – solid solution strengthening and precipitation hardening – are intrinsically linked.

To provide further strengthening to precipitation hardenable magnesium alloys, one can also design for a fine grain size. As mentioned earlier, an added advantage of a refined grain size in magnesium alloy systems is reduction of twinning activity [36, 56], thereby enhancing formability as twinning is often associated with strain hardening and localization, followed by void nucleation and failure [56]. Grain refinement is known to enhance the strength of magnesium alloys according to the Hall-Petch [57, 58] relationship:

$$\sigma_y = \sigma_0 + k_y \times d^{-1/2}, \quad (1)$$

where σ_y is the yield stress, k_y is the Hall-Petch slope, d is the average grain size diameter, and σ_0 is a material dependent strength constant. Here, magnesium alloys show competitive potential as they have a considerably higher Hall-Petch coefficient than Al

alloys [52]. To make the most of the Hall-Petch relationship, an ultrafine grain size (i.e. $d < 1 \mu\text{m}$) is ideal [12].

Grain refinement to ultra-fine levels ($d < 1 \mu\text{m}$) has been shown to produce ultra-high strength levels in RE free Mg alloys [12, 51]. Razavi *et al.* successfully refined the grain size to $\sim 0.35 \mu\text{m}$ via ECAP of the Mg-3Al-1Zn alloy (AZ31), obtaining a UTS over 400 MPa and a ductility approaching 15% [12]. Remarkably, ductility here was only slightly below the initial condition of $\sim 18\%$, where the grain size was much larger ($\sim 33 \mu\text{m}$) [12]. Evidently, grain refinement in Mg can be advantageous for both strength and ductility.

As was touched upon in the previous section, limited low temperature formability for magnesium alloys requires higher processing temperatures, resulting in grain growth. Thus, obtaining ultra-fine grain sizes via conventional wrought processes, such as forging, rolling, or extrusion, is difficult. Alternatively, a technique called Equal Channel Angular Processing (ECAP) is capable of achieving ultra-fine grain sizes for magnesium [12]. As shown schematically in Figure 9, ECAP severely plastically deforms the processed material by pressing it through a 90° channel, exerting over 100% strain to the material [59]. Back pressure can be utilized to prevent shear localization and failure in one pass by increasing the hydrostatic pressure levels.

Note in Figure 9 that the cross-sectional area is maintained during ECAP, which allows for samples to be processed multiple times. In this regard, the processed sample can be rotated along the longitudinal axis in-between passes to produce novel grain morphologies and textures [59]. Conventional routes are listed in Table 1 with volume

percent of fully worked material, which is a function of the chosen route and the number of imposed passes. As ECAP allows for texture engineering, it is an ideal processing technique for magnesium alloys for generation of near random textures and has proven capable of improving formability in Mg alloys by weakening the strong textures of wrought Mg products [12, 50]. Indeed, improved low temperature formability and a reduction in tension-compression asymmetry has been achieved for magnesium alloys via ECAP [50, 51].

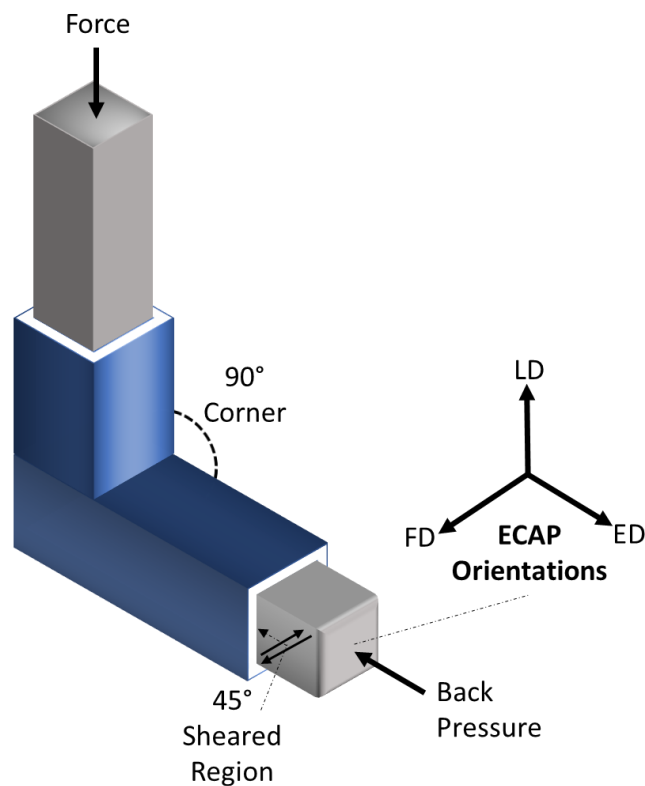


Figure 9. A schematic of a working ECAP die. Here, metal is severe plastically deformed by pressing it through a 90° corner, which imposes a shear region of 45° on the processed material. Back pressure can be used to prevent shear localization and failure during the processing. By convention, directions for specimens post-ECAP are the following: LD: Longitudinal Direction, ED: Extrusion Direction, FD: Flow Direction.

To achieve an ultrafine grain size via ECAP, a multi-temperature step-down method is utilized, where grain size is refined further by gradually lowering the processing temperature in between passes for a given route [12, 50, 51]. Of course, directly ECAP of magnesium at ambient temperature should allow for ultra-fine grain sizes, but cannot be done due to magnesium's poor low temperature formability. As solid solution hardening, precipitation hardening, grain refinement, and texture engineering have been shown in the literature to produce high strength and ductility levels for magnesium alloys, a feasible next step would be to combine these techniques via ECAP for peak strength levels in Mg alloys.

Table 1. A list of conventional ECAP routes, including the volume percent of fully worked material for billet with a square cross-section and an aspect ratio of 6, subjected to 1-8 passes. Rotations are done about the longitudinal axis. N: number of passes. Table adapted from Ref. [59].

Volume percent of fully worked material for ECAE processing of a square cross-section billet with an aspect ratio of six

Route	Rotations before extrusion	Number of passes							
		1	2	3	4	5	6	7	8
A	0°, all passes	83.3	75	66.7	58.3	50	41.7	34.7	29.8
B(B _A)	90°, <i>N</i> even, 270° <i>N</i> odd	83.3	77.8	72.2	66.7	61.6	55.6	50.2	44.4
C	180°, all passes	83.3	83.3	83.3	83.3	83.3	83.3	83.3	83.3
D(B _C)	90°, all passes	83.3	77.8	73.6	72.2	72.2	72.2	72.2	72.2
E	See text	83.3	83.3	77.8	77.8	77.8	77.8	77.8	77.8
F	See text	83.3	77.8	77.8	77.8	77.8	77.8	77.8	77.8

Interestingly, Dogan *et al.* recently showed that a large amount of *dynamic* precipitation occurs during ECAP of AZ31 at low temperatures (150°C) [60]. This is remarkable since Mg alloys such as AZ31 are generally not considered to be precipitation hardenable, as they demonstrate a limited age hardening response [52]. The effect of dynamic precipitates on mechanical properties of ZK alloys remains scarce in the literature; generally efforts focus on traditional *static* precipitates (i.e. precipitates

nucleated via aging after wrought processing). Therefore, the interaction between grain refinement and precipitation via ECAP requires further attention.

1.3 Motivation and Thesis Objectives

A fundamental understanding of low temperature deformation mechanisms in magnesium alloys and their relation to failure is warranted in order to design for improved processing techniques that can enhance formability within these temperature regions. Therefore, a study of the activities of various deformation mechanisms as a function of low and elevated temperatures and crystallographic texture was conducted for Mg-AZ31 (Mg-3Al-1Zn-0.2Mn alloy (wt.%)), which will be discussed in detail in Chapter II. This study correlates the effects of different deformation mechanisms on the microstructural evolution and failure characteristics at low temperatures, seeking to elaborate upon effects of various deformation modes on strength, ductility, and failure.

In addition, in Chapter III, the challenge of low strength for magnesium alloys will be addressed, where an attempt to combine the effects of solid solution hardening, precipitation hardening, and grain refinement for enhanced strength is conducted. Here, the effect of grain size refinement and precipitation during ECAP is investigated on a precipitation hardenable Mg-ZKQX6000 (Mg-6Zn-0.6Zr-0.4Ag-0.2Ca alloy (wt.%)) alloy, where low temperature ECAP was implemented via a multi-temperature step-down approach between 125°C – 200°C. Ultrafine grain sizes were produced, with a dynamically precipitated high number density of second phases. The mechanical characteristics of the processed samples are discussed with respect to grain size,

precipitate morphology, and crystallographic texture. Chapter IV concludes this thesis by providing some recommendations for future work with magnesium alloys.

CHAPTER II
THE ROLE OF DEFORMATION MECHANISMS AND DYNAMIC
RECRYSTALLIZATION ON THE FAILURE OF MG-3AL-1ZN UNDER TENSION
AT LOW TEMPERATURES

While a large number of studies focused on high temperature ($>200^{\circ}\text{C}$) deformation and DRX behavior of AZ31 [2, 21, 39, 61], a detailed microstructural investigation at low-temperatures emphasizing interaction between slip and twinning, characteristics of DRX, and failure mechanisms remains scarce in the literature. Moreover, previous studies have largely focused on relationships among strain rate sensitivity and temperature [8, 31, 39, 62, 63], rather than solely the effect of temperature. This approach can cloud effects of specific deformation mechanisms on microstructural development at low temperatures, where hard slip mode activities are both highly temperature and strain rate sensitive [31]. Therefore, in the current chapter the relationship between different deformation mechanisms and microstructural evolution will be investigated for the most common wrought magnesium alloy, AZ31, at low temperatures ($<200^{\circ}\text{C}$). Here, an effort to categorize characteristics of failure within this temperature region is conducted to provide insights useful for achieving better formability at low temperatures.

2.1 Materials and Experimental Methods

In this study, an AZ31 hot-rolled plate with a thickness of 25 mm was acquired commercially and subsequently annealed under an argon atmosphere at 350°C for 12 hours. As shown in Figure 10b, this heat treatment resulted in a homogeneous, twin-free microstructure with an average grain size of 25 μm . Here, grains are generally equiaxed, and scattered secondary particles ($\sim\text{Al}_8\text{Mn}_5$) align themselves along the rolling direction (RD) and are present in different lengths (1 to 30 μm) – note that the volume fraction of these precipitates is below 1%.

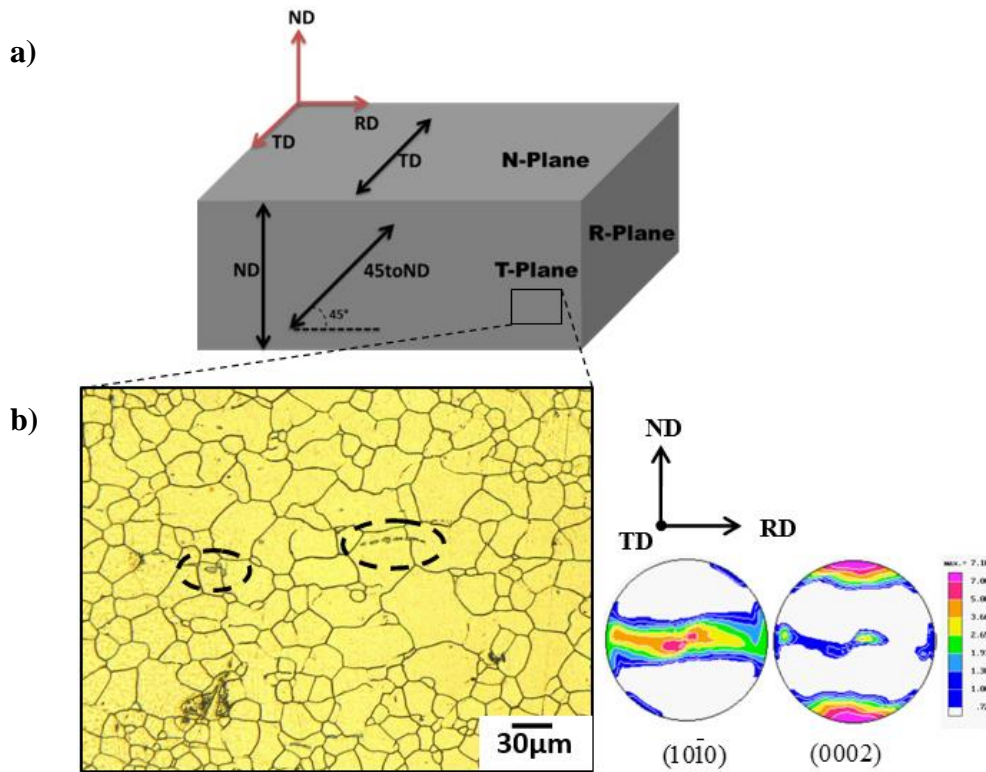


Figure 10. (a) Schematic of the starting material, a hot-rolled Mg-AZ31 plate. N-Plane: Normal Plane, T-Plane: Transverse Plane, R-Plane: Rolling Plane. TD: Transverse Direction, ND: Normal Direction, RD: Rolling Direction. (b) Metallography of the T-Plane. Dashed ovals capture secondary $\sim\text{Al}_8\text{Mn}_5$ particles. The corresponding pole figure demonstrates that the c-axes generally align along the ND, representing a typical plate basal texture.

After annealing, flat, dog-bone tensile specimens with gage sections sized $8 \times 3 \times 1.5 \text{ mm}^3$ were cut from the plate via wire electrical discharge machining (EDM) along the following three orientations: the normal direction (ND), transverse direction (TD), and 45° to the ND (referred to throughout the text as ‘45toND’). For clarity, these directions are depicted with respect to the plate in Figure 10a, where it can also be seen that the plate exhibits a typical strong basal texture (similar to Figure 2a) with the c-axes mostly aligned along the ND. It is worth mentioning that the tensile sample orientations were selected to activate different primary deformation mechanisms during loading at low temperatures, which is possible since the hot-rolled plate exhibits a strong texture. According to Schmid’s Law [64]:

$$\tau = \sigma \cos \varphi \cos \lambda = \sigma * m, \quad (2)$$

the critical resolved shear stress (CRSS) τ to activate a specific deformation mechanism during plastic deformation is dependent upon the Schmid factor m and the applied stress σ . Therefore, certain deformation mechanisms are favored under high Schmid factor m values, where φ is the angle between the direction of stress and the crystallographic glide plane normal and λ is the angle between the direction of glide and the direction of stress.

Here, the material investigated is a magnesium alloy plate with a strong basal texture (Figure 10b), which is reminiscent of a single crystal. Therefore, m from equation (2) can be utilized to determine which deformation mechanisms on average would be favored for different plate orientations with respect to the bulk basal texture. Utilizing Schmid factors, then, prismatic $\langle a \rangle$ slip is the most favorable mechanism during tensile loading along TD, basal $\langle a \rangle$ slip is the most favorable along 45toND, and tensile

twinning is most favorable along ND for the AZ31 hot rolled plate under tension at low temperatures. It is important to also recall that CRSS for magnesium is highly temperature dependent for non-basal slip systems such as prismatic $\langle a \rangle$ or pyramidal $\langle c + a \rangle$ slip [26]. Tension experiments were conducted in a servo-hydraulic MTS test frame at 25°C, 100°C, 150°C, and 200°C for each of the three orientations (ND, TD, and 45toND). Therefore, the flow stress features of basal slip, prismatic slip, and tensile twinning for AZ31 were captured as a function of (low) temperature. A constant strain rate ($5 \times 10^{-4} \text{ s}^{-1}$) was used for all tests, and an MTS high temperature extensometer measured axial strains.

After the tensile samples failed, they were water quenched to preserve the morphology along the fracture surface. The resulting microstructures at failure were examined via a Keyence VH-Z100 optical microscope (OM), an FEI Quanta-600 scanning electron microscope (SEM), and an FEI Tecnai G2 F20 ST transmission electron microscope (TEM). EBSD scans were conducted via a Zeiss Ultra Plus FEGSEM, which exhibits an Oxford Instruments Aztec EBSD system and a Nordlys-S EBSD detector. The accelerating voltage was set to 12 keV, and the aperture to 120 μm for EBSD data acquisition. The step size used to scan the areas of interest on the different samples varied between 300-100 nm. The pole figures of the bulk samples were measured with a Bruker-AXS D8 X-ray diffractometer with Cu K_{α} (wavelength $\lambda = 0.15406 \text{ nm}$) radiation.

To reveal the grain morphology along the fracture surfaces, OM and SEM samples were mechanically ground with SiC paper prior to polishing with 0.1 μm diamond paste. Afterwards, they were etched with an acetic-picric acidic mixture (20 ml acetic acid, 3 g picric acid, 20 ml H_2O , 50 ml ethanol (95%)). Furthermore, Nital (95% ethanol, 5% nitric

acid) was used to clean the sample surfaces of stains after etching with the acetic-picral mixture. EBSD sample polishing was equivalent to the OM and SEM cases, with an added final polishing step of 0.04 μm colloidal silica solution.

2.2 Tensile Flow Responses and Microstructures at Failure

In this section, the tensile flow responses and microstructures at failure will be analyzed systematically. Here, both results are presented together at a specific temperature for all orientations, in an effort to characterize the similarities and differences among samples tested at a specific temperature and favored by Schmid factor considerations (equation 2) to deform via either basal, prismatic, or tensile twinning mechanisms. In the next section (Section 2.3), the evolution of each individual deformation mechanism type with temperature is also analyzed to help clarify the role of temperature on various deformation mechanism activities. There, the influence of deformation mechanisms on the strength and ductility of magnesium for low temperatures will also be addressed, in an effort to bring everything together into a coherent summary while providing some suggestions for improved low temperature formability.

2.2.1 Tensile Flow Responses and Microstructure at Failure at 25°C

To begin, tensile flow responses at 25°C are shown in Figure 11a, where blue represents TD (prismatic slip), red represents ND (tensile twinning), and black represents 45toND (basal slip), and this coloring scheme is utilized from this point forward. The corresponding microstructures at failure for each specimen is provided in Figure 12, where

OM images and a macro-image of the samples tested after failure are included. For clarity, arrows connect the fracture surfaces shown in the OM images to their approximate locations in the macro-images, and the fracture surfaces (FSs) are marked by blue arrows. Note that this convention is repeated for the other temperatures. At 25°C, macro-images in Figure 12 show very little necking, as seen previously at room temperature [38, 65]. This indicates an inherently brittle fracture mechanism derived from the correspondingly difficult activation of non-basal slip modes at low temperatures. Magnesium alloys have been characterized as *quasi-brittle* at this temperature region, meaning failure occurs abruptly at onset of necking due to the inability of magnesium to uniformly deform [31].

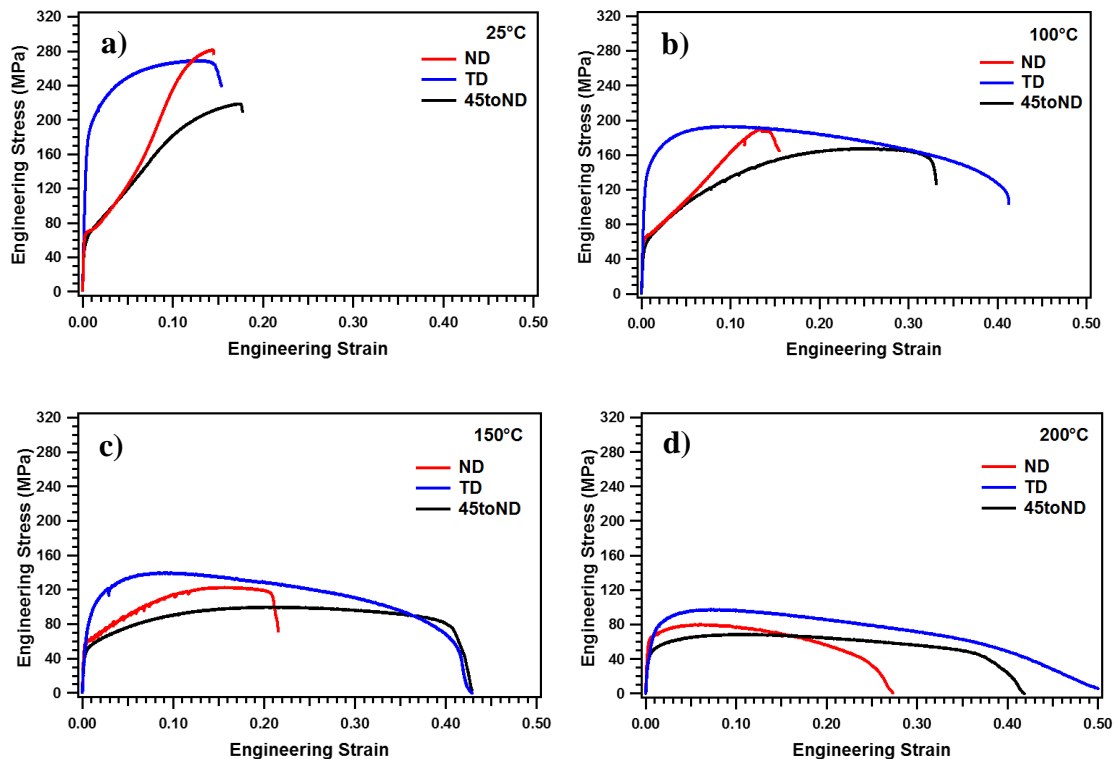


Figure 11. Engineering stress vs. engineering strain responses of Mg-AZ31 tension specimens tested along three different plate orientations: ND in red (tensile twinning), TD in blue (prismatic slip), and 45toND in black (basal slip). (a) 25°C, (b) 100°C, (c) 150°C, and (d) 200°C.

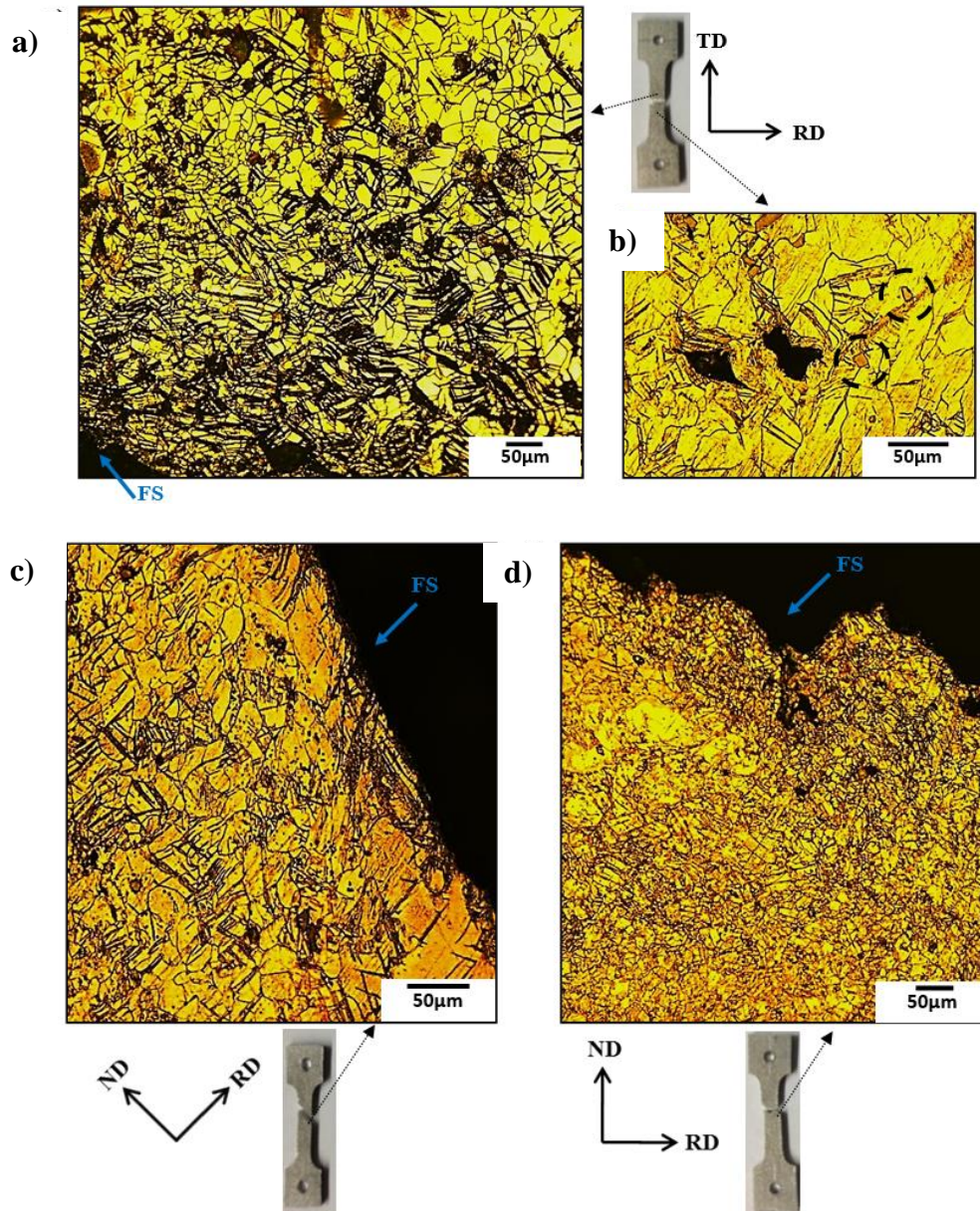


Figure 12. Metallography near fracture edges of samples tested at 25°C with macro-images of tested samples. (a) and (b) correspond to TD. In (b), voids are evident along twins; $\sim\text{Al}_8\text{Mn}_5$ particles encircled in black. (c) corresponds to 45toND and (d) corresponds to ND. FS: Fracture Surface.

Looking at the tension curves in Figure 11a, the TD sample exhibits a much higher yield stress in comparison to both ND and 45toND. Similar trends were also observed for

compression of AZ31 at room temperature, where generally the same deformation mechanisms were prominent [65]. These findings parallel magnesium single crystal studies where prismatic slip exhibits a higher CRSS than both basal slip and tensile twinning, particularly at room temperature [26]. Therefore, the yield stress discrepancies indicate that prismatic slip is indeed active for TD, with inhibited basal slip as these basal planes are nearly parallel to the loading axis and exhibit low Schmid factors [34]. Proust *et al.* also observed prismatic slip – despite its temperature dependence – to contribute significantly to room temperature deformation of a rolled AZ31B plate [32]. For the other samples, comparing strain hardening levels, as well as yield stresses, suggests that basal slip and tensile twinning appear primarily active for 45toND and ND, respectively. The effect of strain hardening will be discussed next in greater detail.

Among the samples, the ND specimen exhibits both the highest twin fraction and the most pronounced strain hardening (Figure 11a), where due to the high density of twin boundaries grains appear refined (Figure 12d). Strain hardening is correlated with tensile twinning activity [22, 37], which reorients the c-axes 86.3° away from the tensile axis. This in turn creates a Schmid factor favoring hard, non-basal slip systems that are inhibited by twin boundaries [25, 37], resulting in higher stress levels during testing. Therefore, strain hardening results from twinning and slip interactions [32]. Knezevic *et al.* [66] argued that tensile twin boundaries do not contribute much to work hardening, but rather the strain hardening primarily results from texture hardening effects; other studies showed

that strain hardening is attributable to an abundance of different dislocation types within the twinned region [23].

Despite the debate, it is commonly accepted that high strain hardening leads to high stress values under twinning, which in turn can lead to stress concentrations, instabilities, and early, abrupt failure [25]. Such an understanding is generally consistent with the results presented here; all flow curves show a prominent amount of strain hardening (Figure 11a), and in Figure 12, an abundance of twin boundaries can be seen in the microstructures for all samples. Moreover, for all samples twinned regions are most prevalent in areas near the fracture surface, thereby correlating twinning activity with brittle failure.

Regarding twinning, several unique features are evident for the TD condition in particular. Note that while prismatic slip is favored for the TD loading, it cannot accommodate c-axis strain. As tension along the TD promotes c-axis compression, either pyramidal slip or compression twinning is necessary to accommodate this deformation. Therefore, tensile twinning should not occur as extension along the c-axes is not favored. With this in mind, the TD twins observed in Figure 12a-b are most likely compression twins rather than tension twins. Also, the presence of twins indicates that pyramidal slip was not activated at 25°C.

From Figure 12a, a large proportion of these twins exhibit thick boundaries characteristic of double twins [33]. In contrast, pure compression twins usually are thin and difficult to index [27, 66]. Under similar test conditions (room temperature deformation, c-axis compression, and a high strain level), Barnett *et al.* [35] observed a

very similar twin morphology to the one shown in Figure 12a, and they identified these twins as double twins. Furthermore, micro-voids originate within twinned regions for the TD sample (e.g. in Figure 12b), and propagate throughout the sample into very large cracks (not shown). Therefore, failure is likely to have occurred sequentially in the TD specimen via compression twin nucleation and growth, followed by double twinning and strain localization along double twinned regions, leading to void formation and later fracture. A similar mechanism regarding compression twinning and failure was previously reported [35], and many studies have observed crack formation due to double twinning activity [31, 38, 67].

Interestingly, post-yield strain hardening is least pronounced in the TD case (Figure 11a), perhaps a consequence of compression twinning activity rather than tensile twinning activity, as seen in the other samples. This is feasible, as compression twinning causes a lower rotation angle (56°) than tensile twinning (86.3°), allowing for softer mechanisms to be active thereafter. Indeed, tensile twinning has a low CRSS and occurs readily in compression twins to create double twin regions, which result in a net 38° c-axis rotation in turn favorable for basal slip [27, 35, 38]. In addition, Ando *et al.* [38] showed the Schmid factor is high for basal slip inside double twins, where there is a long slip length allowing for shear localization. Conversely, the Schmid factor is low for pure tensile twins, where there is a comparatively small slip length that limits shear [38]. Given the above reasoning, shear can localize more readily in double twin regions than in tensile twin regions, allowing for void nucleation and growth in the former whereas instability, stress concentrations, and abrupt failure occurs for the latter.

The ease for basal slip inside double twin regions is known to result in strain incompatibilities between the twin interior, where basal slip is soft, and the surrounding matrix, resulting in void nucleation along twin boundaries [31]. Therefore, the mechanism for surface relief (void formation) is related to the localization of shear in these double twin regions. Also, regions where a sharp difference in Schmid factor between basal slip and prismatic slip were observed to be preferential sites for grain boundary sliding, as reported for a coarse-grained AZ31 specimen deformed at room temperature [68]. Grain boundary sliding was not investigated in the current work, but its contribution to strain at low temperatures along twin boundaries poses an interesting research question.

As mentioned, large cracks that nucleated from twin regions and grew continuously were a unique feature of the TD sample. In contrast, only a few voids were observed in the twinned regions near the fracture surface for the 45toND and ND cases (Figure 12c-d), resembling an abrupt, discontinuous fracture triggered by localized instabilities [31]. Note that at room temperature tensile twinning does not promote void formation [29, 67]. As such, for the ND and the 45toND samples tested at 25°C, fracture appears to occur along twin and grain boundaries (Figure 12c-d). These twins are believed to be tensile twins, which are generally easier to activate than compression or double twins [40]. In addition, tensile twinning rather than compression twinning is favorable for ND and 45toND, while the opposite is true for TD.

It is also worth mentioning that failure was not associated with the Al_8Mn_5 particles, as indicated by the absence of cracks near the particles encircled in black in Figure 12b. Secondary particles have been reported to have a larger impact on failure at

higher temperatures, whereas voids along their interfaces were not observed previously at ambient temperature [31]. Note also that DRX grains were not observed at 25°C. The aforementioned failure types (shear localization for the TD sample and segmentation at twin and grain boundaries for both the ND and 45toND cases) are characteristics of brittle fracture as well, and the low ductility levels from Figure 11a confirm this sentiment.

As an interesting side note, shear bands with compression and double twins were also observed for pure magnesium while tested at room temperature, and were deemed to initiate a premature failure via strain localization along these regions [20]. However, the addition of RE-elements can relax the texture, promoting more homogeneous shear band formation by activation of profuse twinning types [20]. Therefore, if all variants of tensile and compression twins could be activated simultaneously, an enhanced ductility could be potentially achieved at room temperature for AZ31.

2.2.2 Tensile Flow Responses and Microstructure at Failure at 100°C

When the temperature increased from 25°C to 100°C, only TD showed macroscopic necking (Figure 12, Figure 14). Likewise, TD exhibits the best ductility – ~40%, closely followed by 45toND (Figure 11b). Rodriguez *et al.* [31] also observed limited necking at room temperature, with increased necking at 100°C. As TD has a significantly higher yield stress than ND and 45toND at 100°C, prismatic slip remains primarily activated in TD, while tensile twinning and basal slip are primarily active in the latter two samples, respectively (Figure 11b).

Among the samples, ND showed the highest strain hardening coupled with the lowest ductility (~15% in Figure 11b). While ND shows an immediate, significant strain hardening effect, it is more gradual for 45toND, where over twice the strain was obtained. This can be explained as follows: the Schmid factor for basal slip is much higher in 45toND than ND, as in ND the basal planes are generally normal to the loading axis and limited to movements along the $\langle a \rangle$ planar directions (i.e. along the N-Plane in Figure 10). Furthermore, ND possesses a high propensity for tensile twinning, which reorients the basal planes by 86.3° away from the loading axis (under tension) to directions that continue to inhibit deformation by basal slip [37]. While the Schmid factor for the reoriented grains favor prismatic slip (similar to TD), quasi-brittle fracture prevails, resulting in a low ductility of ~15% in Figure 11b.

As strain hardening is indicative of tensile twinning activity, the volume fraction of extension twins should be highest in ND, followed by 45toND and, finally, TD. With this in mind, several unique features for the ND at 100°C can be seen in the microstructure (Figure 13). Here, a high volume fraction of twins is obvious, whose boundaries are so numerous that they obscure the grain boundaries. These twin boundaries appear to coalesce into large shear bands throughout the specimen, as indicated by the ellipses in Figure 13a; in addition, large, discontinuous voids are prominent at the fracture surface. It is worth mentioning also that no DRX grains are observed in the microstructure, even in the shear bands and twins (Figure 13b-c). Also, the role of secondary $\sim\text{Al}_3\text{Mn}_5$ particles on failure is minimal, as there are no obvious cracks along these particles (encircled in white in Figure 13c).

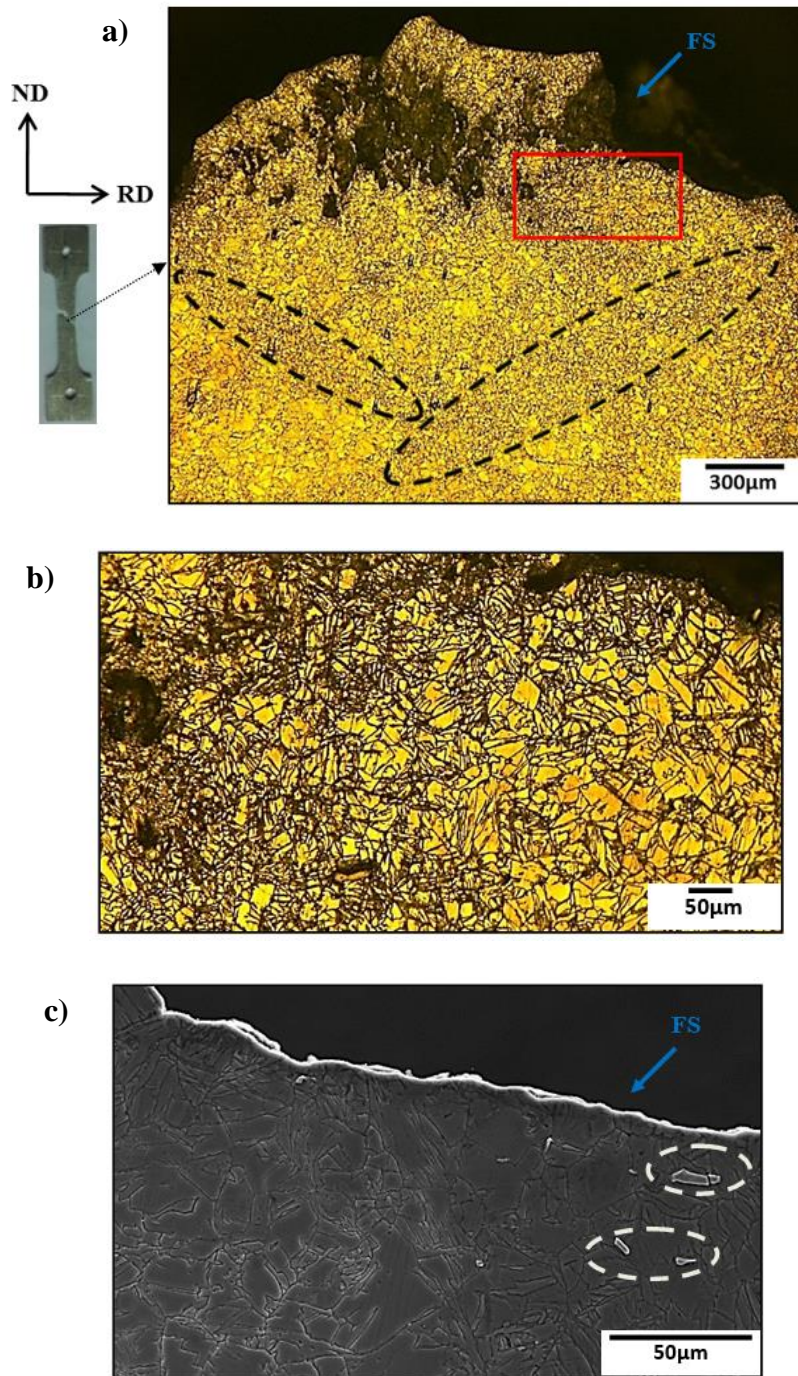


Figure 13. Metallography near fracture edge of ND at 100°C, with a macro-image of the tested specimen. In (a) shear bands are seen to form (annotated in black). In (b), a zoomed in image of (a) according to the red square, twinning activity is obvious. (c) shows no obvious DRX regions; Al₈Mn₅ particles are encircled in white. FS: Fracture Surface.

From Figure 11b, it appears that failure via tensile twinning for ND at 100°C occurred sequentially, as a series of events which lead to a quasi-brittle, catastrophic failure. In this regard, the rapid amount of strain hardening indicates tensile twinning activated immediately and reoriented the grains to unfavorable textures for soft slip [37]. Afterwards, stress concentrations and strain incompatibilities likely occurred at regions with high twin fractions (Figure 13a), and once the stress levels became high enough, failure occurred catastrophically. Here, tensile twinning appears to have been incapable of accommodating higher strains, resulting in grain pull-outs along grain and twin boundaries (Figure 13a).

In contrast, the TD specimen tested at 100°C (Figure 14) shows grains mostly elongated along the tensile axis, resembling a slip-dominated deformation. Unlike ND, twins are present only near the fracture surface (Figure 14). As these twins are thick – similar to the double twins observed for TD at 25°C – and pass across the elongated grains (Figure 14b), double twinning appears to occur *after* sample necking for TD, and subsequently leads to failure. Under similar testing conditions, Zhou *et al.* [63] also showed grains elongated along the loading axis prior to failure, yet in their study no twins were evident (the post-failure microstructure was not shown). As such, this reinforces the argument that the twins in Figure 14 formed late in the deformation process.

In addition, Jiang *et al.* [37] quantitatively demonstrated that compression and double twins become less common when increasing temperature from 25°C to 100°C. Likewise, the volume fraction of twins and the number of voids which nucleated from twinned regions was significantly lower in TD tested at 100°C vs. 25°C (Figure 14 and

Figure 12, respectively). This observation indicates that compression twinning – followed by double twinning, void nucleation, and growth – was relatively suppressed at 100°C, allowing for enhanced ductility. Also, the temperature increment from 25°C to 100°C may allow pyramidal $\langle c + a \rangle$ slip to compete more easily with compression twinning for c -axis compression [69].

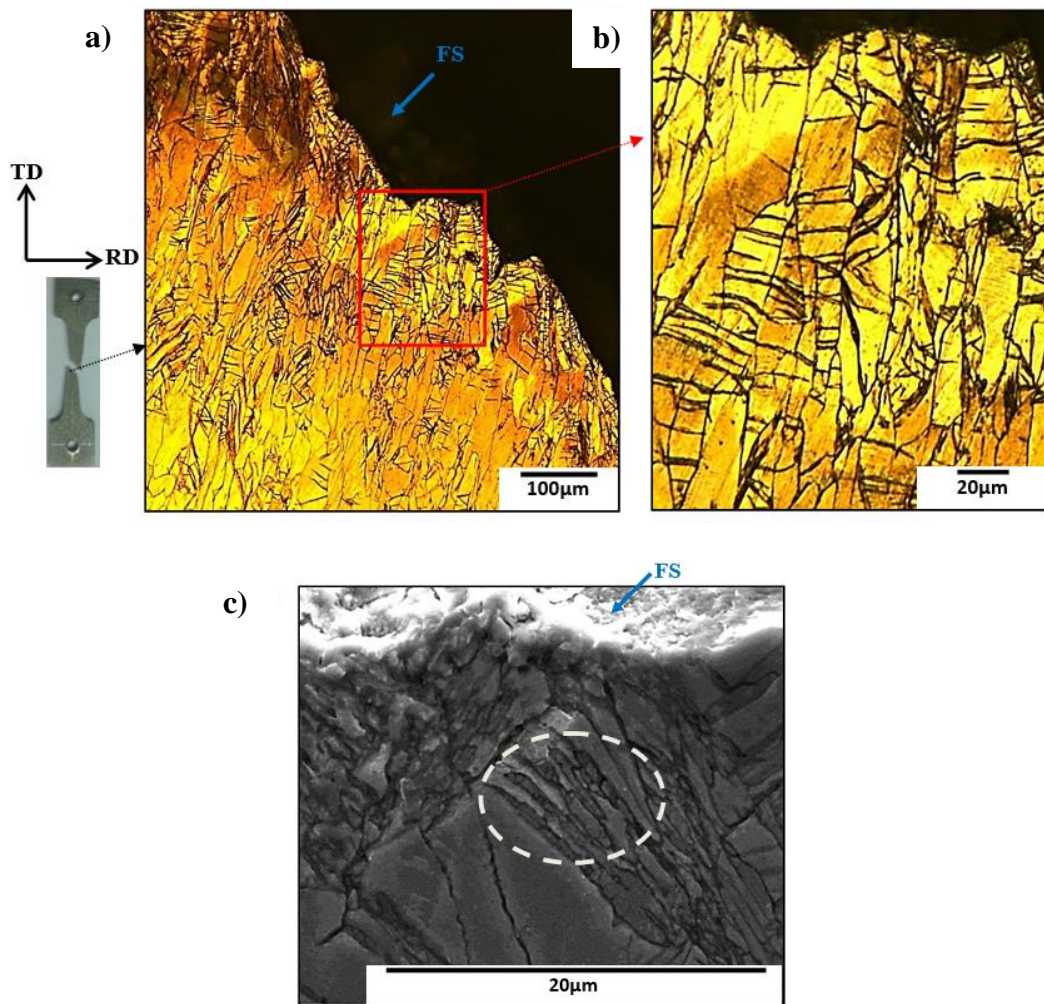


Figure 14. Metallography near the fracture edge of TD at 100°C, with a macro-image of the tested sample. (a-b) show twins localized near the fracture edge. (c) shows DRX grains evident within twins. FS: Fracture Surface.

Given the evidence, the mechanism for failure for TD at 100°C is proposed next. First, prismatic slip occurred readily allowing for grain elongation, and compression and double twinning activity were inhibited until the onset of necking. At this point, stress concentrations at the necked region appear to activate compression twinning, as observed previously in Ref. [37], leading to double twinning followed by shear localization and failure similar to TD at 25°C. Here, DRX grains were observed in the microstructure exclusively within the twin regions at the fracture surface (e.g. encircled in white in Figure 14c), characteristic of TDRX [43] and suggesting that shear localizes within double twins prior to fracture. Rodriguez *et al.* [31] also observed void formation as a mechanism for failure for AZ31 for the same general test conditions (temperature, texture, etc.), where cracks were seen to initiate at twins and precipitates.

In comparison to TD and ND, the failure mechanism for 45toND tested at 100°C is somewhat more complex due to more obvious interactions between tensile twinning and basal slip. Here, due to the high Schmid factor for both twinning and basal slip, many grains are twinned while also appearing more elongated in comparison to 45toND at 25°C. Interestingly, basal slip, tensile twinning, and even prismatic slip (following the 86.3° reorientation from tensile twinning) are favored deformation modes. Altogether, these constitute ~4.5 independent slip mechanisms, which is close to the required 5 independent slip mechanisms by Von Mises for homogeneous deformation. As mentioned above, the enhanced ductility appears due to the gradual activation of tensile twinning with basal slip, which is eased by the subsequent propensity for prismatic slip.

Regarding failure mechanisms, there are several cracks near the fracture surface (e.g. via the red arrow in Figure 15a). When analyzing such cracks at a higher magnification, DRX grains were found to nucleate inside twins (Figure 15b), where a micro-crack can also be seen along this boundary. Therefore, it is feasible that DRX grains allowed for additional strain accommodation along the twin boundaries at 100°C for 45toND, thereby extending the sample's ductility. Given the low temperature, DRX are not expected to make a significant contribution to strain [70], but here quasi-brittle failure along shear bands (as seen in ND at 100°C) were avoided perhaps as a result of DRX activity. DRX nucleation from twin regions at low temperatures have been reported before [70]. Given the sample orientation, this may be due to favorability for basal slip, or could be the result of favorability for prismatic slip following tensile twinning reorientations.

As a clear understanding of failure for 45toND remained elusive, EBSD was conducted to clarify the failure mechanisms and is shown in Figure 16. Here, several distinct features are discussed. First, notice that most twins observed are tensile twins, as expected given the earlier discussion. Also, from the inverse pole figure (IPF) map in Figure 16a, the c-axes reoriented significantly after tensile twinning, which is expected given the necessary 86.3° rotation from the ND around the tensile axis. Notice also that a few grains and subgrains were observed along twinned regions, as seen via white arrows and the white ellipse, respectively. These features resemble DRX grains similar to that observed in Figure 15b. An analysis of the grains in these regions confirmed the existence of DRX grains along the twin regions (not shown).

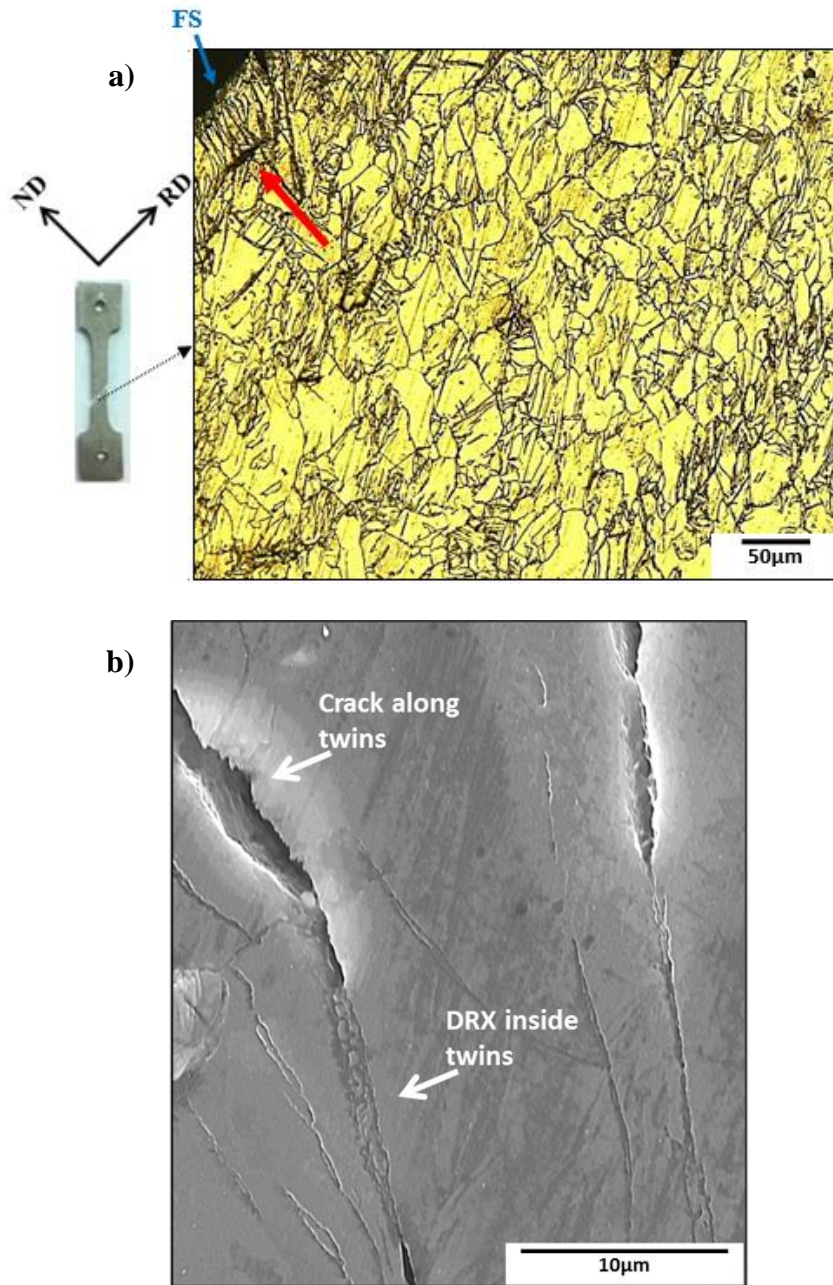


Figure 15. Metallography near the fracture edge of 45toND at 100°C, with a macro-image of the tested sample. (a) shows elongated grains with significant twinning activity near the fracture edge. (b) shows DRX within the twin boundary, where cracks have grown along twins. FS: Fracture Surface.

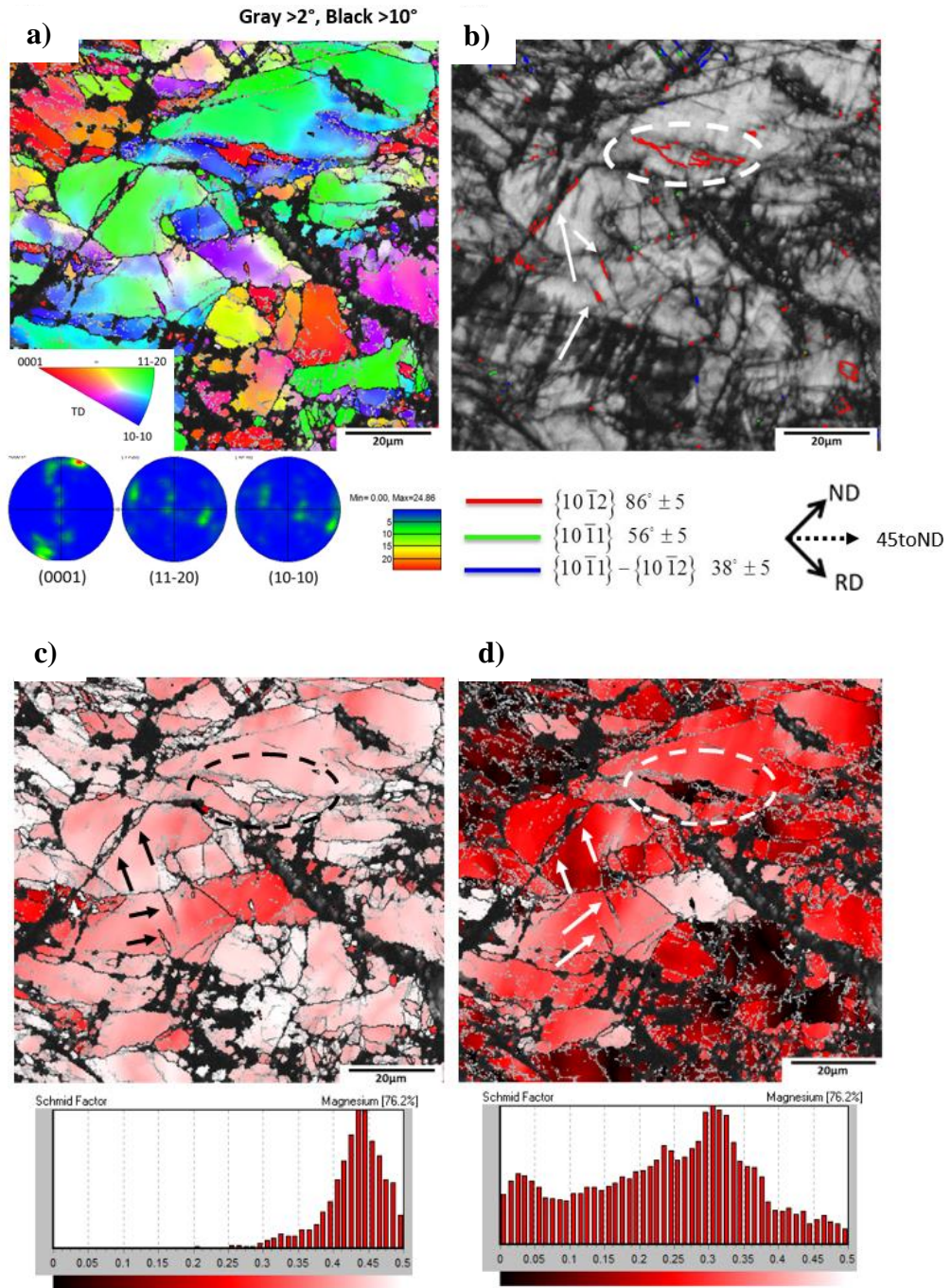


Figure 16. EBSD of 45toND at 100°C. (a) IPF with corresponding texture contour plot. (b) Map of indexed twin types: red = tension twin, green = compression twin, blue = double twin. (c-d) are Schmid factor maps for prismatic slip and basal slip, respectively.

From Schmid factor maps of the same area, the subgrains favor prismatic slip instead of basal slip immediately after twinning (follow the dashed ellipses in Figure 16c-d). However, once clear grain boundaries have formed – indicating the formation of DRX grains along the twin regions – basal slip is more favorable. This can be seen via the arrows in Figure 16b-d. Also, prismatic slip is possible along these regions, as seen via the black arrows in Figure 16c. Therefore, it appears that initially tensile twinning creates hard orientations for basal slip, yet due to the temperature (100°C) DRX grains nucleate within these twin regions with increasing strain. The resulting conversion from LABs to HABs increases favorability for basal slip, reminiscent of a CDRX mechanism. Consequently, strain accommodation occurred along the twin regions, both enhancing the stability along the twin regions while also localizing strain here. Therefore, catastrophic failure due to instabilities along twin regions were not observed at 45toND, in contrast to ND as seen in Figure 13. However, 45toND appears to experience strain localization along twin boundaries, leading to stress concentration and crack nucleation along soft DRX grains prior failure.

2.2.3 Tensile Flow Responses and Microstructure at Failure at 150°C

Once the temperature is increased to 150°C, the flow curves in Figure 11c exhibit an improved ductility, and other mechanical trends seen previously when going from 25°C to 100°C continue at 150°C. For instance, given the lower strain hardening at 150°C, deformation appears to have transitioned from primarily twinning dominant to slip dominant for 45toND and TD. For ND, strain hardening remains most pronounced. Also,

yield stress differences are consistent with lower temperatures, and contributions of DRX – which were first observed within twins at 100°C for TD and 45toND – to strain become more significant at higher temperatures, as expected from the observed latent softening in Figure 11c. The resultant interaction between DRX, slip, and twinning mechanisms is given significant attention in the current section. In this regard, 150°C represents an important transition temperature regarding formability for Mg-AZ31 [18], and deserves additional attention in comparison to the other temperatures (25°C, 100°C, and 200°C).

With this in mind, the microstructure near the fracture surface for TD at 150°C is captured in Figure 17, where grains are elongated (similar to 100°C in Figure 14) along the tensile axis. Double twins were not evident along the fracture surface at 150°C, unlike lower temperatures, and DRX grains surround elongated parent grains in a “necklace” type fashion. These necklace DRX are likely formed via CDRX [71], as it requires non-basal slip [42] which is favored for TD. Furthermore, DDRX is unlikely, as the characteristic serrated or bulging grain boundaries [2, 43, 44] are not obvious along DRX regions in Figure 17. Of course, the lack of twinning eliminates the TDRX mechanism from consideration. Thus, from 100°C to 150°C, a transition from TDRX to CDRX is seen for TD.

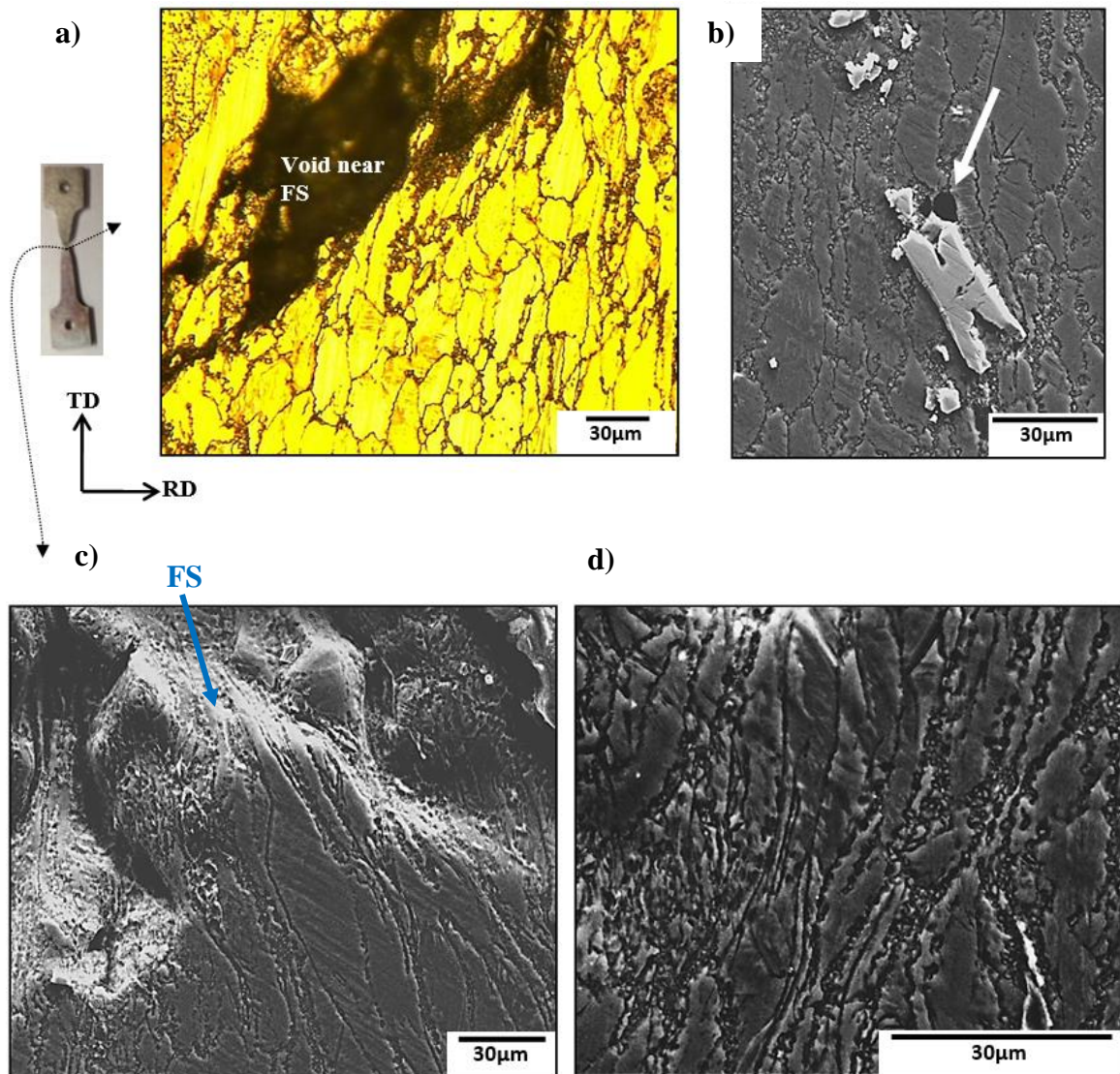


Figure 17. Metallography of TD at 150°C, with a macro-image of the tested sample. (a, c) show voids formed along necklace DRX regions at the fracture surface. (b) shows voids along $\sim\text{Al}_8\text{Mn}_5$ precipitates. DRX are also visible away from the fracture surface (d). FS: Fracture Surface.

Regarding failure mechanisms, strain appears to localize along the necklace DRX regions, where voids form and coalesce (Figure 17a and c). A few voids were sometimes observed along $\sim\text{Al}_8\text{Mn}_5$ particles (e.g. see the white arrow in Figure 17b) as well, but the

low volume fraction of these particles minimized their contributions to failure. In general, the TD case at 150°C exhibits high ductility and ductile failure via void nucleation and coalescence.

To gain more insight into deformation mechanisms and validate previous assessments made from Figure 17, EBSD maps were captured near a void and are included in Figure 18. Here, the image captures the N-Plane (recall Figure 10), which is parallel to the basal planes prior deformation. For comparison purposes, the initial location of the basal planes is indicated via a black dashed circle in Figure 18a. In the EBSD contour map, the basal planes post deformation are oriented similarly to their initial condition, showing that prismatic slip and DRX does not significantly alter the texture [11]. Notice also that very few twins post-deformation were indexed in Figure 18b, indicating that any observed texture evolution occurred free of twinning activity. Indeed, the minimal texture evolution after deformation is consistent with the absence of twinning, which exhibits large reorientations of the basal poles [22, 35].

Therefore, it is clear from Figure 18 that deformation along TD at 150°C is slip-dominated, with no significant contributions from twinning modes. A Schmid factor map for pyramidal $\langle c + a \rangle$ slip was constructed for this EBSD map (not shown here), where the Schmid factor values were all greater than 0.30. Therefore, given the temperature and favorable Schmid factors – and also the absence of compression twins – pyramidal slip was likely active here to accommodate the expected c-axis compression. The propensity for pyramidal and prismatic slip for TD further supports the argument that the DRX grains formed via CDRX [42]. Additionally, evidence for CDRX is found via the gray subgrain

boundaries (i.e. LABs) within interiors of the larger parent grains (Figure 18a). These LABs may accumulate with higher strain levels, eventually forming HABs which finally convert to DRX grains [43].

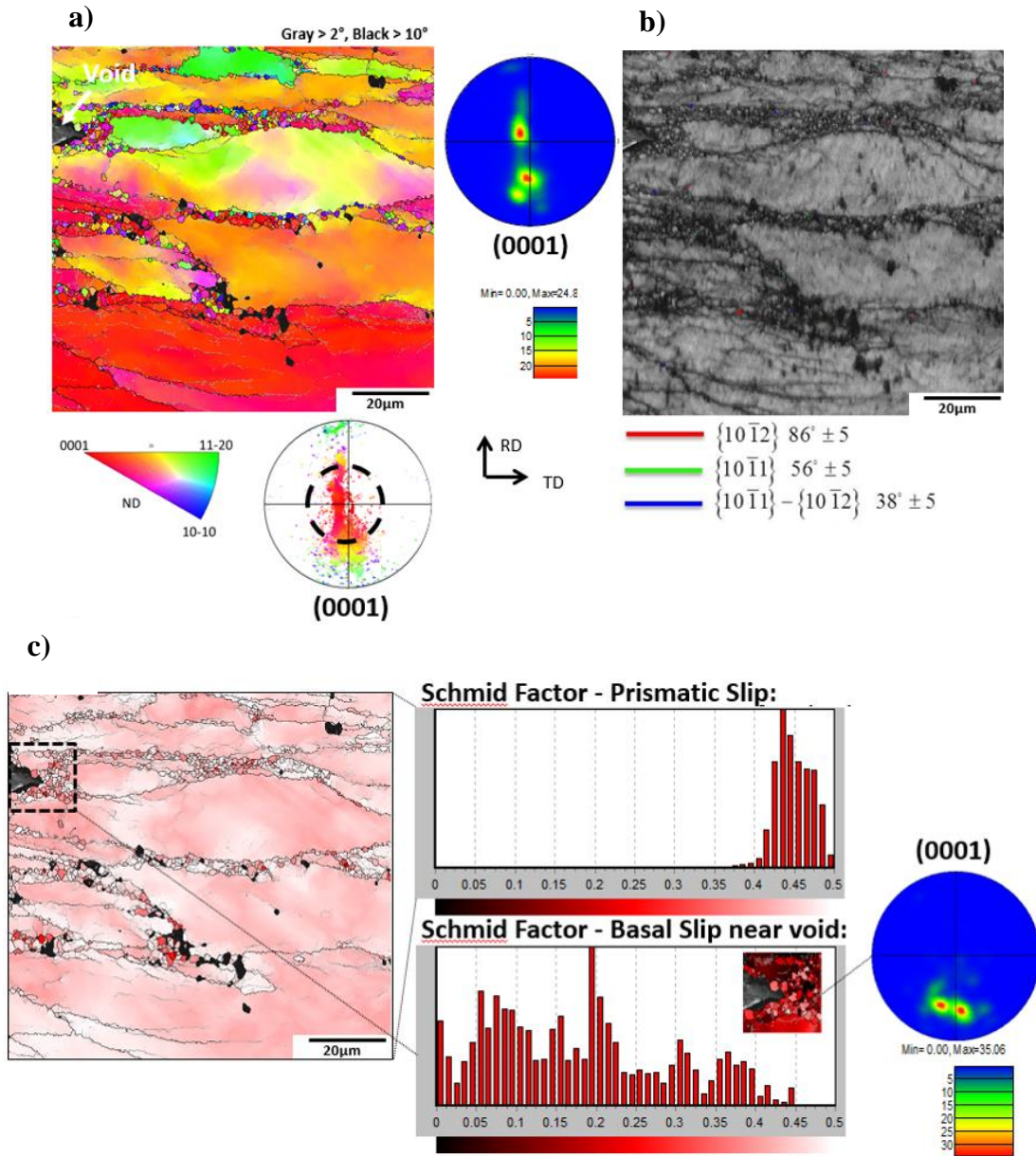


Figure 18. EBSD of TD at 150°C. (a) IPF map with corresponding basal plane textures, (b) indexed twins, (c) Schmid factor map for prismatic slip (for entire image) and basal slip (for dashed inset area near void), with corresponding basal plane texture for the latter.

A key interest regarding TD at 150°C is identifying the mechanism for void nucleation and failure in a characteristically slip-dominant, ductile deformation process for AZ31. Regarding the impact of various slip systems on void formation, Schmid factor maps were analyzed to check post-mortem propensity for basal $\langle a \rangle$, prismatic $\langle a \rangle$, and pyramidal $\langle c + a \rangle$ slip throughout the region. In this regard, only the Schmid factor map for prismatic slip is shown (Figure 18c). Here prismatic slip clearly remains favored throughout the region, which reflects the limited texture reorientation from prior prismatic slip (Figure 18a). In comparison, basal slip showed the lowest Schmid factors (averaging ~0.15).

In an attempt to clarify the effect of DRX on void formation, a portion of a void is captured in Figure 18c via the dashed square, where Schmid factor analyses were conducted for basal slip and are included here with the Schmid factor map as an inset. Here, grains near the void show some propensity for basal slip and are oriented around the TD axis towards the negative RD direction. Essentially, their texture deviates from the majority. Therefore, it appears that DRX grains near voids allow for slight strain accommodation prior to void formation. Ion *et al.* [41] argued that at low temperatures, shear zones form from necklace DRX regions, where soft basal slip localizes strain. They postulated that localized strain at geometrical soft DRX regions led to stress localizations at grain tips, which was relieved by void formation [41]. In the current study, a similar argument can be made, as basal slip is slightly more favorable along DRX regions where texture deviates from the bulk, indicating that strain localizes here prior to void formation (Figure 18c).

Figure 19 captures the fracture edge of the ND at 150°C case, where $\sim\text{Al}_8\text{Mn}_5$ inclusions (e.g. encircled in white) did not appear to impact the deformation process. Tensile twinning is prevalent throughout the sample (Figure 19a), and as the few grains without twins appear more elongated than at lower temperatures for this orientation, slip modes appear more active at 150°C. Near the fracture surface, Figure 19b shows necklace DRX grains (e.g. by the red arrows), a new feature that was not seen at lower temperatures for ND. Unlike TD at 150°C, voids are not observed along these DRX regions. The presence of twins appear to promote brittle failure along the twin boundaries, with low amounts of sample necking (Figure 19) and ductility $\sim 20\%$ (Figure 11c).

To better characterize the deformation process for this sample, EBSD maps for a larger area (Figure 20) and a smaller area (Figure 21) are shown as well. Here, we focus first on the large area (Figure 20), where the IPF map shows a region captured near a crack, as indicated via the white arrow. In Figure 20b, the twins indexed were primarily extension twins, and the texture appears reoriented significantly from the initial orientation (indicated by the black dashed ellipses in the contour plot). Note here that tensile twinning has been reported to reorient the c-axes under tension by 86.3° away from the tensile axis [37]. Similarly, after failure the basal planes have aligned parallel to the ND in Figure 20. Orientations of the large ($d > 5 \mu\text{m}$) and refined ($d < 5 \mu\text{m}$) grains were captured as well in Figure 20c-d. Here, the c-axes of large grains have realigned normal to the ND, but the refined grains are oriented differently (Figure 20d). The orientation of the refined grains is similar to the As Received basal texture, indicating that these grains are not twins but

rather DRX grains. Furthermore, DRX cannot contribute significantly to texture evolution [11], as was seen earlier for necklace DRX in TD at 150°C.

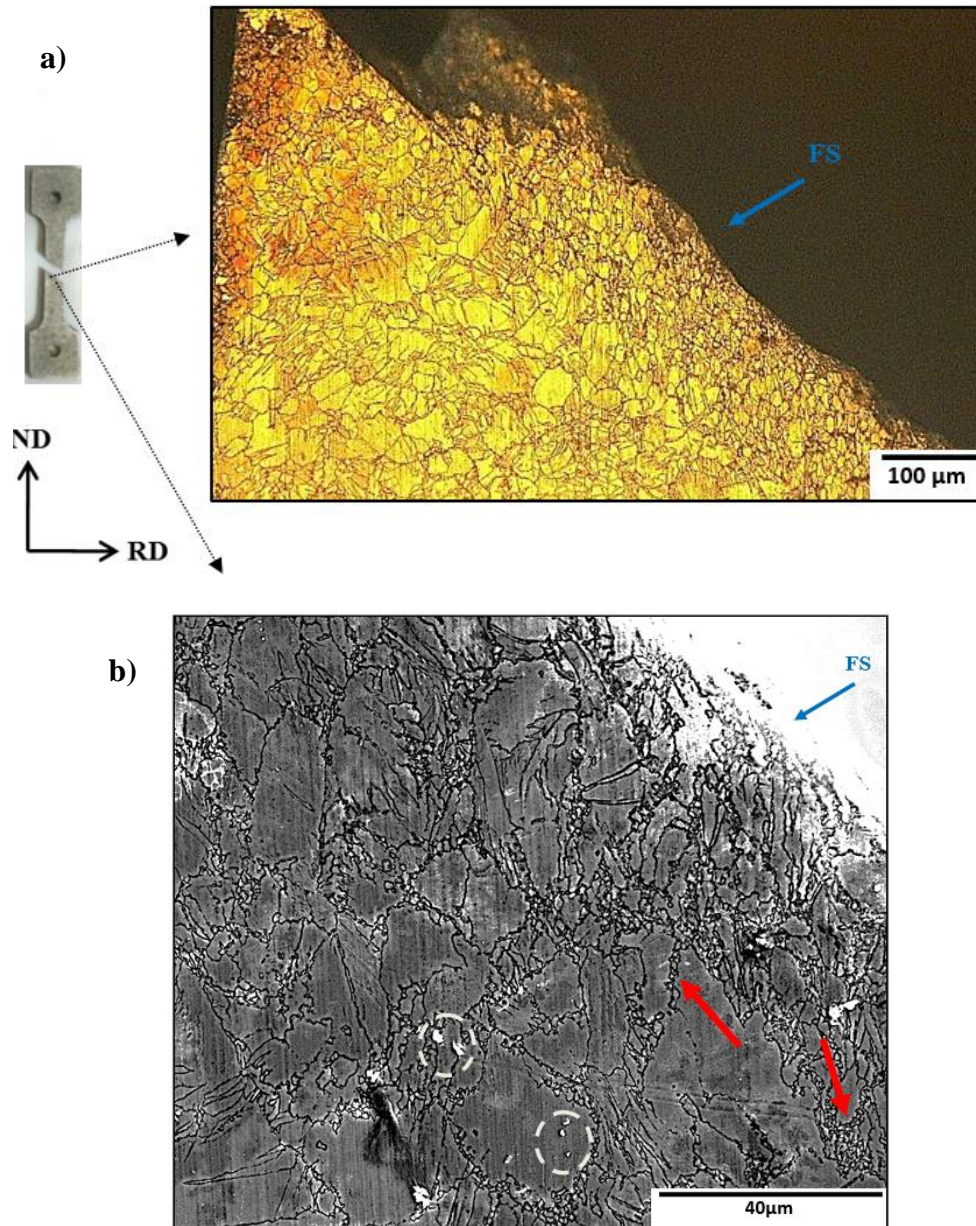


Figure 19. Metallography of ND at 150°C, with a macro-image of the tested specimen. (a-b) show prominent twinning activity, (b) also shows DRX grains near the fracture edge (red arrows). No cracks were obvious along the $\sim\text{Al}_8\text{Mn}_5$ secondary particles (encircled in white). FS: Fracture Surface.

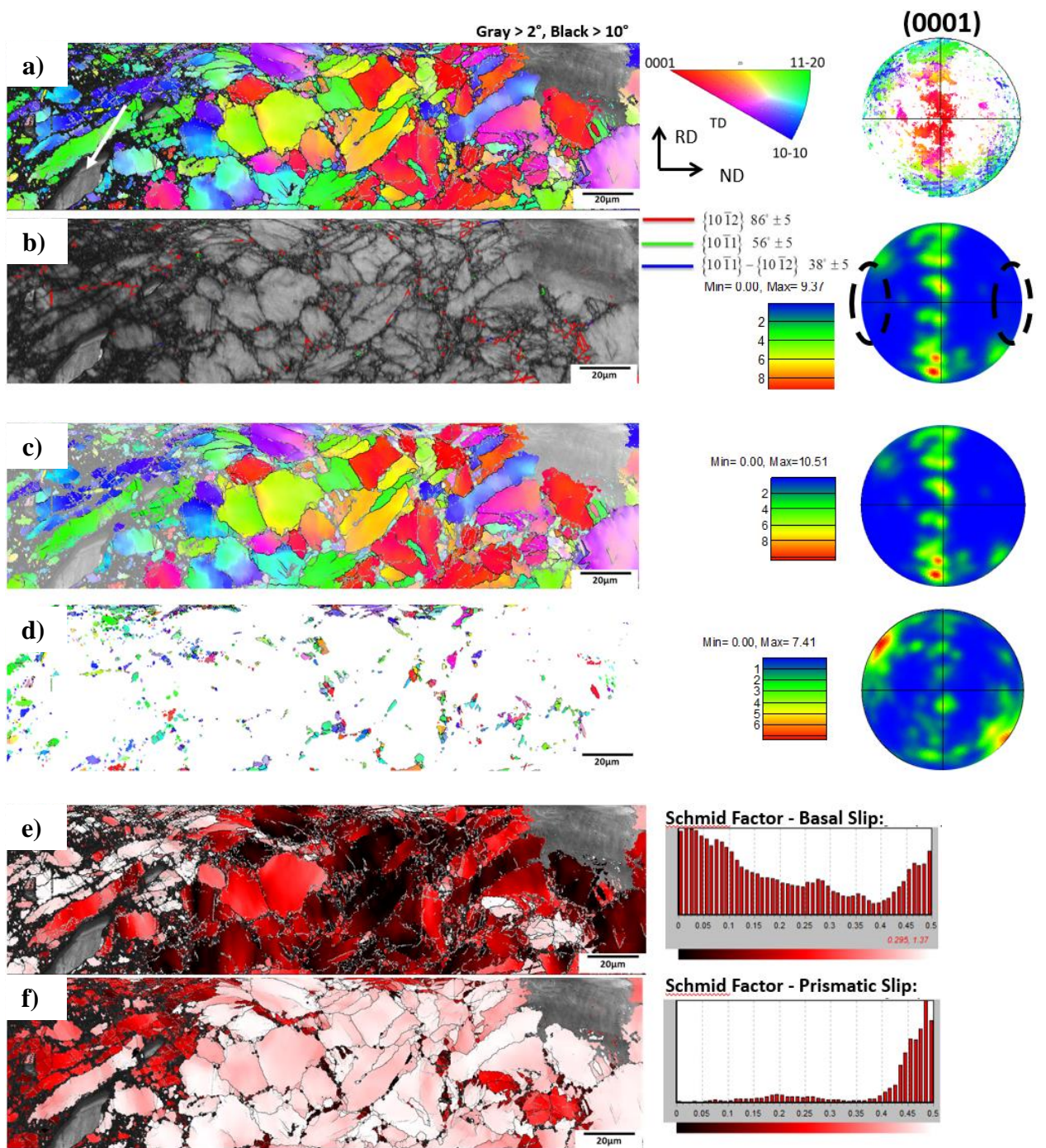


Figure 20. Large area EBSD map of ND at 150°C. (a) IPF map, (b) indexed twin boundaries and pole figure corresponding to (a), (c) Large grains and corresponding texture, (d) Refined grains between 0.4-5 μm and corresponding texture. (e-f) show Schmid factor maps and values for basal and prismatic slip, respectively. All pole figures capture the basal plane.

Schmid factor maps are also shown in Figure 20e-f, where the grains generally favor prismatic slip, which is expected given the reorientation of the basal planes from tensile twinning (Figure 20b). Also, recall Figure 11c, where at high strains the ND at 150°C demonstrates a similar strain hardening to TD where prismatic slip was dominant. Interestingly, grains to the left of the crack show a higher propensity for basal slip than prismatic slip (Figure 20e-f). This could be due to reorientations from the cracked region. Given the propensity for prismatic slip, it is likely that the mechanism behind necklace DRX grains formation was CDRX [42], similar to TD, yet the presence of twinning complicates interpreting the DRX mechanism. Therefore, the DRX mechanism will be discussed next in greater detail.

In order to more accurately capture orientations of the DRX grains, a smaller area was mapped in EBSD in Figure 21, where a step-size of 0.1 μm was utilized. Here, there are several features worth mentioning that are consistent with the larger image in Figure 20. First, the twins indexed are primarily tensile twins, and c-axes have reoriented $\sim 86.3^\circ$ from the ND axis (Figure 21a). Additionally, the Schmid factor maps show that there is inhomogeneity in the region in terms of favorable slip modes. In this regard, some regions are more favorable for prismatic slip, while others are more favorable for basal slip (Figure 21d-e). Finally, fine grains ($< 5 \mu\text{m}$) are oriented differently from the large grains, as also observed for the large area (Figure 20).

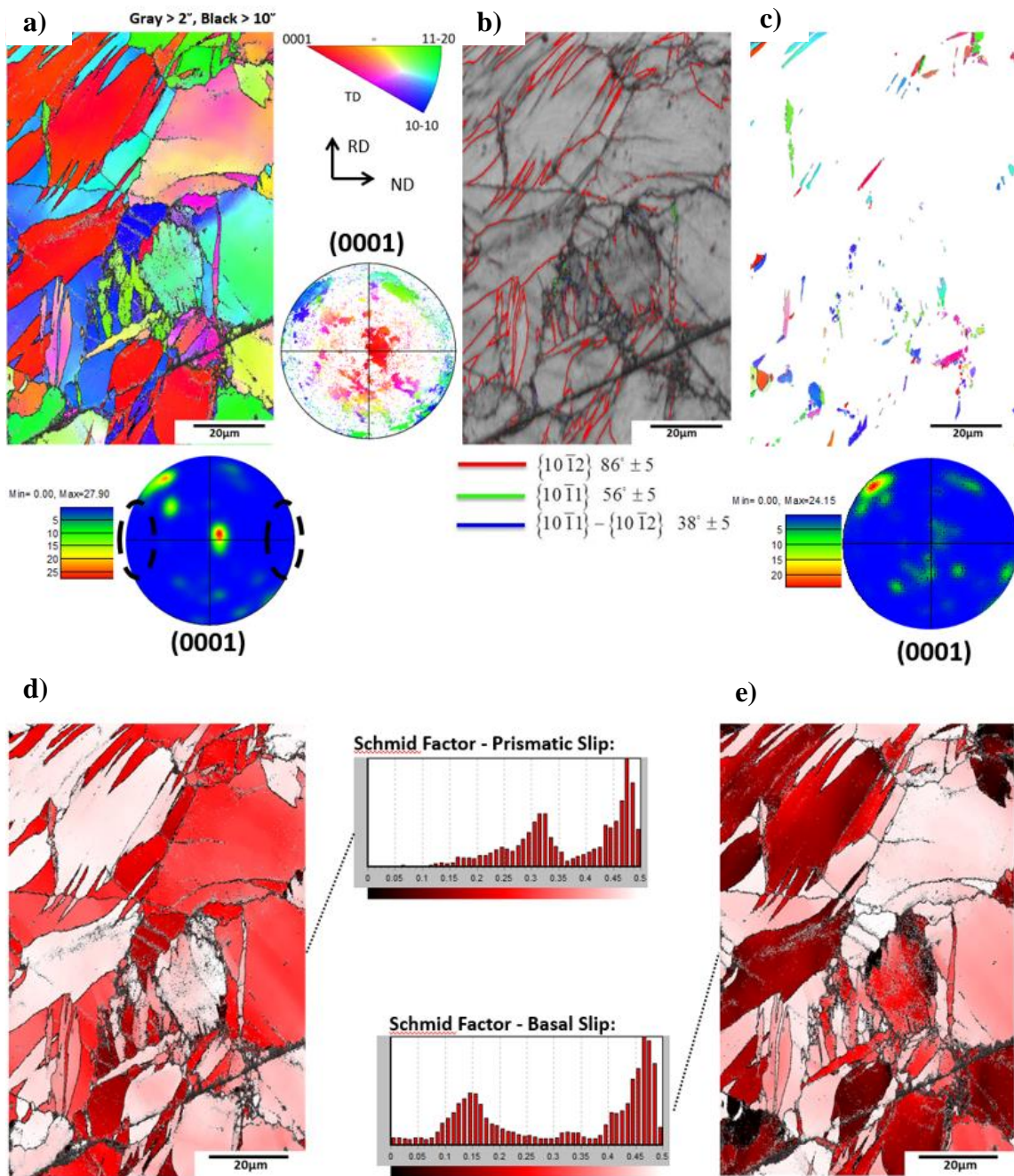


Figure 21. Small area EBSD map of ND at 150°C. (a) IPF map with corresponding texture, (b) Indexed twins, (c) IPF and texture of refined (0.4-5 μm) grains, (d-e) Schmid factor map and values for prismatic and basal slip, respectively.

Evidently, the refined grains captured in Figure 21c are sometimes located along twinned regions. One could argue that TDRX should dominate for ND at 150°C given both its high volume fraction of tensile twins and the existence of refined grains along twin regions, yet a method to distinguish TDRX grains from twinned grains is via their texture, as pure tensile twinning results in an 86.3° reorientation [39]. In contrast, TDRX can further modify the texture, reorienting the c-axes of parent tensile twins by anywhere between 30° and 70° relative to the axis of deformation [39]. Since DRX grains in Figure 21c are mostly oriented similarly to the initial basal texture – rather than 86.3° away from the tensile axis – they may have formed as TDRX and afterwards reoriented the parent grains. On the other hand, DRX grains are likely not restricted to forming solely via TDRX, as the serrated and bulged grain boundaries visible in Figure 21 are indicative of DDRX [43]. Furthermore, given the necklace DRX grains in Figure 19 near the fracture surface, CDRX may be active also at grain boundaries [19]. In short, a clear mechanism for DRX is unclear for ND at 150°C.

Likewise, the mechanism for failure is complex for this condition. Here, the large reorientations due to tensile twinning create huge local mismatches in Schmid factors for different deformation mechanisms (Figure 20e-f, Figure 21d-e). Therefore, certain regions can favor hard prismatic slip, while other regions inhibit it and instead promote soft basal slip. Furthermore, the mechanism for DRX grain formation is unclear, given evidence for DDRX, CDRX, and TDRX. Clearly, the propensity for a variety of slip mechanisms (basal, prismatic, and pyramidal) along with tensile twinning for ND result in a complicated interaction between all of these mechanisms. Also, as DRX mechanisms are

linked to the active deformation mode [43], a single mechanism behind DRX cannot be justified for ND at 150°C. Regarding fracture, the localized favorability for different slip modes throughout the sample (i.e. seen via Schmid factor maps), coupled with the propensity for tensile twinning, would seemingly promote localized instabilities. Therefore, catastrophic failure should be likely between such regions, and this interpretation is supported by crack formation between the basal and prismatic favored regions in Figure 20. Furthermore, a low strain to failure in comparison to 45toND and TD coupled with limited ND sample necking (Figure 11c and Figure 19) are indicative of a relatively catastrophic, quasi-brittle failure for ND at 150°C.

Finally, the 45toND case exhibited mild strain hardening at 150°C, with a strain to failure similar to TD and a comparatively lower yield stress reflective of the different CRSS values for basal and prismatic slip (Figure 11c). Metallography for 45toND is shown in Figure 22, where grains generally appear elongated and failure is seen to occur via cracks along the DRX regions (see Figure 22a). DRX grains appear both as necklace type (Figure 22c) and also within the twins (encircled in white in Figure 22b) – recall that the latter feature also occurred at 100°C for this orientation. Throughout the sample, twinning activity is prominent and DRX grains are seen to coalesce into shear bands where cracks were observed (Figure 22a and c). The presence of twins, DRX, shear zones, and cracks characterize the nature of failure in the 45toND case at 150°C. Of course, given its high elongation to failure (~40%), ductile rather than brittle fracture is obvious, and cracks initiate along DRX regions (Figure 22a), a feature reminiscent of TD at 150°C (Figure 17) which was explained via the mechanism proposed by Ion *et al.* [41]. Cracks are also

sometimes observed along $\sim\text{Al}_8\text{Mn}_5$ secondary particles (e.g. by the red arrow in Figure 22b), yet this feature is inconsistent (e.g. by the white arrow in the same image).

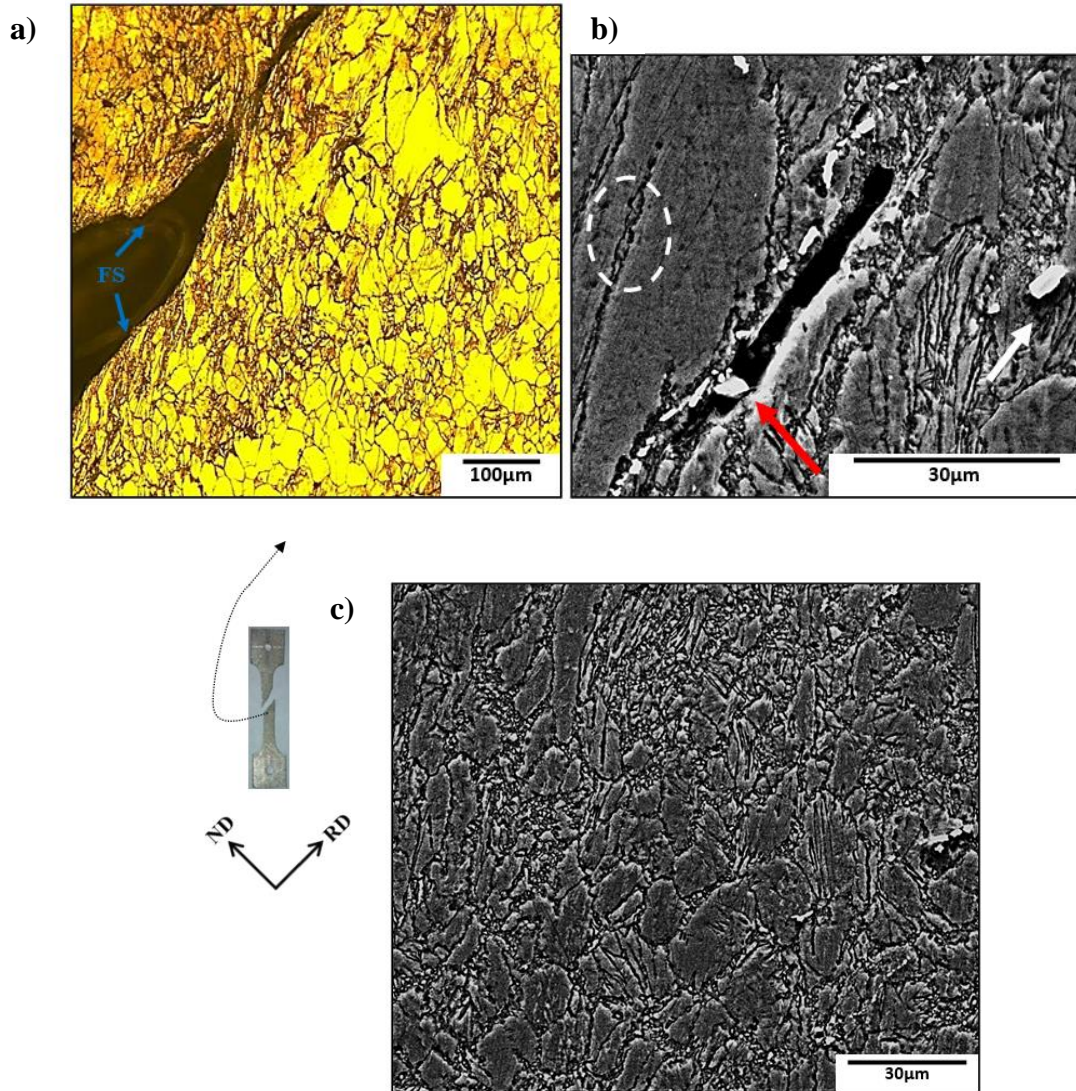


Figure 22. Metallography of 45toND at 150°C, with a macro-image of the tested sample. (a) shows a crack evident along DRX region, (b) shows a crack present near an $\sim\text{Al}_8\text{Mn}_5$ precipitate. (c) DRX grains appear to coalesce into shear bands. FS: Fracture Surface.

To elaborate on the effects of DRX and twins on failure, EBSD maps were constructed near a crack for 45toND at 150°C, as shown in Figure 23. Notice here that the basal planes remain mostly $\sim 45^\circ$ from the tensile axis after failure and do not largely

deviate from the As Received texture, which is marked via black dashed ellipses in the contour plot. Nevertheless, a fraction of basal planes have reoriented normal to the tensile axis due to tensile twinning, and these grains are colored red in the IPF map of Figure 23. It is also worth mentioning that refined, presumably DRX grains are present along the crack region, similar to observations in Figure 22.

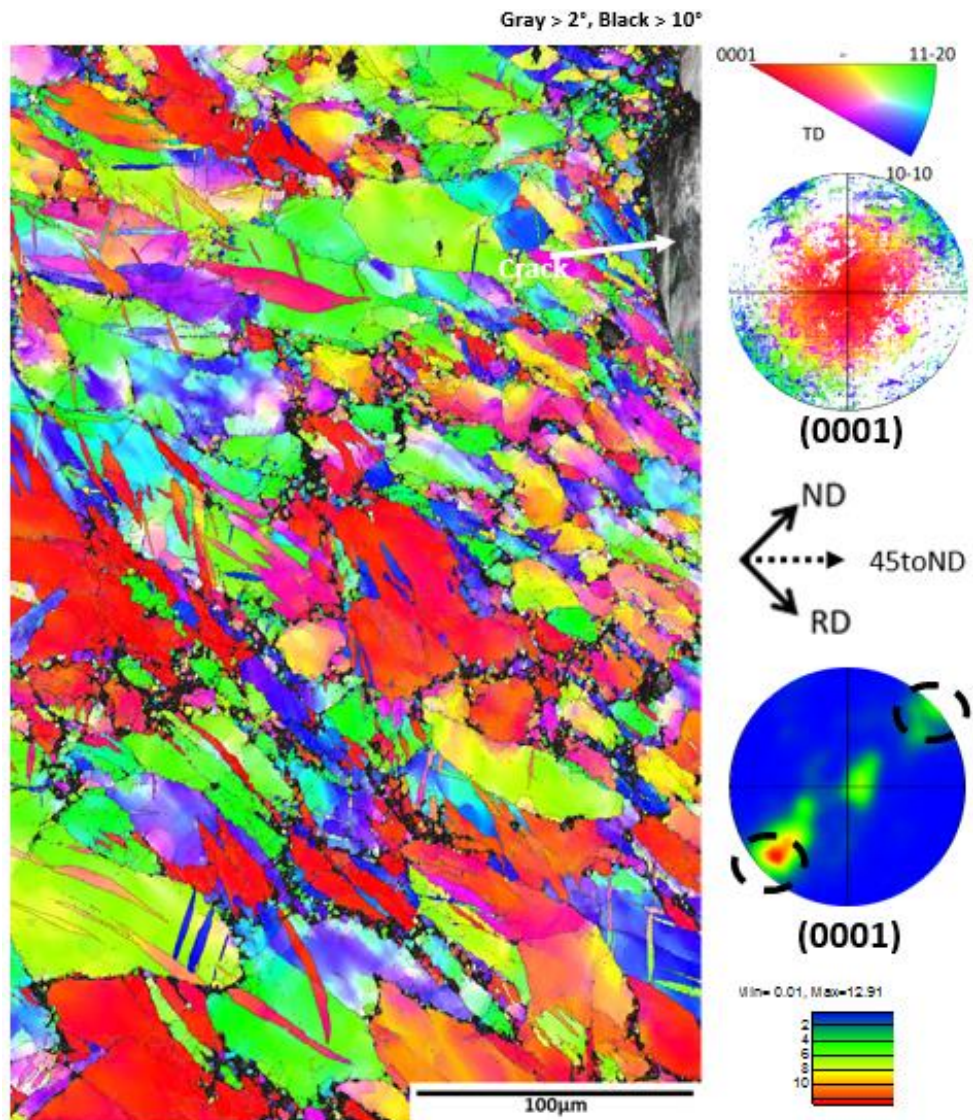


Figure 23. EBSD of 45toND at 150°C. The IPF map and corresponding basal plane contour texture plots are provided. Notice that the map was constructed near a crack (white arrow). See text for further details.

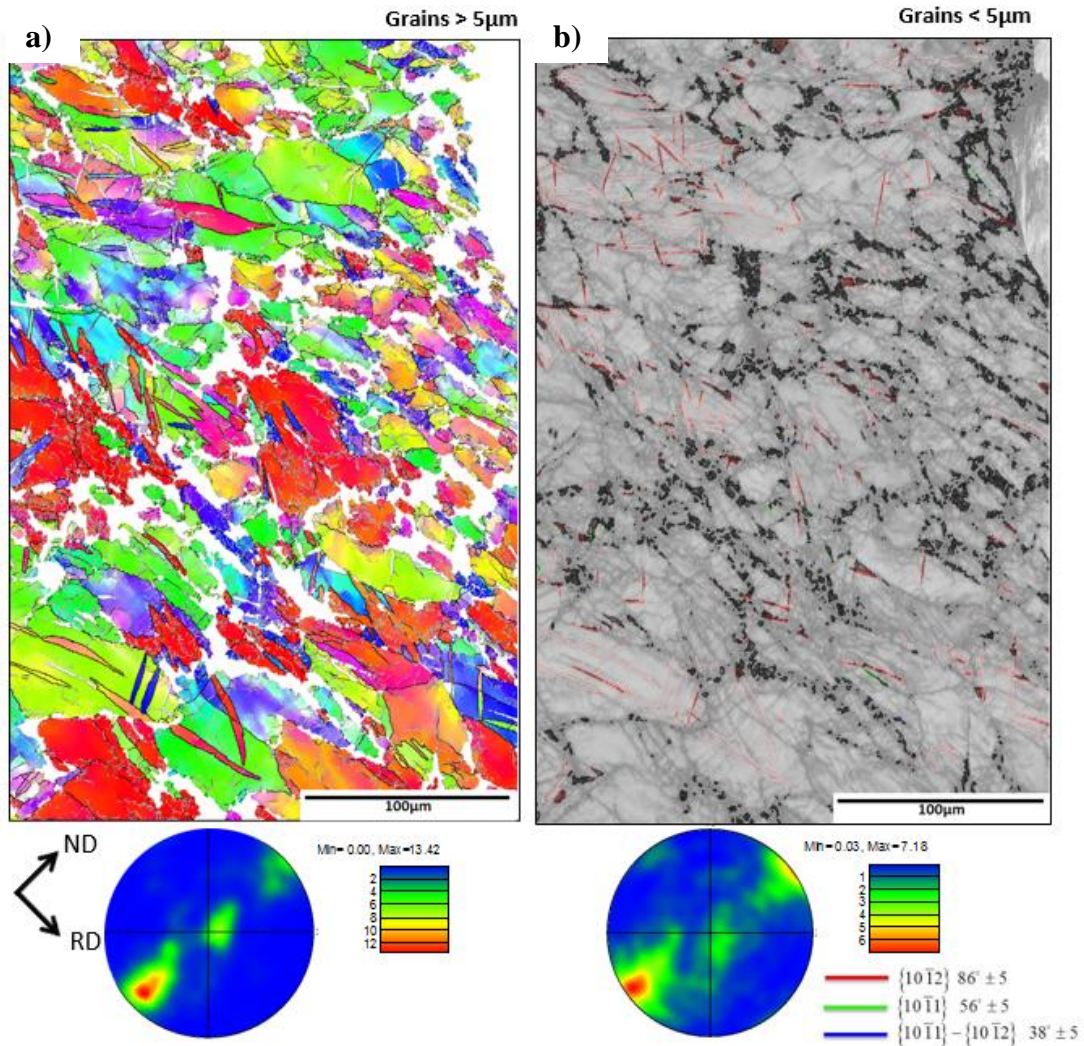


Figure 24. Comparison between textures of (a) large ($>5 \mu\text{m}$) and (b) small ($<5 \mu\text{m}$) grains. Twin boundaries are also visible in (b). EBSD maps corresponds to the same area as in Figure 23.

Separate maps for large ($>5 \mu\text{m}$, Figure 24a) and fine ($<5 \mu\text{m}$, Figure 24b) grains were constructed from the original EBSD map in Figure 23. Here, textures are similar for both cases. Additionally, Figure 24b includes indexed twin boundaries, where tensile twinning is shown to be predominantly active for 45toND at 150°C . Notice also that DRX grains are evident both within twins and along grain boundaries. Given the limited texture

evolution, basal slip remains favored throughout for the majority of the grains, which can be seen in the Schmid factor maps from Figure 25b. In Figure 25a, prismatic slip is favorable for the twinned grains. For Mg-AZ31, Galiyev *et al.* also observed DRX grains at 150°C which nucleated via dislocation pile up and non-basal slip following the initial deformation via basal slip and twinning [42]. The current results indicate that DRX grains form easy shear paths, and after a sufficient amount of DRX, cracks nucleate along these regions. Therefore, failure is initiated from DRX regions as reported by Ion *et al.* [41], and given the DRX grains within twins and decorating parent grains, both TDRX and CDRX are presumed active here resulting in minimal texture evolution.

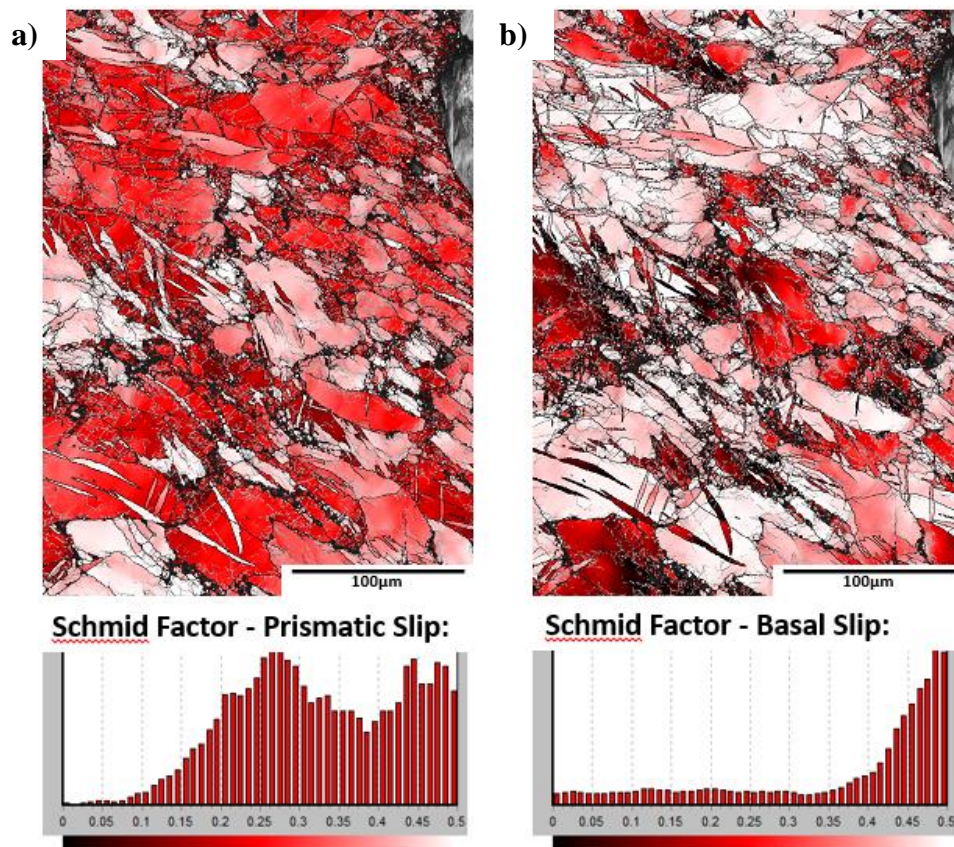


Figure 25. Schmid factor maps for (a) prismatic slip and (b) basal slip for 45toND at 150°C. EBSD map corresponds to the same area as in Figure 23.

2.2.4 Tensile Flow Responses and Microstructures at Failure at 200°C

At 200°C, the flow curves in Figure 11d generally show improved ductility over lower temperatures. Once again, TD shows the optimal mechanical properties (strength and elongation), followed by 45toND and ND, respectively. Strain hardening is not evident at 200°C, indicating a slip dominated deformation which is expected as this is the highest test temperature, with the most readily activated slip mechanisms. As shown in Figures 26-28, macroscopic necking was evident for 45toND and TD yet remained minimal for ND. Twins were not prominent for any of the orientations. Also, the contribution of DRX to strain becomes most significant at 200°C, as the most latent softening is evident here. In comparison to previous temperatures, 200°C indicates that enhanced ductility is strongly correlated with increased DRX activity.

Figure 26 captures the twin-free microstructure of the TD sample tested at 200°C. A macro-image of the sample is also shown with significant necking near the fracture surface, as expected from its high ductility (approaching 50% in Figure 11d). In Figure 26a, voids characteristic of ductile fracture are found near the fracture surface, as indicated by the red arrows, and these voids are bordered by necklace-type DRX grains. In general, significant amounts of DRX grains can be seen throughout the specimen; these occur along grain boundaries as necklace DRX (Figure 26a), near the $\sim\text{Al}_8\text{Mn}_5$ particles (not shown), and along the cracked regions (Figure 26b). It is also worth mentioning that a white, speckled pattern of fine secondary particles is captured in Figure 26b within the DRX regions. As discussed in a companion study by Dogan *et al.* [60], these secondary particles consist of Mg-Zn-Al and dynamically precipitated during the tensile test.

Additionally, said precipitates extract solid-solution hardening elements (i.e. Al, Zn) from the DRX regions, making the DRX grains “softer” than the surrounding matrix [60]. As such, DRX regions are more prone to crack formations, ultimately leading to failure [60]. Since TD at 200°C has the highest volume fraction of DRX grains, these dynamically precipitated particles are most readily observed for this condition. At lower temperatures, dynamic precipitation along DRX regions was much less obvious, perhaps due to slowed kinetics.

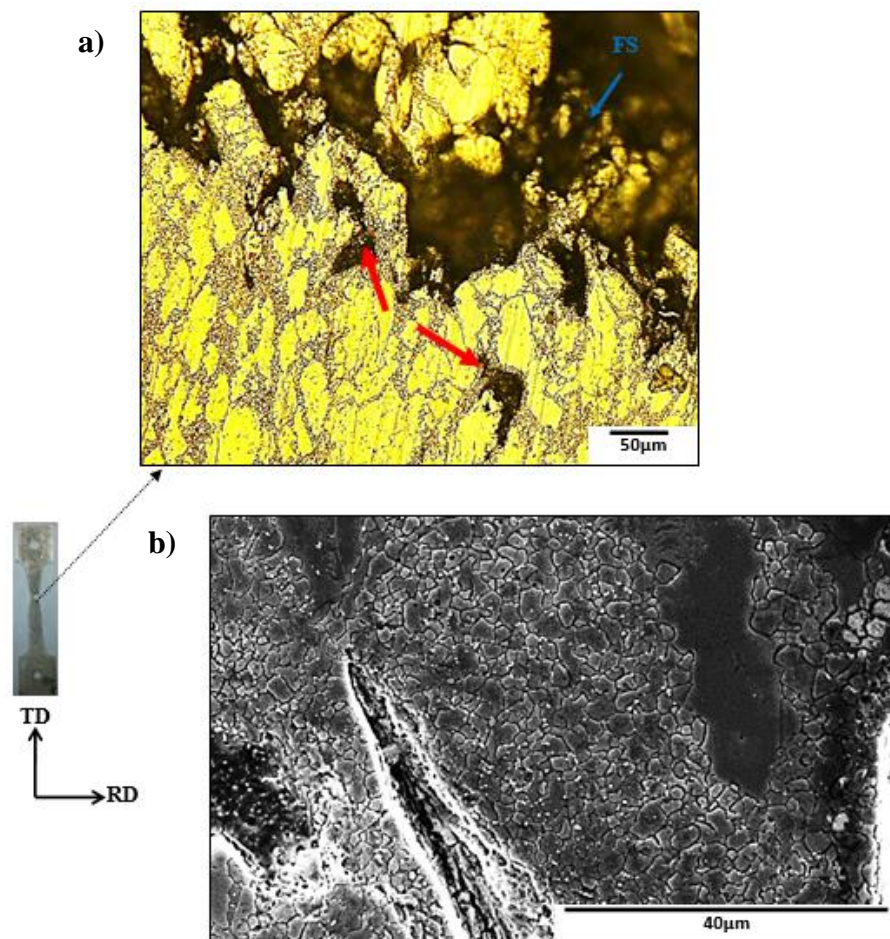


Figure 26. Metallography of TD at 200°C. (a) and (b) show void and crack initiation, respectively, along DRX regions. White dynamic precipitates are visible in (b) along DRX regions. FS: Fracture Surface.

In Figure 27, a macro-image of the slightly necked ND sample tested at 200°C is shown with its corresponding microstructure. In comparison to lower temperatures, two major differences for this orientation at 200°C are the larger volume fraction of DRX near the fracture surface (Figure 27a and c) and the minimal amount of twinning visible throughout the specimen. DRX grains are highly localized near the fracture surface and become much less prominent away from this region (Figure 27b), a unique feature in comparison to the other orientations at 200°C.

The limited amount of DRX for ND at 200°C is likely related to the active deformation mechanisms [43]. Galiyev *et al.* [42] proposed DRX at low temperatures formed via pyramidal $\langle c + a \rangle$ slip along grain boundaries, where due to stress concentrations CRSS for pyramidal slip can be most readily overcome. In contrast, Ion *et al.* [41] proposed that DRX form after twinning via basal slip, which causes rotations leading to CDRX. As few twins were observed for ND at 200°C (Figure 27) and basal slip is suppressed, it is more likely that DRX formed via pyramidal slip. Such an argument is supported by the concentration of DRX grains along the fracture edge, where stress levels apparently were maximal. Furthermore, stress-strain curves in Figure 11d show minimal strain hardening for ND at 200°C in comparison to 150°C, indicating the transition from soft tensile twinning to the harder pyramidal $\langle c + a \rangle$ slip. This indicates that stress concentrations here promoted DRX via pyramidal slip.

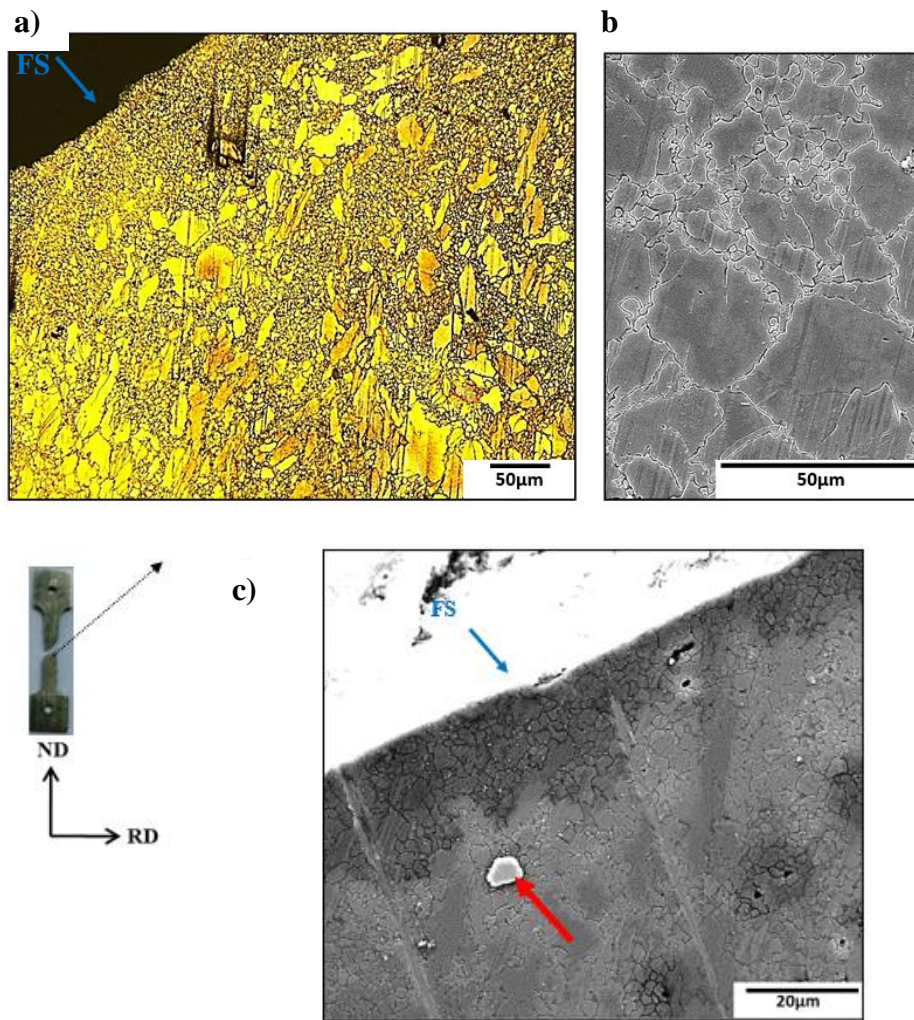


Figure 27. Metallography of ND at 200°C, with a macro-image of the tested specimen. (a, c) show failure along DRX regions concentrated near the fracture surface. (b) shows DRX are less prominent away from the fracture surface. (c) also shows an $\sim\text{Al}_8\text{Mn}_5$ particle (red arrow) near the fracture surface. FS: Fracture Surface.

As DRX occurs mainly along the fracture edge, crack initiation and propagation is concentrated in this area, causing a more abruptly fracture for ND. In contrast, for TD at 200°C, DRX grains were evident throughout the microstructure at 200°C and allowed for a more ductile fracture via micro-voids which gradually coalesced together (Figure 26). It is also worth mentioning that a speckled pattern of secondary Mg-Zn-Al particles can be

seen in Figure 27c along the fracture edge. As mentioned previously for TD at 200°C, these precipitates promote crack initiation and growth along DRX regions [60].

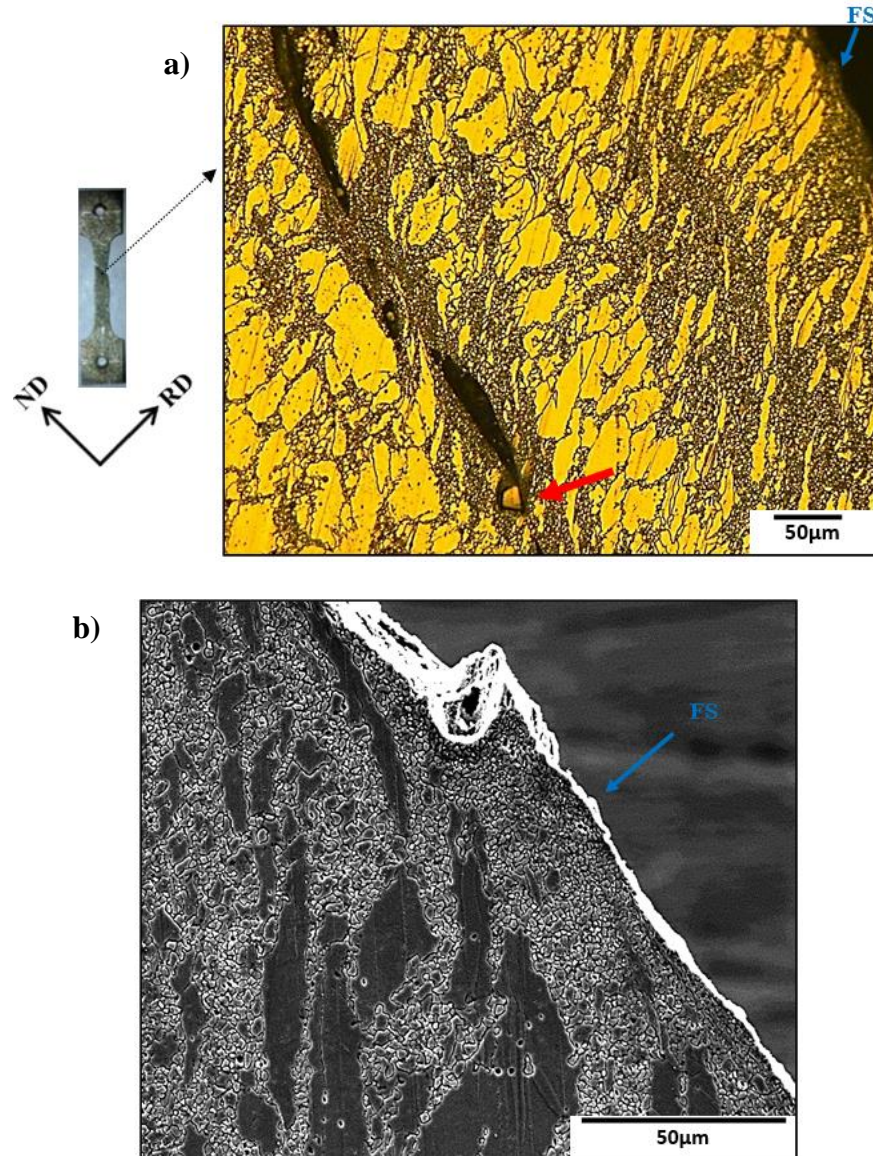


Figure 28. Metallography of 45toND at 200°C, with a macro-image of the tested specimen. (a) shows cracks initiate along the DRX regions, and also near an $\sim\text{Al}_8\text{Mn}_5$ secondary particle (red arrow). (b) shows DRX regions near the fracture surface. FS: Fracture Surface.

Finally, the 45toND sample tested at 200°C is shown in Figure 28, where twinning is suppressed and DRX grains are present throughout the specimen. Large cracks are seen along the DRX regions, and one is visible near the $\sim\text{Al}_8\text{Mn}_5$ particles (red arrow in Figure 28a). Significant necking (macro-image in Figure 28) was observed for this sample, as expected from its high ductility ($\sim 40\%$ in Figure 11d). In general, the failure type for the 45toND sample tested at 200°C, with high ductility and crack nucleation within the DRX regions, was also seen at 150°C for this orientation (Figure 22). Mechanisms for failure appear to be induced via soft DRX regions, which were discussed in this thesis as aligning with mechanisms proposed by Dogan *et al.* [60] and Ion *et al.*[41].

2.3 Summarizing Deformation Phenomena for Mg at Low Temperatures

In the previous section (Section 2.2), flow curves and microstructures at each specific temperature (25-200°C) were analyzed sequentially in detail, and the current section attempts to combine those findings into a coherent summary which can serve to clarify temperature effects on different deformation and fracture phenomena for AZ31. Such information should prove useful for designing processes which favor optimal formability at lower temperatures in magnesium alloys.

2.3.1 Effect of Temperature on Deformation Mechanisms

Figure 29 captures the effect of temperature on tensile loading along ND, TD, and 45toND for the hot-rolled AZ31 plate. As a refresher, when the basal planes are perpendicular to the tensile loading axis, the Schmid factor of basal slip is close to zero.

Therefore, prismatic slip is the most favorable deformation mode in TD samples. When basal planes are oriented 45° to the tensile loading axis (45toND), basal slip is most favorable since it has the lowest CRSS and highest Schmid factor. Finally, the Schmid factor for ND favors either tensile twinning or pyramidal $\langle c + a \rangle$ slip depending on temperature, and basal and prismatic slip is suppressed since the planes are normal or parallel, respectively, to the deformation axis.

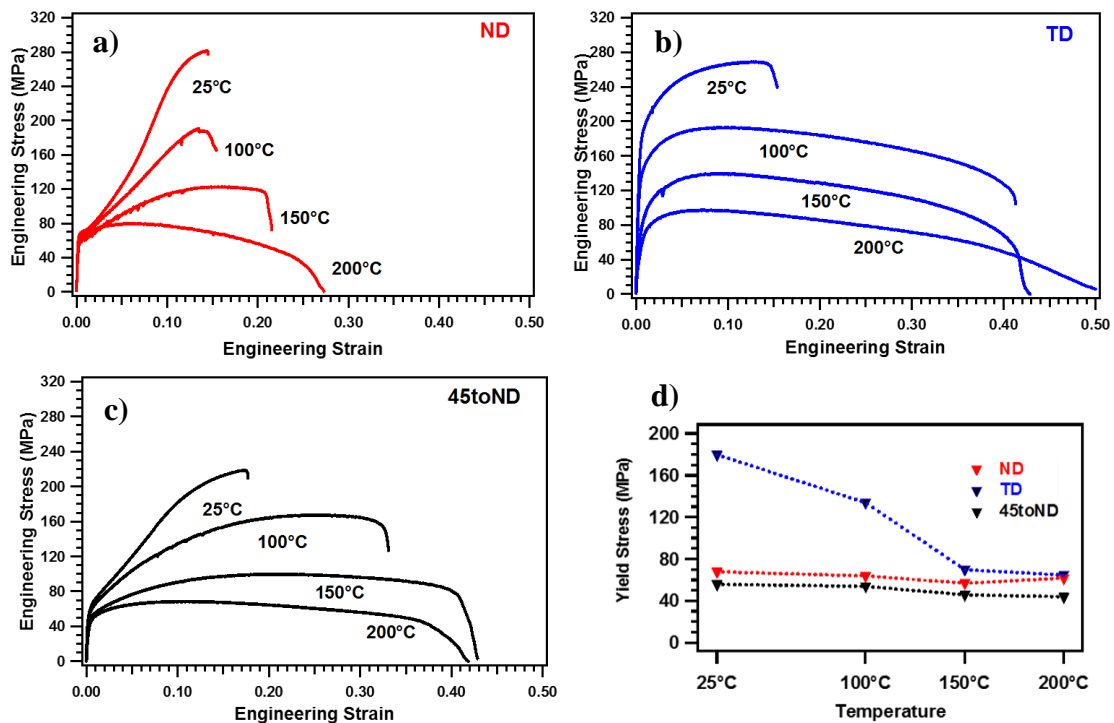


Figure 29. Engineering stress vs engineering strain tension responses of Mg-AZ31 tested at a temperature range of 25°C to 200°C. (a) ND (tensile twinning), (b) TD (prismatic slip), and (c) 45toND (basal slip). (d) Corresponding evolution of 0.2% yield stress with temperature.

Figure 29d captures the yield stress for all orientations as a function of temperature, where prismatic slip (TD) has the highest yield strengths and also shows the most significant temperature dependence. Notice here that the yield stresses reflect CRSS

values and thermal sensitivity for the individual deformation mechanisms, as prismatic slip has a higher CRSS at low temperatures than basal slip and tensile twinning. Tensile twinning and basal slip should be athermal in comparison to prismatic slip, and basal slip should demonstrate the lowest CRSS as it operates via the close-packed basal plane [22]. These phenomena are reflected in Figure 29d. Yield strengths converge at 150°C, indicating that formability should be greatly improved at this temperature due to the suppressed mechanical anisotropy. The strain to failure levels at 150°C for all orientations reflect a much improved ductility as well. In this regard, it was shown in Section 2.2.3 that a transition from twinning to slip dominant failure was observed when the temperature rose to 150°C.

Strain hardening, an indication of tensile twinning activity, is most prominent among ND cases (Figure 29a). In contrast, TD (Figure 29b) exhibits the least amount of strain hardening, perhaps due to its necessity for c-axis compression rather than extension. Strain hardening generally begins to mitigate at 150°C, and largely twin-free microstructures emerge for all orientations at 200°C. However, even at 200°C for ND, where pyramidal $\langle c + a \rangle$ is likely activated, there is a considerable difference in ductility levels for ND and TD. The comparatively lower strain to failure along ND at 200°C is somewhat surprising, as pyramidal $\langle c + a \rangle$ slip should accommodate 5 independent slip systems, sufficient for homogeneous ductility. In this regard, the role of DRX may be key, since more DRX are present for TD and 45toND than ND at 200°C. This will be elaborated upon in the next section.

2.3.2 Effect of Deformation Modes on DRX and Ductility

Metallography for ND, 45toND, and TD indicated that DRX grains were most prominent for TD, followed closely by 45toND and, finally, ND. Indeed, for all temperatures, ND exhibited the lowest volume fraction of DRX grains. Therefore, it appears that prismatic slip promotes DRX, which allow for high strains and more ductile fracture features at low temperatures. In contrast, pyramidal slip and tensile twinning inhibit DRX, promoting earlier failure. It has been reported previously that pyramidal $\langle c + a \rangle$ slip along grain boundaries promotes DRX nucleation there [42]. However, from ND at 200°C, perhaps the lower DRX activity is connected with the more homogeneous activity of pyramidal slip, resulting in fewer stress concentrations at grain boundaries. Rather, stress concentrations at the fracture edge may have promoted abundant DRX along mainly this region via pyramidal $\langle c + a \rangle$ slip.

For 45toND, it appears that basal slip also promotes DRX, to a similar degree as TD, and both samples demonstrate excellent ductility when DRX is readily active (Figure 29). With these observations in mind, one of the apparent keys to high strength and improved formability is via favoring prismatic slip activity. Although prismatic slip can supply just two independent deformation mechanisms, its high propensity for DRX allows for additional strain accommodation along these regions, resulting in enhanced low temperature ductility. Furthermore, designing for high prismatic slip activity also promotes optimal yield strength levels for low temperature applications (Figure 29d).

2.3.3 The Role of the Al-Mn Precipitates

The Al-Mn particles are mostly aligned along the rolling direction and are present in all tensile specimens. They are aligned perpendicular to the tensile loading axis in the TD and ND cases, at which the stress state promotes the crack initiation. However, the ductility levels of the TD and ND specimens are remarkably different at elevated temperatures, indicating that failure is not associated with the Al-Mn particles. At 150°C, the numerous voids near the fracture surface and the crack initiation around the particles are shown in Figure 17 and Figure 22. However, the ND at 100°C specimen failed at a shear band that is free of particles, although many voids are present near the fracture surface. The minimal volume fraction (<1%) for the Al-Mn precipitates indicates that they had a generally limited role on failure mechanisms.

2.3.4 Fracture Surfaces at 100°C and 200°C

Figure 30 captures SE images from the fracture surfaces of ND, TD, and 45toND tested at 100°C (top) and 200°C (bottom). At 100°C, a few dimples are evident for ND, although features reminiscent of cleavage fracture indicate a transgranular, brittle fracture mechanism. In 45toND at 100°C, dimples were obvious, where a large one perhaps resulting from failure along a twin interface or grain boundary can be seen at the fracture surface in Figure 30. The highest proportion of dimples were evident for TD among the 100°C samples, and features resemble microvoids which coalesced, indicative of a more ductile fracture mechanism. When the temperature increased to 200°C, ductile fracture prevailed, as dimples and voids were seen for all samples at the fracture surface (Figure

30 bottom). Sample necking was most pronounced in TD at 200°C, and 45toND and TD both exhibit gradual necking features correlated with more homogeneous DRX activity (see Figure 26 and Figure 28). In contrast, ND at 200°C shows a more abrupt neck region in Figure 30, perhaps due to the concentration of DRX grains near the fracture surface (Figure 27a).

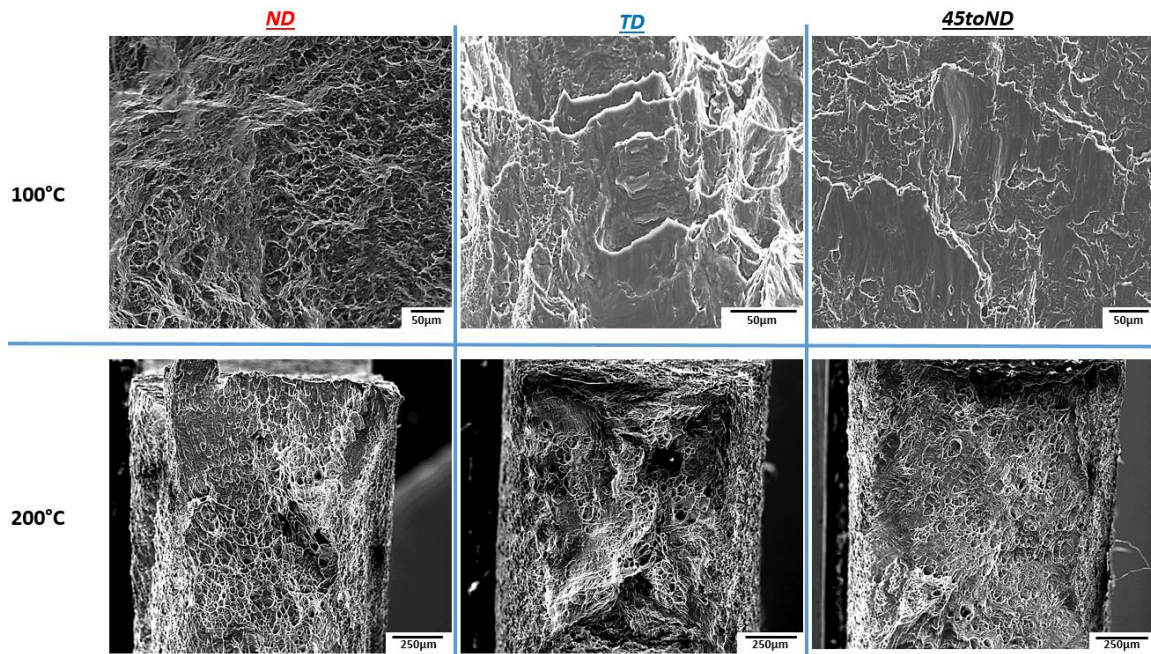


Figure 30. Fracture surfaces for all samples tested to failure at 100°C (top) and 200°C (bottom).

Figure 31 compares the macroscopic sample images for all 12 test conditions, where the fracture edge and sample necking can be observed. Here, several general, simplified observations can be made. First, prismatic slip (TD) exhibits the most pronounced sample necking, indicative of ductile fracture. Second, tensile twinning activity, which is observed readily for 45toND and ND below 200°C, appears to promote uniform elongation perhaps due to strain hardening. Interestingly, basal slip is correlated

with a 45° fracture edge; for ND and TD at 25°C, the suppression of basal slip is also correlated with a flat fracture edge.













Schmid Factors	25°C	100°C	150°C	200°C
<u>ND</u> Tensile Twinning Favored				
<u>45toND</u> Basal Slip Favored				
<u>TD</u> Prismatic Slip Favored				

Figure 31. A comparison of macroscopic images for samples tested to failure for all conditions.

2.3.5 Trends in Fracture Mechanisms at Various Temperatures

In this study, it was shown that DRX promote enhanced ductility whereas twinning generally has the opposite effect and promotes earlier fracture. Twinning volume fractions were highest for ND, followed by 45toND and, finally, TD. Note that readily activated prismatic slip in the TD case generally promotes DRX, suppresses twinning, and exhibits the highest strain to failure at all temperatures besides 25°C. In contrast, uniform

elongation to failure and no significant necking was observed in the 45toND and ND specimens up to 150°C, where both samples showed more pronounced tensile twinning activity than TD. Tensile twinning seems to cause non-uniform DRX due to deformation localization (i.e. TDRX) in the ND and 45toND cases, thereby deteriorating ductility at moderately elevated temperatures. In Section 2.2, the various cases were analyzed and proposed mechanisms of fracture were discussed. In Figure 32, these fracture mechanisms are summarized for the reader in an attempt to clarify the current findings in a simple and efficient manner.

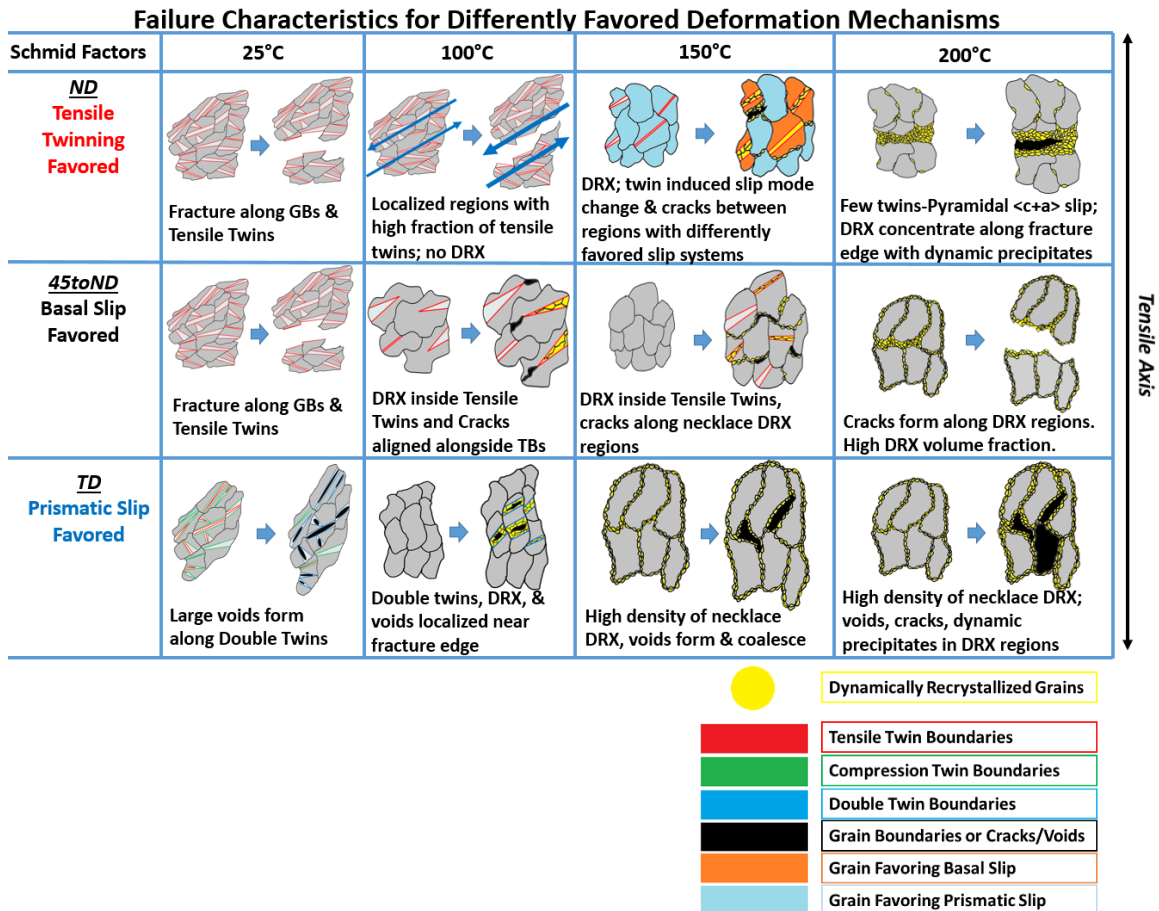


Figure 32. Observed failure phenomena summarized for all conditions. Please follow the legend to clarify the schematics. GBs: grain boundaries, TBs: twin boundaries.

2.4 Conclusions

In this chapter, tensile specimens were cut from a hot-rolled Mg-AZ31 alloy plate along different orientations that favored a variety of deformation mechanisms. Tested to failure at low temperatures (25-200°C), the microstructures of these samples were examined near the fracture surface. Distinct characteristics of failure were categorized according to the favored deformation mechanism and test temperatures, in the aim to ultimately expand the current understanding of low temperature formability for magnesium alloys.

Here, active deformation modes showed a significant effect on dynamic recrystallization (DRX) behavior and the strength and ductility levels for the AZ31 Mg alloy at low temperatures (at and below 200°C). In addition to Figure 32, several main findings of this study can be summarized as follows:

1. Slip mechanisms (basal, prismatic, and pyramidal $\langle c + a \rangle$) promote DRX, whereas tensile twinning retards DRX.
2. DRX activity correlates with more ductile fracture mechanisms and consequently improved ductility at low temperatures, although fracture was shown to occur preferentially along DRX regions.
3. When tensile twinning is activated, uniform elongation is more pronounced due to hardening associated with tensile twinning. Conversely, twinning caused shear localization and thus non-uniform DRX, thereby inducing earlier fractures at moderately elevated temperatures.

4. In the future, processing methods should allow for maximal prismatic slip activity, which was shown to promote optimal yield strengths and elongations to failure.
5. The effects of Al_8Mn_5 precipitates on failure for AZ31 were minimal; however, precipitates may contribute significantly to failure for alloys with higher precipitate volume fractions.

CHAPTER III

EFFECTS OF GRAIN SIZE REFINEMENT ON MECHANICAL PROPERTIES OF A PRECIPITATION HARDENABLE MAGNESIUM ALLOY

Chapter II investigated low temperature failure characteristics for AZ31, the most commonly wrought magnesium alloy, in an effort to ultimately provide recommendations for improved low temperature formability for magnesium. In contrast, the current chapter attempts to explore the upper limits of strengthening for a more recently developed, RE-free magnesium alloy. As a refresher, two well-known methods for enhancing the strength and controlling the anisotropy in magnesium alloys are precipitation hardening and grain size refinement. In the present chapter, both methods were combined in an attempt to obtain optimal strengthening. In this regard, a precipitation hardenable magnesium alloy was cast and severely plastically deformed via ECAP at low temperatures, ranging from 125-200°C. Specimens were processed along different ECAP routes, and the resulting mechanical responses, microstructures, and textures are discussed and compared.

3.1 Materials and Experimental Methods

The magnesium alloy Mg-ZKQX6000 (Mg 92.8 wt.%, Zn 6 wt.%, Zr 0.6 wt.%, Ag 0.4 wt.%, Ca 0.2 wt.%) was chosen for this study due to its favorability for precipitation hardening [52]. The alloy was initially manufactured by gravity die-casting, where the base material and alloying elements were obtained commercially. In producing the quinary alloy, the bulk alloying components were melted at 750°C in a steel crucible

and afterwards stirred for 30 min. Due to the strong reactivity of magnesium with air, melting and casting were conducted under a protective argon atmosphere. After casting, hot extrusion was conducted. Here, a direct extrusion operation was arranged in a 10 MN extruder with the extrusion die heated to 300°C along with the ZKQX6000 recipient, which was inserted into the extruder and pressed through the extrusion die with a profile velocity of 0.05 m·min⁻¹. This process, with an extrusion ratio of 16, produced a final square cross-section of 27.5 × 27.5 mm² for the extruded billet. After extrusion, the bulk material was segmented via wire EDM into billets ~150 mm in length. Next, the billets were homogenized at 350°C for 48 hours under argon before being water quenched, resulting in the As-Rec (short for ‘As Received’) condition which is mentioned throughout the text. Finally, billets were machined down to a 25 × 25 mm² cross section prior to ECAP.

As-Rec specimens were ECAP-deformed through a press with a sharp (90°) corner, and Figure 33 shows a schematic of the ECAP press relative to the processed material. In this study, three billets of ZKQX6000, called A3-1, A3-3, and A3-4 in the text, were processed along different ECAP routes and temperatures. Note that the results for specimen A3-2 are not reported here as it failed during the ECAP due to insufficient applied back pressure. Mechanical behavior for ECAP specimens is investigated and compared with the As-Rec condition to determine the level of mechanical enhancement resulting from texture and grain size modifications.

Table 2 includes details about ECAP routes and temperatures, and also compares the grain sizes between the As-Rec and ECAP conditions. Here, route A represents no

rotation of the billet along its Extruded Direction (ED_0) axis with respect to the ECAP press between passes (Figure 33). In contrast, route C represents a 180° rotation around ED_0 between passes. As an example, the route shown in Table 2 for A3-1 means that it was ECAP-deformed under two passes for route A at 200°C , rotated 180° along its ED_0 axis before going to 150°C for two more passes of route A. Finally, one pass of route C was conducted at 125°C . Three hundred grain diameters were individually measured via the ImageJ software package from multiple images, and the averages with standard deviations are reported in Table 2.

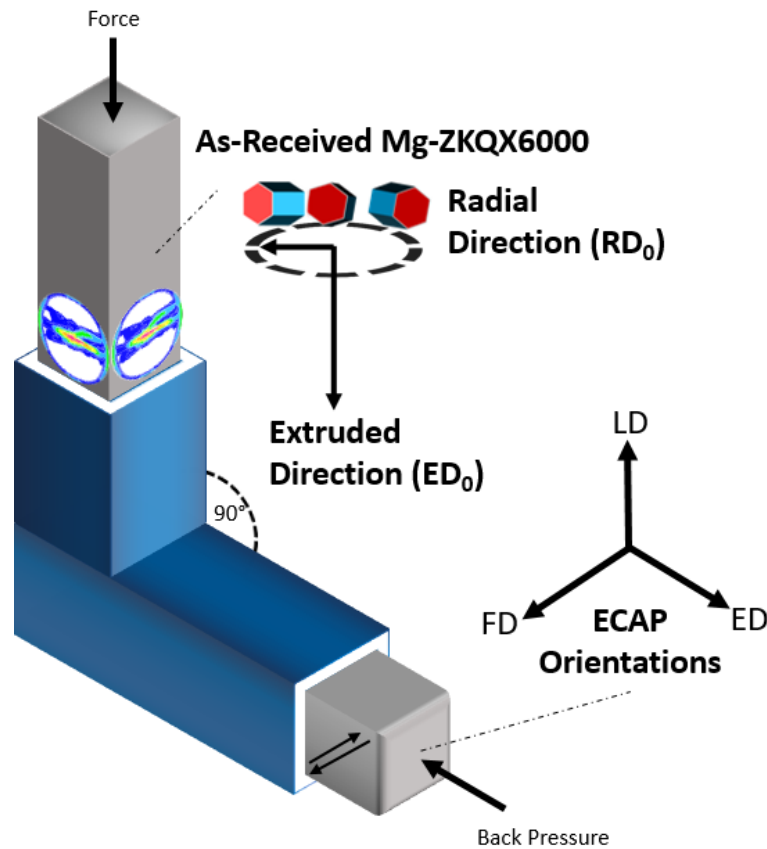


Figure 33. Schematic of the ZKQX6000 billets with respect to the ECAP press utilized in this study. Prior ECAP, pole figures show the (0002) basal planes are parallel to the Extruded Direction (ED_0). Post ECAP orientations - FD: Flow Direction, ED: Extrusion Direction, LD: Longitudinal Direction.

Table 2. ECAP processing details and resultant grain sizes for the ZKQX billets discussed in this study. Rotations were done about ED₀.

Designation	Processing Route and Temperature	Average Grain Size (μm)
As-Rec	None - As Received	10.6 ± 7.2
A3-1	2A@200°C + 180° rotation + 2A@150°C + 1C@125°C	0.54 ± 0.39
A3-3	4C@200°C + 180° rotation + 2A@150°C + 1A@125°C	0.51 ± 0.25
A3-4	4C@200 °C + 180° rotation + 2A@150 °C	0.92 ± 0.39

Further details on ECAP routes with the current press can be found in Ref. [59]; note that the routes chosen in this study are hybrid routes. For all ECAP experiments, extrusion rates of $4.5 \text{ mm} \cdot \text{min}^{-1}$ were utilized at 200°C and 150°C, while at 125°C the rate was reduced to $2.25 \text{ mm} \cdot \text{min}^{-1}$ as a precaution. Also, back pressures of 20, 35, and 55 MPa were utilized for 200°C, 150°C, and 125°C, respectively. Billets were heated for 30 minutes to temperature prior to each ECAP pass to homogenize the temperature throughout the sample.

Sample microstructures were examined via a Keyence VH-Z100 digital microscope and an FEI Quanta-600 SEM instrument. Pole figures of the bulk samples were determined using a Bruker-AXS D8 X-ray diffractometer with Cu Ka (wavelength $k = 0.15406 \text{ nm}$) radiation. Samples for microstructural characterization were cut from the mid-section of the deformed specimens from the flow plane. These samples were mechanically ground and subsequently polished with diamond paste to $0.1 \mu\text{m}$. OM and

SEM samples were etched via an acetic-picric acid mixture (20 mL acetic acid, 3 g picric acid, 20 mL H₂O, 50 mL ethanol (95%)). Chemical analyses of the alloy precipitates prior ECAP (As-Received conditions) was performed in a Cameca SX50 SEM equipped with four wavelength dispersive X-Ray spectrometers (WDS).

Flat, “dog-bone” tension specimens were cut via EDM along the ED₀ and radial direction (RD₀) for the As-Rec specimen, and along the flow and extrusion directions (FD and ED) for the ECAP specimens (Figure 33). The gauge sections of the tensile specimens were 8 × 3 × 1.5 mm³. Compression samples of dimensions 4 × 4 × 8 mm³ were cut along each direction. Samples were cut with the gage sections located in the midsections of the ECAP billets to capture the mechanical performance along the fully worked regions [59]. Tension and compression tests were performed using a strain rate of 5×10⁻⁴ s⁻¹ for all temperatures, using an MTS test frame with an MTS extensometer to record strain values.

3.2 Experimental Results

The extruded and As-Rec microstructures and crystallographic textures are shown in Figure 34. From the (0002) pole figure in Figure 34a, the extruded microstructure demonstrates a typical extrusion texture (recall Figure 2b), where basal planes are parallel to ED₀. Long strands, i.e. ‘stringers,’ of second phases aligned along ED₀ are also visible, and fine second particles can also be seen dispersed along grain boundaries (Figure 34a). As mentioned in Section 3.1, the alloy was heat treated at 350°C for 48 hours, dissolving the fine second phases into the matrix; the resultant condition is called the As-Rec state (Table 2 and Figure 34b), since it is the condition for all ZKQX6000 billets prior to ECAP.

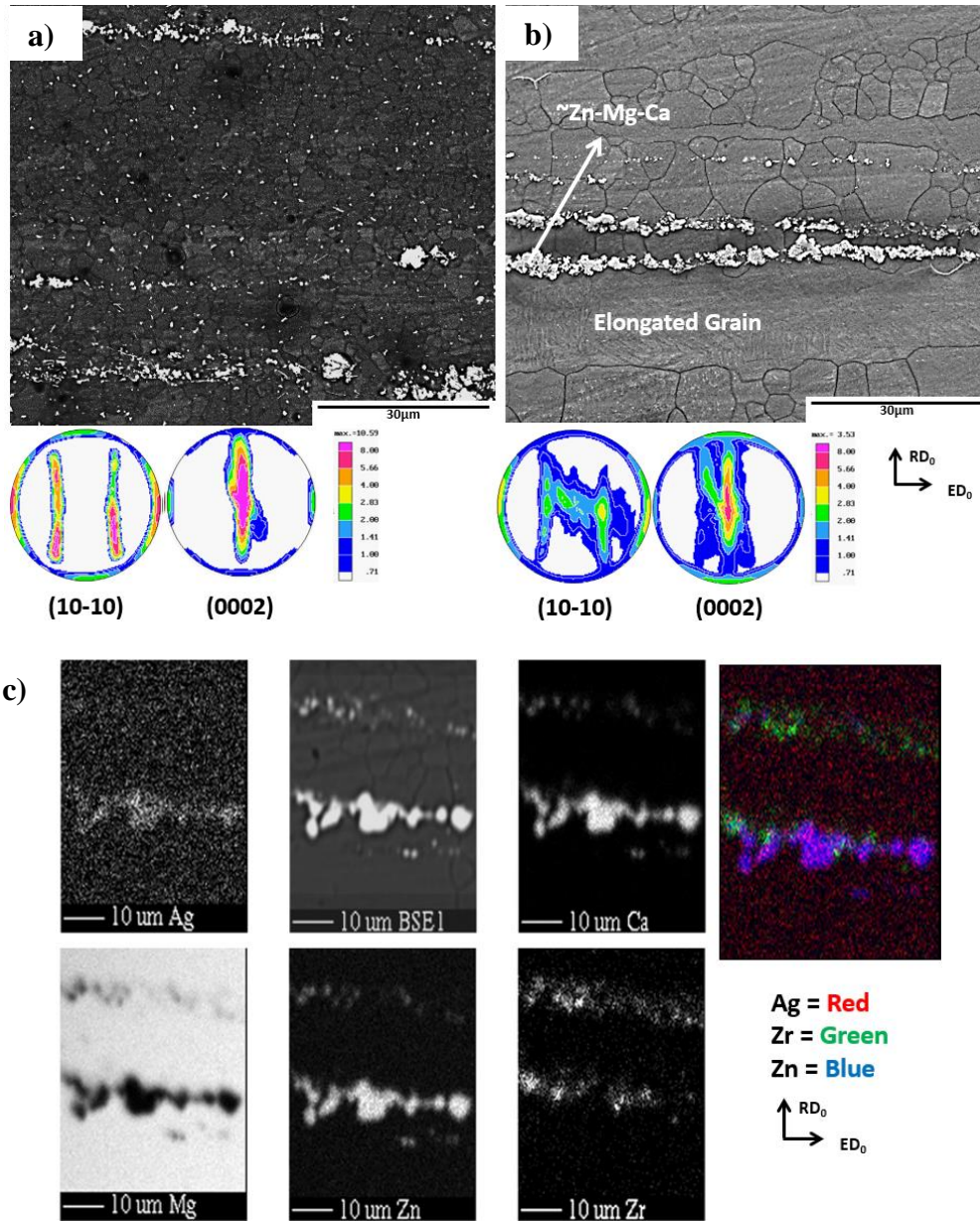


Figure 34. (a) Extruded and (b) pre-ECAP As-Rec microstructures for ZKQX6000. Corresponding prismatic (10 $\bar{1}0$) and basal (0002) pole figures are shown as well. For the As-Rec condition, (c) shows WDS elemental maps for precipitates and the matrix, where precipitates were found to be Zn and Ca rich, with trace amounts of Zr and Ag.

As seen from the As-Rec (0002) pole figure in Figure 34b, the homogenization heat treatment softened the extrusion texture, although generally the basal planes remain

parallel to ED_0 . Notice also in Figure 34b that the grains have grown significantly, and the refined secondary particles have diffused into the magnesium matrix. However, the long stringers of second particles were not solutionized via the homogenization heat treatment and remain elongated along ED_0 ; these particles (white arrow in Figure 34b) were point-analyzed via WDS as \sim Zn-Mg-Ca rich. However, the WDS elemental maps in Figure 34c indicate limited Mg, Ag, and Zr content for these phases. The average grain size for the As-Rec condition was $10.6\ \mu\text{m}$ (Table 2), although it is worth mentioning that elongated grains (Figure 34b) were also present along ED_0 and were excluded from the grain size measurements.

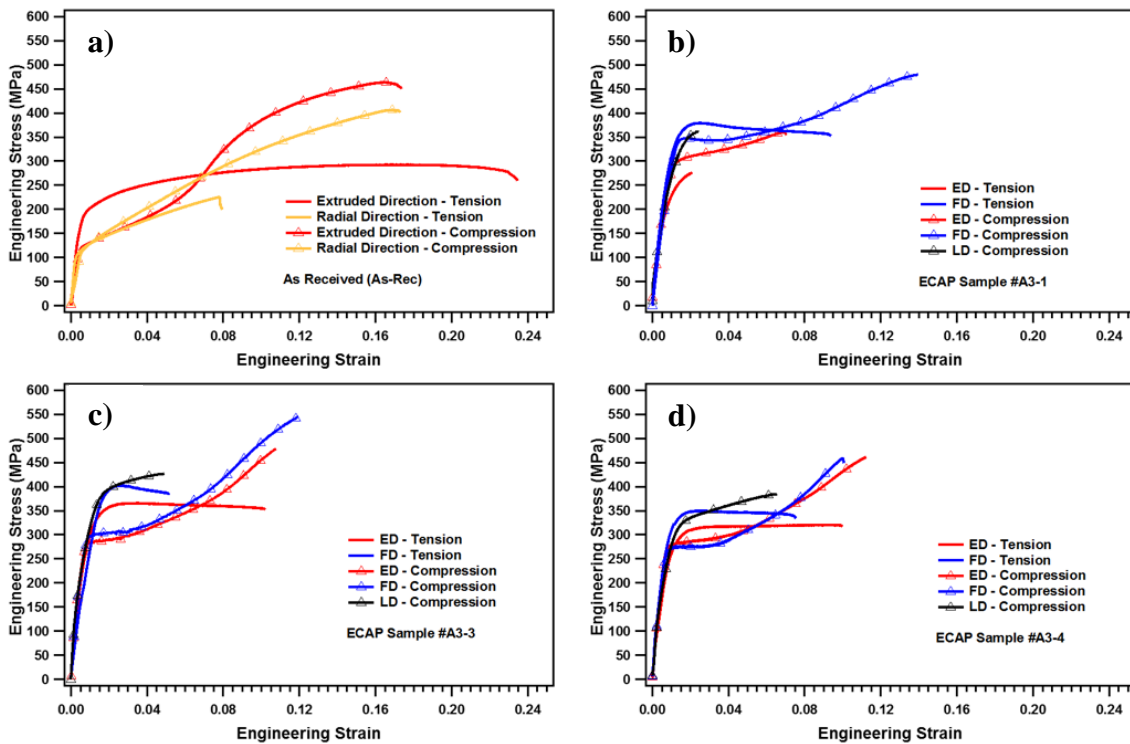


Figure 35. Engineering stress vs. strain test curves for ZKQX6000. (a) pre-ECAP condition, called As-Rec. ECAP conditions: (b) A3-1, (c) A3-3, and (d) A3-4. Please refer to Table 2 for ECAP routes for each billet.

Nominal mechanical responses for the As-Rec and ECAP-deformed specimens are included in Figure 35. Note several ultra-high tensile strength levels in the A3-1 and A3-3 specimens along the FD, which approach 400 MPa. Representative microstructures and crystallographic textures for the A3-1, A3-3, and A3-4 billets post-ECAP are also included in Figure 36. The corresponding grain sizes for the ECAP billets are shown in Table 2, where an ultrafine ($<1 \mu\text{m}$) grain size was obtained for all three cases. Notice in Figure 36 the prevalence of white precipitates along the fine grain regions, obscuring grain boundaries.

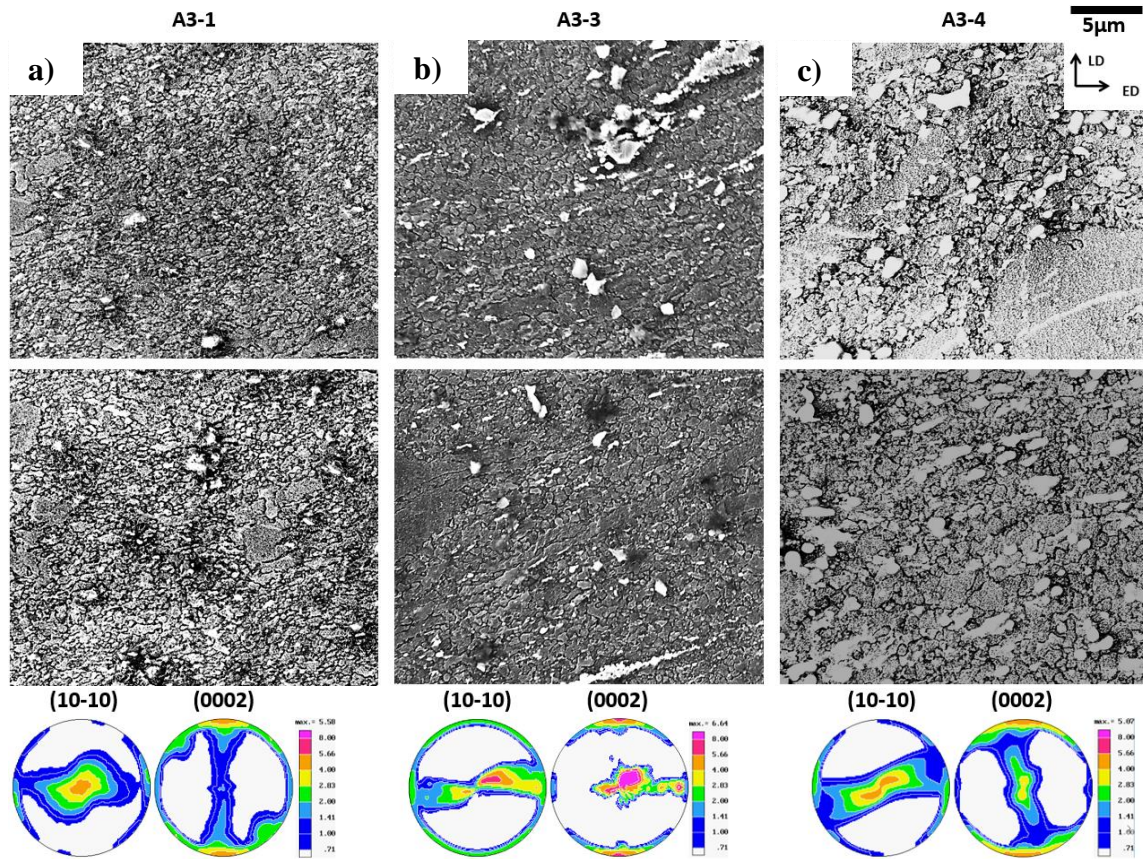


Figure 36. Metallography via SE for the following ECAP ZKQX6000 conditions: (a) A3-1, (b) A3-3, (c) A3-4. Precipitates cover fine grain regions. Pole figures are also included for (a-c), capturing the orientations of the prismatic $(10\bar{1}0)$ and basal (0002) planes.

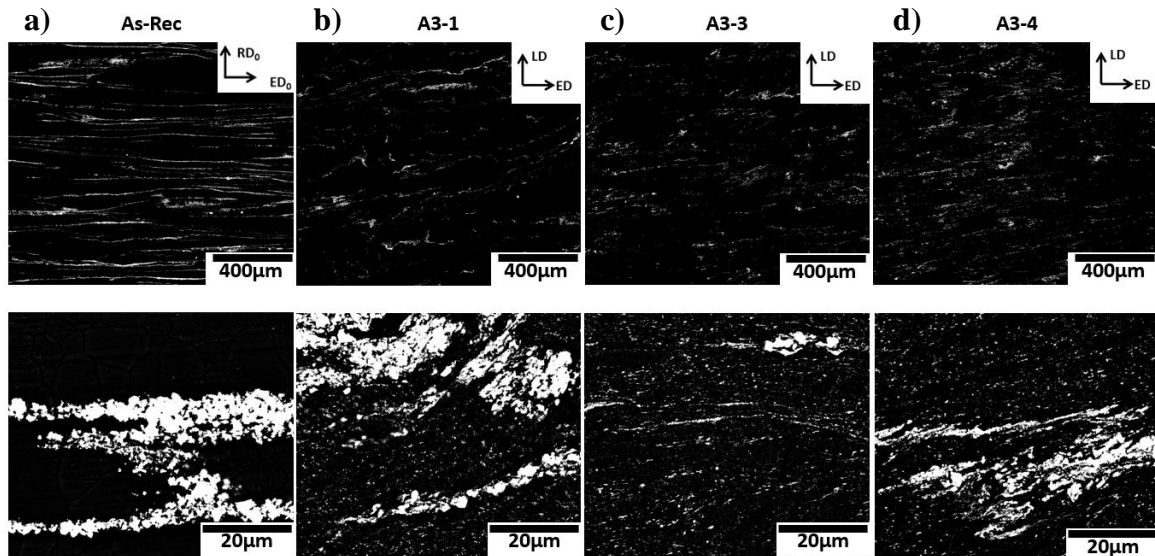


Figure 37. Precipitate morphologies captured via BSE for a larger area (top images) and a smaller area (bottom images). (a) As-Rec (b) A3-1 (c) A3-3 (d) A3-4.

In order to better characterize these precipitates and understand their effects on mechanical properties, back scattered electron (BSE) images are shown in Figure 37 for the As-Rec and ECAP conditions. Precipitates are white in these binary BSE images. In all of the top images here, a larger area has been taken in comparison to the bottom images. In the larger areas (top images of Figure 37), orientations of the precipitate stringers can be seen more clearly, and these orientations vary considerably. For example, in the As-Rec condition (Figure 37a, top image) precipitates are aligned along ED_0 , while in the ECAP specimens the precipitate stringers have realigned differently, as seemingly a function of ECAP route. Notice also that in the smaller areas (bottom images of Figure 37), a higher volume fraction of refined precipitates are clearly evident for the ECAP cases in comparison to the As-Rec condition. Although not shown here, Energy Dispersive X-

Ray Spectroscopy (EDS) characterized large precipitates after ECAP as generally Zn rich (similar to the As-Rec case). Nevertheless, note that considerable variations in precipitate chemistry were observed, and chemistries of refined precipitates were not measured due to EDS precision limitations.

3.3 Discussion of Results

In this chapter, ECAP was conducted on a precipitation hardenable ZKQX6000 magnesium alloy, successfully refining the grain size to ultrafine levels (Table 2). Consequently, ultra-high strength levels were achieved as seen in Figure 35 for a few cases. However, the effects of precipitates appears to be magnified after ECAP, as higher volume fractions of precipitates are evident in the ECAP microstructures in Figure 37. In this section, the effects of grain size, texture, and precipitates in relation to mechanical properties are discussed and compared for the different conditions.

3.3.1 Influence of Grain Size on Mechanical Properties

Mechanical responses in Figure 35 show increased yield strengths for all ECAP conditions in comparison to the As-Rec cases. Here, UTS for the As-Rec condition was ~300 MPa along ED_0 where the grain size was ~10.6 μm . In contrast, several of the best mechanical responses are seen for tension along FD for A3-1 and A3-3, with UTS levels approaching ultra-high strength (~400 MPa) via an ultrafine grain size (~500 nm). In addition, A3-4 exhibited a comparatively larger grain size (~920 nm) with a respectable UTS (~350 MPa). Given the grain refinement via ECAP, strength increments here are

attributed to Hall-Petch effects (recall equation 1). Notice also the role of processing temperature on grain refinement; lower final processing temperatures yielded finer grain sizes (Table 1), as expected from the multi-temperature step-down method [12, 51].

In Figure 35, only a few cases – A3-1 along FD and A3-4 along ED – showed reduction in tension-compression yield asymmetry after ECAP. Interestingly, while grain refinement to ultra-fine levels should suppress tensile twinning [36, 50] and, therefore, tension-compression yield asymmetry, there appears to be only limited improvement despite the ultra-fine grain size for ECAP conditions. The role of texture may be important in this regard, and will be discussed in Section 3.3.2. Finally, it is necessary to mention that elongation to failure was quite limited after ECAP. Here, among A3-1, A3-3, and A3-4, maximal tensile strain to failure levels reached only ~10%; incredibly low strain levels were also apparent for A3-1 compression along LD and tension along ED. Even for the As-Rec case, strain levels for tension along RD_0 are limited (~8%). Note that mechanical tests were repeated at least twice per orientation with general repeatability, yet low strain to failure levels were commonly observed for ECAP conditions.

3.3.2 Crystallographic Texture Effects on Mechanical Properties

The role of texture on mechanical properties is important since deformation mechanisms in magnesium are strongly dependent upon the starting texture [71]. As seen previously for AZ31 in Chapter II, deformation mechanisms in polycrystalline magnesium alloys are also highly temperature dependent. For ZKQX6000, note that all tests in Figure 35 were conducted at room temperature (25°C). As such, athermal deformation

mechanisms (i.e. tensile twinning and basal slip) should be primarily active for all conditions [26]. However, other deformation mechanisms may be active if their Schmid factors (equation 2) are high enough.

In Figure 34b, it can be seen that the As-Rec condition exhibits a general extrusion texture with the basal planes parallel to ED_0 . By equation 2, prismatic slip is therefore highly favored along ED_0 under tension, where c-axis compression may also prompt compression twinning or pyramidal $\langle c + a \rangle$ slip to a lesser degree. In contrast, for RD_0 under tension, tensile twinning and basal slip should be primarily active given the c-axis extension, Schmid factor, and low temperature. Compression along RD_0 or ED_0 should favor tensile twinning.

After ECAP, the three specimens demonstrate unique textures, which could explain some of their profound differences in mechanical responses. Under tension along FD, A3-1, A3-3, and A3-4 favor prismatic slip, tensile twinning, and prismatic slip, respectively. Likewise, under tension along ED, these samples all favor prismatic slip. In contrast, for compression along LD, A3-1, A3-3, and A3-4 are prone to compression twinning, tensile/compression twinning, and compression twinning, respectively. Tension twinning should be dominant for compression along ED and FD for these three cases, with one exception being compression twinning is most favored for A3-3 along FD.

The generally favored deformation mechanisms are summarized in Figure 38 for all conditions given texture and Schmid factor considerations. Note here that the activity of twinning modes for ECAP conditions may be inhibited, given the ultra-fine grain size [36]. In general, several findings in Figure 38 can be utilized for clarification of

mechanical flow responses of Figure 35. Here, note that prismatic slip, as a hard deformation mechanism, should promote higher strength and ductility at room temperature, as was seen in Chapter II for AZ31. In addition, prismatic slip should be more active for ultra-fine grained conditions [12]. From Figure 35, prismatic slip is correlated with improved ductility and high strength for most cases, except for the curious case of A3-1 tension along ED. Twinning is favored for all compression tests, where compression twinning correlates with higher stress levels than tensile twinning (see A3-1 and A3-4), reflecting a higher CRSS for compression twinning at room temperature [26]. Finally, twinning is correlated with lower strain levels in general, as seen for tension along RD_0 vs. ED_0 , and for A3-3 along FD vs. ED.

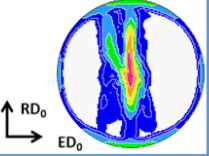
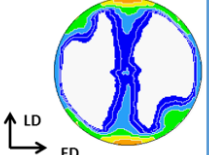
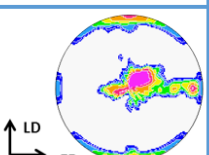
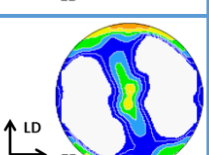
Sample	Basal (0002) Planes	Compression	Tension
As-Rec		RD_0 – T-Twin ED_0 – T-Twin	RD_0 – T-Twin, Basal Slip ED_0 – Prismatic Slip
A3-1		LD – C-Twin ED – T-Twin FD – T-Twin	ED – Prismatic Slip FD – Prismatic Slip
A3-3		LD – T-Twin, C-Twin ED – T-Twin FD – C-Twin, T-Twin	ED – Prismatic Slip FD – T-Twin
A3-4		LD – C-Twin ED – T-Twin FD – T-Twin	ED – Prismatic Slip FD – Prismatic Slip

Figure 38. A simplified summary of probable active deformation mechanisms via Schmid factors considerations for all tension and compression tests for As-Rec and ECAP conditions. T-Twin: Tension Twin, C-Twin: Compression Twin.

A general understanding of the deformation mechanisms active here would ideally be confirmed via microstructural analyses (preferably EBSD) of the samples tested to failure, to verify twin types, Schmid factors, and fracture mechanisms. Unfortunately, given the ultra-fine grain size and the presence of precipitates, such an analyses is not included here for ECAP samples. In general, the low ductility observed here after ECAP may not be a result of twinning, given the ultra-fine grain size and the limited strain hardening seen for the tensile specimens. In other studies of ECAP for AZ31, which is not precipitation hardenable, grain refinement led to high ductility as well as strength levels [12, 50]. As such, the mechanisms behind low ductility for the ZKQX6000 alloy are likely a result of precipitation effects, which is discussed next in Section 3.3.3.

3.3.3 Precipitation Effects on Mechanical Properties

From Figure 35a, RD_0 shows a much lower ductility than ED_0 , perhaps due to Schmid factor considerations (Figure 38). As ECAP conditions exhibit limited ductility as well, similar mechanisms of failure were perhaps involved for As-Rec and ECAP cases. With this in mind, microstructures at failure for As-Rec cases (tension along ED_0 and RD_0) are shown in Figure 39. Here, twins are evident along the fracture surface; however, twinning's influence on fracture was overshadowed, as it was found that failure occurred along the interfaces between the secondary Zn-Mg-Ca particles and grains during the RD_0 tensile test (Figure 39a). As a refresher, second phases and grains are elongated along ED_0 (Figure 34b-c). In contrast to RD_0 , during the ED_0 tensile tests, precipitate stringers act as crack barriers (see crack annotated in white in Figure 39b), reinforcing the surrounding

Mg matrix. As compression tests along RD_0 and ED_0 show similar strain to failure levels (Figure 35a), tension-induced delamination along precipitate-grain interfaces for RD_0 appears to cause premature fracture. It is worth mentioning that RD_0 loading is not generally reported for extruded, precipitation hardened magnesium alloys [52, 53].

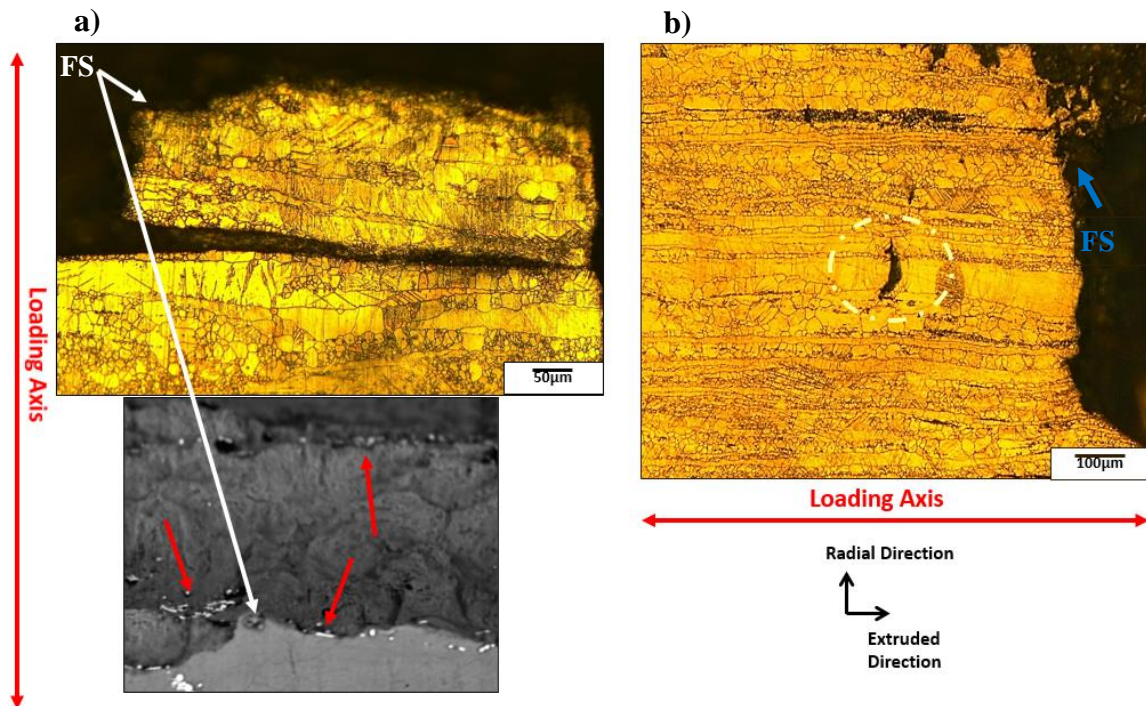


Figure 39. Microstructures at failure for As-Rec under tension along (a) RD_0 and (b) ED_0 . Particles indicated by red arrows in (a); crack seen via white ellipse in (b). FS: Fracture Surface.

The role of the precipitate-grain interface on failure is mentioned since it may impact the mechanical behavior of the ECAP specimens as well. ECAP of the As-Rec condition modifies precipitate morphology, grain size, and texture. Figure 37 captures a comparison of the Zn-Mg-Ca precipitate stringer morphologies, where precipitates are elongated along the ED initially (Figure 37a). After ECAP, various reorientations take

place as a function of the ECAP route (Figure 37b-d). Given the microstructure at failure for the As-Rec case (Figure 39), it is likely that embrittlement along precipitate stringer interfaces detrimentally affects ductility levels after ECAP.

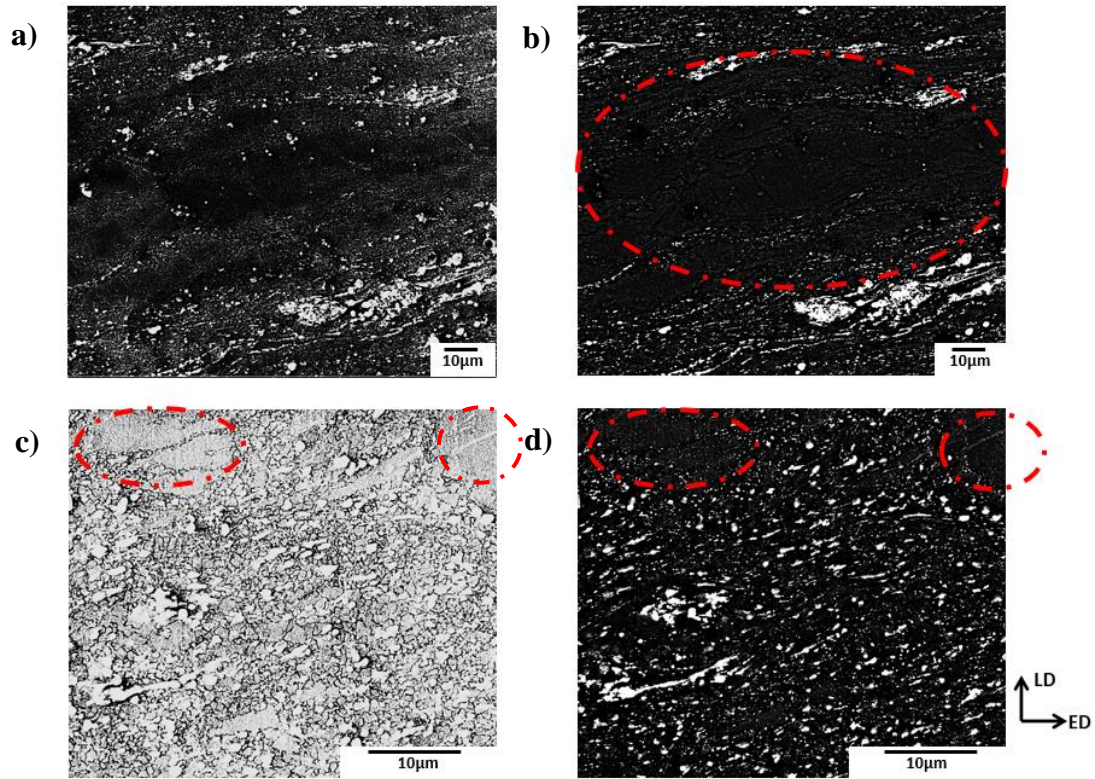


Figure 40. Evidence for dynamic precipitation after ECAP. (a) SE and (b) BSE of A3-3 from the same area; (c) SE and (d) BSE of A3-4 from the same area.

In addition to the precipitate stringers, Figure 40 BSE images show ultrafine Mg-Zn rich precipitates dispersed along the ultrafine grain regions; in general these particles were observed throughout the ECAP specimens along DRX regions. These precipitates are not observed prior ECAP, as seen by comparing Figure 37a with Figure 37b-d. In addition, notice that these precipitates were not observed in a few larger, non-deformed

grains of the ECAP samples (e.g. in red in Figure 40b-d). Hence, they are considered precipitates which nucleated dynamically during the ECAP.

Dynamic precipitation in Mg-ZK alloys is rarely mentioned in the literature. Dogan *et al.* [60] recently showed that ECAP of AZ31, which like ZK60 is not considered a precipitation hardenable alloy [52], demonstrates dynamic precipitation also along the DRX regions at 150°C. In contrast, Mostaed *et al.* argued that ECAP of ZK60 at 150°C refined the initial precipitate distribution, but they did not mention dynamic precipitation as a possible explanation [72]. In the present study, Figure 37 and Figure 40 indicate that both stringer precipitate reorientation and dynamic precipitation are occurring in the ZKQX6000 alloy during ECAP. The precise effects of these precipitates on failure are reserved for future studies.

Given the findings for the As-Rec case (Figure 39), poor ductility after ECAP could be derived from delamination at the interfaces between the reoriented precipitate stringers and the matrix. However, a detailed analysis of the fracture surface is needed to prove this argument. The contributions of the dynamically precipitated Mg-Zn rich second phases on strength requires further investigation. It is possible that the second phases contribute to grain boundary pinning, resulting in enhanced strength and brittle failure. Conversely, embrittlement along grain boundaries due to particle nucleation would explain the low strain to failure. An elaboration on the interaction effects between precipitates, grain size, and texture would be beneficial for expanding on the statements made here.

3.4 Conclusions

In this study, a Mg-ZK60 precipitation hardenable alloy containing trace additions of Ag and Ca was ECAP-deformed in an effort to enhance the mechanical strength by combining precipitation hardening with Hall-Petch strengthening. Several main findings are summarized in the following:

1. Ultrafine grain refinement was successfully achieved for the precipitation hardenable Mg-ZKQX6000 alloy, resulting in ultra-high strength levels (UTS ~400 MPa) for several orientations.
2. ECAP has a profound effect on precipitation for this alloy, both reorienting the initial precipitate stringers as well as dynamically precipitating an abundance of fine second phases along the DRX grain regions. Results indicate these particles detrimentally affect ductility levels via embrittlement along precipitate-grain interfaces.
3. Hybrid ECAP routes can develop a variety of unique textures for the Mg-ZKQX6000 alloy, which may be used to promote improved strength and ductility by favoring prismatic slip.

CHAPTER IV

CONCLUSIONS

In Chapter II of this work, Mg-AZ31 failure characteristics were categorized for differently favored deformation mechanisms (tension twinning, basal slip, and prismatic slip) at a low temperatures regime (25°C to 200°C). Here, effects of temperature on deformation mechanism activities was assessed in detail, and the role of DRX in relation to active deformation mechanisms was also investigated. It was found that optimal low temperature ductility and strength require ready activation of prismatic slip as the primary deformation mechanism. In contrast, tension twinning was strongly correlated with poor ductility, and basal slip was correlated with comparatively lower strength levels than prismatic slip.

In Chapter III of this work, a precipitation hardenable alloy, Mg-ZKQX6000, was processed via Equal Channel Angular Processing (ECAP) to test the upper limits of strength for magnesium alloys. Here, ultra-fine grain sizes with ultra-high strength levels approaching ~400 MPa were achieved along several orientations. However, it was shown that precipitates can detrimentally affect ductility due to embrittlement along the precipitate-grain interfaces. It is also worth mentioning that prismatic slip was correlated with optimal strength and ductility for the ZKQX6000 ECAP conditions, supporting the findings from Chapter II.

Given the findings from this thesis, several recommendations for future work in magnesium alloys can be made. First, novel wrought processing techniques should be

designed to produce crystallographic textures favorable for prismatic slip in the subsequent forming operations. Such techniques would allow for improved low temperature formability of wrought magnesium. Secondly, magnesium alloys utilized for structural applications should favor prismatic slip for enhanced strength levels. Thirdly, the effect of precipitates on mechanical properties can be detrimental to formability. Here, magnesium alloy design should consist of careful additions of secondary alloying elements, to allow for optimal strength enhancement via precipitation hardening while also preventing embrittlement due to excessive precipitation. Finally, the effect of wrought processing – in particular ECAP – on precipitation kinetics, morphology, and relation to failure in magnesium alloys requires further study.

REFERENCES

- [1] Y. Chang, D.M. Kochmann. A variational constitutive model for slip-twinning interactions in hcp metals: Application to single- and polycrystalline magnesium, *International Journal of Plasticity* 73 (2015) 39-61.
- [2] M.M. Myshlyaev, H.J. McQueen, A. Mwembela, E. Konopleva. Twinning, dynamic recovery and recrystallization in hot worked Mg–Al–Zn alloy, *Materials Science and Engineering: A* 337 (2002) 121-133.
- [3] J.C. Tan, M.J. Tan. Dynamic continuous recrystallization characteristics in two stage deformation of Mg–3Al–1Zn alloy sheet, *Materials Science and Engineering: A* 339 (2003) 124-132.
- [4] J.-F. Nie. Precipitation and Hardening in Magnesium Alloys, *Metall and Mat Trans A* 43 (2012) 3891-3939.
- [5] J.-M. Seitz, K. Collier, E. Wulf, D. Bormann, F.-W. Bach. Comparison of the Corrosion Behavior of Coated and Uncoated Magnesium Alloys in an In Vitro Corrosion Environment, *Advanced Engineering Materials* 13 (2011) B313-B323.
- [6] S.N. Mathaudhu, E.A. Nyberg. Magnesium Alloys in U.S. Military Applications: Past, Current and Future Solutions. in: Mathaudhu SN, Luo AA, Neelameggham NR, Nyberg EA, Sillekens WH, (Eds.). *Essential Readings in Magnesium Technology*. Springer International Publishing, Cham, 2016. pp. 71-76.

- [7] S.R. Agnew, M.H. Yoo, C.N. Tomé. Application of texture simulation to understanding mechanical behavior of Mg and solid solution alloys containing Li or Y, *Acta Materialia* 49 (2001) 4277-4289.
- [8] S.R. Agnew, Ö. Duygulu. Plastic anisotropy and the role of non-basal slip in magnesium alloy AZ31B, *International Journal of Plasticity* 21 (2005) 1161-1193.
- [9] R. Cottam, J. Robson, G. Lorimer, B. Davis. Dynamic recrystallization of Mg and Mg–Y alloys: Crystallographic texture development, *Materials Science and Engineering: A* 485 (2008) 375-382.
- [10] Y. Ding, C. Wen, P. Hodgson, Y. Li. Effects of alloying elements on the corrosion behavior and biocompatibility of biodegradable magnesium alloys: a review, *Journal of Materials Chemistry B* 2 (2014) 1912-1933.
- [11] S.B. Yi, S. Zaefferer, H.G. Brokmeier. Mechanical behaviour and microstructural evolution of magnesium alloy AZ31 in tension at different temperatures, *Materials Science and Engineering: A* 424 (2006) 275-281.
- [12] S.M. Razavi, D.C. Foley, I. Karaman, K.T. Hartwig, O. Duygulu, L.J. Kecskes, S.N. Mathaudhu, V.H. Hammond. Effect of grain size on prismatic slip in Mg–3Al–1Zn alloy, *Scripta Materialia* 67 (2012) 439-442.
- [13] D.J. Shaeffler. *Getting to Know More about the Metal You Are Forming, The Fabricator - A Publication of the Fabricators and Manufacturers Association, Intl.* (2016).

- [14] J. Koike, R. Ohyama. Geometrical criterion for the activation of prismatic slip in AZ61 Mg alloy sheets deformed at room temperature, *Acta Materialia* 53 (2005) 1963-1972.
- [15] S.M. Fatemi-Varzaneh, A. Zarei-Hanzaki, H. Beladi. Dynamic recrystallization in AZ31 magnesium alloy, *Materials Science and Engineering: A* 456 (2007) 52-57.
- [16] J. Koike, T. Kobayashi, T. Mukai, H. Watanabe, M. Suzuki, K. Maruyama, K. Higashi. The activity of non-basal slip systems and dynamic recovery at room temperature in fine-grained AZ31B magnesium alloys, *Acta Materialia* 51 (2003) 2055-2065.
- [17] X.Y. Lou, M. Li, R.K. Boger, S.R. Agnew, R.H. Wagoner. Hardening evolution of AZ31B Mg sheet, *International Journal of Plasticity* 23 (2007) 44-86.
- [18] M.R. Barnett, Z. Keshavarz, A.G. Beer, D. Atwell. Influence of grain size on the compressive deformation of wrought Mg–3Al–1Zn, *Acta Materialia* 52 (2004) 5093-5103.
- [19] E. Dogan, M.W. Vaughan, S.J. Wang, I. Karaman, G. Proust. Role of starting texture and deformation modes on low-temperature shear formability and shear localization of Mg–3Al–1Zn alloy, *Acta Materialia* 89 (2015) 408-422.
- [20] S. Sandlöbes, S. Zaeferrer, I. Schestakow, S. Yi, R. Gonzalez-Martinez. On the role of non-basal deformation mechanisms for the ductility of Mg and Mg–Y alloys, *Acta Materialia* 59 (2011) 429-439.

- [21] A.G. Beer, M.R. Barnett. Microstructural Development during Hot Working of Mg-3Al-1Zn, *Metall and Mat Trans A* 38 (2007) 1856-1867.
- [22] M.R. Barnett. Twinning and the ductility of magnesium alloys: Part I: “Tension” twins, *Materials Science and Engineering: A* 464 (2007) 1-7.
- [23] A.L. Oppedal, H. El Kadiri, C.N. Tomé, G.C. Kaschner, S.C. Vogel, J.C. Baird, M.F. Horstemeyer. Effect of dislocation transmutation on modeling hardening mechanisms by twinning in magnesium, *International Journal of Plasticity* 30–31 (2012) 41-61.
- [24] M.H. Yoo. Slip, twinning, and fracture in hexagonal close-packed metals, *Metallurgical Transactions A* 12 (1981) 409-418.
- [25] A. Jain, S.R. Agnew. Modeling the temperature dependent effect of twinning on the behavior of magnesium alloy AZ31B sheet, *Materials Science and Engineering: A* 462 (2007) 29-36.
- [26] A. Chapuis, J.H. Driver. Temperature dependency of slip and twinning in plane strain compressed magnesium single crystals, *Acta Materialia* 59 (2011) 1986-1994.
- [27] Z. Keshavarz, M.R. Barnett. EBSD analysis of deformation modes in Mg–3Al–1Zn, *Scripta Materialia* 55 (2006) 915-918.
- [28] J. Koike. Enhanced deformation mechanisms by anisotropic plasticity in polycrystalline Mg alloys at room temperature, *Metall and Mat Trans A* 36 (2005) 1689-1696.

- [29] R.E. Reed-Hill, W.D. Robertson. The crystallographic characteristics of fracture in magnesium single crystals, *Acta Metallurgica* 5 (1957) 728-737.
- [30] S. Choi, E. Shin, B. Seong. Simulation of deformation twins and deformation texture in an AZ31 Mg alloy under uniaxial compression, *Acta Materialia* 55 (2007) 4181-4192.
- [31] A.K. Rodriguez, G.A. Ayoub, B. Mansoor, A.A. Benzerga. Effect of strain rate and temperature on fracture of magnesium alloy AZ31B, *Acta Materialia* 112 (2016) 194-208.
- [32] G. Proust, C.N. Tomé, A. Jain, S.R. Agnew. Modeling the effect of twinning and detwinning during strain-path changes of magnesium alloy AZ31, *International Journal of Plasticity* 25 (2009) 861-880.
- [33] A.K. Rodriguez, G. Kridli, G. Ayoub, H. Zbib. Effects of the Strain Rate and Temperature on the Microstructural Evolution of Twin-Rolled Cast Wrought AZ31B Alloys Sheets, *Journal of Materials Engineering and Performance* 22 (2013) 3115-3125.
- [34] I. Ulacia, N.V. Dudamell, F. Gálvez, S. Yi, M.T. Pérez-Prado, I. Hurtado. Mechanical behavior and microstructural evolution of a Mg AZ31 sheet at dynamic strain rates, *Acta Materialia* 58 (2010) 2988-2998.
- [35] M.R. Barnett. Twinning and the ductility of magnesium alloys Part II. "Contraction" twins, *Mat Sci Eng a-Struct* 464 (2007) 8-16.

- [36] M. Lentz, A. Behringer, C. Fahrenson, I. Beyerlein, W. Reimers. Grain Size Effects on Primary, Secondary, and Tertiary Twin Development in Mg-4 wt pct Li (-1 wt pct Al) Alloys, *Metall and Mat Trans A* 45 (2014) 4737-4741.
- [37] L. Jiang, J.J. Jonas, R.K. Mishra, A.A. Luo, A.K. Sachdev, S. Godet. Twinning and texture development in two Mg alloys subjected to loading along three different strain paths, *Acta Materialia* 55 (2007) 3899-3910.
- [38] D. Ando, J. Koike, Y. Sutou. Relationship between deformation twinning and surface step formation in AZ31 magnesium alloys, *Acta Materialia* 58 (2010) 4316-4324.
- [39] T. Al-Samman, G. Gottstein. Dynamic recrystallization during high temperature deformation of magnesium, *Materials Science and Engineering: A* 490 (2008) 411-420.
- [40] Y. Chino, K. Kimura, M. Hakamada, M. Mabuchi. Mechanical anisotropy due to twinning in an extruded AZ31 Mg alloy, *Materials Science and Engineering: A* 485 (2008) 311-317.
- [41] S.E. Ion, F.J. Humphreys, S.H. White. Dynamic recrystallisation and the development of microstructure during the high temperature deformation of magnesium, *Acta Metallurgica* 30 (1982) 1909-1919.
- [42] A. Galiyev, R. Kaibyshev, G. Gottstein. Correlation of plastic deformation and dynamic recrystallization in magnesium alloy ZK60, *Acta Materialia* 49 (2001) 1199-1207.

- [43] R. Kaibyshev. 5 - Dynamic recrystallization in magnesium alloys. *Advances in Wrought Magnesium Alloys*. Woodhead Publishing, 2012. pp. 186-225.
- [44] T. Al-Samman, X. Li, S.G. Chowdhury. Orientation dependent slip and twinning during compression and tension of strongly textured magnesium AZ31 alloy, *Materials Science and Engineering: A* 527 (2010) 3450-3463.
- [45] A. Pineau, A.A. Benzerga, T. Pardoen. Failure of metals I: Brittle and ductile fracture, *Acta Materialia* 107 (2016) 424-483.
- [46] J. Deng, Y.C. Lin, S.-S. Li, J. Chen, Y. Ding. Hot tensile deformation and fracture behaviors of AZ31 magnesium alloy, *Materials & Design* 49 (2013) 209-219.
- [47] M. Marya, L.G. Hector, R. Verma, W. Tong. Microstructural effects of AZ31 magnesium alloy on its tensile deformation and failure behaviors, *Materials Science and Engineering: A* 418 (2006) 341-356.
- [48] A.K. Ray, D.S. Wilkinson. The effect of microstructure on damage and fracture in AZ31B and ZEK100 magnesium alloys, *Materials Science and Engineering: A* 658 (2016) 33-41.
- [49] M. Barnett, N. Stanford, P. Cizek, A. Beer, Z. Xuebin, Z. Keshavarz. Deformation mechanisms in Mg alloys and the challenge of extending room-temperature plasticity, *JOM Journal of the Minerals, Metals and Materials Society* 61 (2009) 19-24.

- [50] E. Dogan, I. Karaman, G. Ayoub, G. Kridli. Reduction in tension–compression asymmetry via grain refinement and texture design in Mg–3Al–1Zn sheets, *Materials Science and Engineering: A* 610 (2014) 220-227.
- [51] D.C. Foley, M. Al-Maharbi, K.T. Hartwig, I. Karaman, L.J. Kecskes, S.N. Mathaudhu. Grain refinement vs. crystallographic texture: Mechanical anisotropy in a magnesium alloy, *Scripta Materialia* 64 (2011) 193-196.
- [52] C.L. Mendis, K. Oh-ishi, Y. Kawamura, T. Honma, S. Kamado, K. Hono. Precipitation-hardenable Mg–2.4Zn–0.1Ag–0.1Ca–0.16Zr (at.%) wrought magnesium alloy, *Acta Materialia* 57 (2009) 749-760.
- [53] C.L. Mendis, K. Oh-ishi, K. Hono. Enhanced age hardening in a Mg–2.4at.% Zn alloy by trace additions of Ag and Ca, *Scripta Materialia* 57 (2007) 485-488.
- [54] C. Xu, M.Y. Zheng, S.W. Xu, K. Wu, E.D. Wang, S. Kamado, G.J. Wang, X.Y. Lv. Ultra high-strength Mg–Gd–Y–Zn–Zr alloy sheets processed by large-strain hot rolling and ageing, *Materials Science and Engineering: A* 547 (2012) 93-98.
- [55] J.D. Robson, C. Paa-Rai. The interaction of grain refinement and ageing in magnesium–zinc–zirconium (ZK) alloys, *Acta Materialia* 95 (2015) 10-19.
- [56] M.R. Barnett, N. Stanford, P. Cizek, A. Beer, Z. Xuebin, Z. Keshavarz. Deformation mechanisms in Mg alloys and the challenge of extending room-temperature plasticity, *JOM* 61 (2009) 19-24.
- [57] E.O. Hall. The Deformation and Ageing of Mild Steel: III Discussion of Results, *Proceedings of the Physical Society. Section B* 64 (1951) 747.

- [58] N.J. Petch. The cleavage strength of polycrystals, *J. Iron and Steel Inst.* 174 (1953) 25-28.
- [59] R.E. Barber, T. Dudo, P.B. Yasskin, K.T. Hartwig. Product yield for ECAE processing, *Scripta Materialia* 51 (2004) 373-377.
- [60] E. Dogan, S. Wang, M.W. Vaughan, I. Karaman. Dynamic precipitation in Mg-3Al-1Zn alloy during different plastic deformation modes, *Acta Materialia* 116 (2016) 1-13.
- [61] M. Al-Maharbi, I. Karaman, I.J. Beyerlein, D. Foley, K.T. Hartwig, L.J. Kecskes, S.N. Mathaudhu. Microstructure, crystallographic texture, and plastic anisotropy evolution in an Mg alloy during equal channel angular extrusion processing, *Materials Science and Engineering: A* 528 (2011) 7616-7627.
- [62] D. Sagapuram, M. Efe, K.P. Trumble, S. Chandrasekar. Flow transitions and flow localization in large-strain deformation of magnesium alloy, *Materials Science and Engineering: A* 659 (2016) 295-305.
- [63] G. Zhou, M.K. Jain, P. Wu, Y. Shao, D. Li, Y. Peng. Experiment and crystal plasticity analysis on plastic deformation of AZ31B Mg alloy sheet under intermediate temperatures: How deformation mechanisms evolve, *International Journal of Plasticity* 79 (2016) 19-47.
- [64] E. Schmid, W. Boas. ... *Kristallplastizität*, J. Springer, J. W. Edwards, Berlin, Ann Arbor, Mich., 1935.

- [65] A.S. Khan, A. Pandey, T. Gnäupel-Herold, R.K. Mishra. Mechanical response and texture evolution of AZ31 alloy at large strains for different strain rates and temperatures, *International Journal of Plasticity* 27 (2011) 688-706.
- [66] M. Knezevic, A. Levinson, R. Harris, R.K. Mishra, R.D. Doherty, S.R. Kalidindi. Deformation twinning in AZ31: Influence on strain hardening and texture evolution, *Acta Materialia* 58 (2010) 6230-6242.
- [67] T. Al-Samman, G. Gottstein. Room temperature formability of a magnesium AZ31 alloy: Examining the role of texture on the deformation mechanisms, *Materials Science and Engineering: A* 488 (2008) 406-414.
- [68] D. Ando, Y. Sutou, J. Koike. Internal microstructure observation of enhanced grain-boundary sliding at room temperature in AZ31 magnesium alloy, *Materials Science and Engineering: A* 666 (2016) 94-99.
- [69] A. Khosravani, J. Scott, M.P. Miles, D. Fullwood, B.L. Adams, R.K. Mishra. Twinning in magnesium alloy AZ31B under different strain paths at moderately elevated temperatures, *International Journal of Plasticity* 45 (2013) 160-173.
- [70] J. Su, M. Sanjari, A.S.H. Kabir, I.-H. Jung, S. Yue. Dynamic recrystallization mechanisms during high speed rolling of Mg–3Al–1Zn alloy sheets, *Scripta Materialia* 113 (2016) 198-201.
- [71] E. Dogan, M.W. Vaughan, S.J. Wang, I. Karaman, G. Proust. Role of starting texture and deformation modes on low-temperature shear formability and shear localization of Mg-3Al-1Zn alloy, *Acta Materialia* 89 (2015) 408-422.

- [72] E. Mostaed, M. Hashempour, A. Fabrizi, D. Dellasega, M. Bestetti, F. Bonollo, M. Vedani. Microstructure, texture evolution, mechanical properties and corrosion behavior of ECAP processed ZK60 magnesium alloy for biodegradable applications, *Journal of the Mechanical Behavior of Biomedical Materials* 37 (2014) 307-322.